FACULTY OF TECHNOLOGY

DESIGN AND IMPLEMENTATION OF A SENSOR TESTING SYSTEM WITH USE OF A CABLE DRONE

Oskari Virtanen

MECHANICAL ENGINEERING

Master's thesis

January 2022

ABSTRACT

Design and implementation of a sensor testing system with use of a cable drone

Oskari Virtanen

University of Oulu, Degree Programme of Mechanical Engineering

Master's thesis 2022, 100 pp.

Supervisors at the university: M.Sc. (Tech.) Antti Tikanmäki and University lecturer, D.Sc. (Tech.) Toni Liedes

This thesis aims to develop a testing method for various sensors by modifying a commercial cable cam system to drive with an automated process at constant speed. The goal is to find a way to lift the cables in the air securely without a need for humans to climb on ladders and place them afterwards. This is achieved with a hinged truss tower structure that keeps the cables stabile while the tower is lifted. Another goal was to achieve automated movement of the cable drone. This is done by connecting a tracking camera to a computer that is used to control the cable drone's motor controller. This will have the drone behave in a certain way depending on the tracking camera's position data. Third goal is to build a portable sensor system which collects and saves the data from the tested sensors. This goal is achieved with an aluminium profile frame which is equipped with all the necessary equipment, such as a powerful computer.

Research included studying different sensors' performance evaluation criteria and effect of the wind on magnitude of the force in this application. Research was done by studying written sources and consulting a cable camera company called Motion Compound GbR. Results of this master's thesis are used to evaluate if the idea of using a cable cam is applicable for this kind of sensor testing system. As the conclusion the cable drone with automated driving is evaluated to be a practical method which can still be further developed to meet the requirements even better.

Keywords: sensors, test equipment, unmanned aerial vehicles

TIIVISTELMÄ

Antureiden testausjärjestelmän suunnittelu ja toteuttaminen käyttäen vaijeridronea

Oskari Virtanen

Oulun yliopisto, Konetekniikan tutkinto-ohjelma

Diplomityö 2022, 100 s.

Työn ohjaaja(t) yliopistolla: DI Antti Tikanmäki ja yliopistonlehtori, TkT Toni Liedes

Tämän diplomityön tavoitteena on muokata kaupallisesta vaijerikamerajärjestelmästä vakionopeudella liikkuva testausmenetelmä eri antureille. Yhtenä työn tavoitteena on löytää tapa nostaa käytettävät vaijerit ylös turvallisesti siten, ettei niitä tarvitse asentaa jälkikäteen korkealla. Tämä toteutetaan saranoidulla, trusseista rakennetulla tornilla. Tornin huipulle asennetaan laakeroidut akselit sekä suoja, jotka yhdessä pitävät vaijerit paikoillaan myös tornin noston ajan. Toinen tavoite on saavuttaa vaijerilennokin automatisoitu liike. Tämä tapahtuu kytkemällä seurantakamera tietokoneeseen, jota käytetään ohjaamaan myös vaijeridronen moottoriohjainta. Näin vaijeridrone saadaan käyttäytymään halutulla tavalla riippuen seurantakameran sijaintitiedoista. Kolmas tavoite on rakentaa kannettava anturijärjestelmä, jolla kerätään ja tallennetaan testatuilla antureilla kerätty data. Tämä tavoite saavutetaan alumiiniprofiilirungolla, joka varustetaan tarvittavilla laitteilla, kuten esimerkiksi tehokkaalla tietokoneella. Tutkimukseen kuului myös antureiden suorituskyvyn arviointikriteereihin tutustuminen sekä työssä käytettävästä järjestelmästä koituvan voiman suuruuden laskeminen. Tutkimus tehtiin perehtymällä kirjallisuuteen ja konsultoimalla vaijerikamera-alalla toimivaa Motion Compound GbR -yritystä. Tämän diplomityön tuloksia voidaan hyödyntää arvioitaessa, onko vaijerikamerajärjestelmä sovellettavissa mainitun anturien testausjärjestelmän rakentamisessa. Lopputuloksena automatisoidulla ajolla varustetun vaijeridronen arvioidaan olevan tähän tarkoitukseen toimiva menetelmä, jota voidaan edelleen kehittää vastaamaan vaatimuksia vielä paremmin.

Asiasanat: anturit, miehittämättömät ilma-alukset, testauslaitteet

FOREWORD

This master's thesis was ordered by the University of Oulu Biomimetics and Intelligent Systems Group (BISG). The purpose was to design a system which moves at constant speed. The system could then be used to test and evaluate moving sensors and other devices. This thesis is part of the 5G!Drones-project.

First, I want to thank Professor Juha Röning for offering me a job as a research assistant and my supervisors, Toni Liedes and Antti Tikanmäki, for the ideas and knowledge they shared with me during the work. I would also like to thank my co-workers for the help I received from them, especially when the schedule was tight.

Finally, I wish to give my warmest thanks to my family and friends for the support I have received during my studies.

Oulu, 18.12.2021

Oskari Virtanen

TABLE OF CONTENTS

LIST OF ABBREVIATIONS

A_{ref}	reference area of the structure or structural element [m^2]
A_{x}	horizontal component of reaction force A [N]
A_{y}	vertical component of reaction force A [N]
a	a parameter used to calculate the catenary equation
b	diameter of the cable [m]
$c_{\mathrm{e}}(z)$	exposure factor
c_{f}	force coefficient for the structure or structural element
$c_{\mathrm{f,0}}$	force coefficient of structural elements without free-end flow
$c_{\mathrm{s}}c_{\mathrm{d}}$	structural factor
D	sag of the cables [m]
F_{b}	tensile force acting on a bolt [N]
F_{bg}	projected tension force of the guy-wire in the back [N]
F_C	force the cable cam system exerts to the anchoring point [N]
F_{fg}	tension force of the guy-wire in the front [N]
F_{m}	force caused by mass of the structure [N]
F_{tot}	resultant force due to forces acting on the cable [N]
F_{w}	wind force [N]
G	resultant force due to cable's weight and the payload's weight [N]
g	gravitational acceleration [m/s^2]
h	height of the cable cam system in the direction of wind [m]
h_{g}	height of the guy-wires anchoring point [m]
h_{sag}	sag of the cable [m]
h_{t}	height of the truss tower [m]
L	distance between poles where the cable is hung [m]
l_{c}	length of the cable [m]
M_{A}	bending moment about the point A [Nm]
m_{p}	mass of the system [kg]
m_{sp}	mass of the steel plate [kg]
q	distributed weight of the cable [kg/m]
q_{c}	distributed weight of the cable [kg/m]

$q_{\mathrm{p}}(z_{\mathrm{e}})$	peak velocity pressure at reference height z_e [Pa]
R_{B}	breaking load of the main cable [N]
R_{P}	maximum permissible rated load of the main cable [N]
T	tension force [N]
T_0	vertical tension force [N]
v_{b}	basic wind velocity [m/s]
w	width of the cable cam system in the direction of wind [m]
x	distance between anchoring points [m]
y_1	distance to between bolts [m]
y_2	distance between bolts in the middle and the hinge axle [m]
y_{b}	distance between the bolt and the hinge axle [m]
y_{cable}	plotted cable in correct height

a	angle [°]
β	angle [°]
γ	safety factor
γ_{G}	partial safety factor for permanent actions in amusement devices
θ	angle [°]
ρ	air density [kg/m^3]
φ	coefficient due to dynamic factors
ψ_λ	end-effect factor

1 INTRODUCTION

Robots and drones are used in a wide range of circumstances in different environment. Therefore, it is essential to find out more about how well the sensors operate in practice. Even though for example LiDAR sensor manufacturers often list their products' range, range accuracy, field of view and other important specifications, the testing methods can vary between the manufacturers, or the testing method may not be directly specified. This thesis introduces a testing system that can be utilized for testing of various sensors simultaneously. It is done by modifying a commercial cable cam system. Modifications include inter alia devices which the automated driving sequence requires to work.

The designed testing system aims to provide a way to acquire information of how the sensors' performance is affected by their movement. This information would improve both usability and reliability of the sensors when they are used in other applications. However, this information is not accessible without a valid and a consistent way to gather the data. This thesis aims to develop a technical solution to test sensors which move at constant speed. The data needs to include a timestamp and the speed which the sensor is moving so they can be analyzed later. Sensors are attached to the frame, which is easily attached to the device by which the movement is carried out.

Autonomous robots need to work reliably in various circumstances. Thus, the testing of sensors should be done in a changing environment and at different locations. Gathering sufficient data to draw conclusions requires the measurements to be repeated in the same way throughout the testing period. This sets a few requirements for the testing equipment, which must be considered. Testing equipment will have to be steady enough to work properly without surveillance for a relatively long period. It also needs to be light and adaptable enough to be used in an urban environment. The lightness of the equipment improves portability and eases the installation on field, making the tests more efficient. In this master's thesis a hinged truss tower structure will be developed. This will offer more testing site opportunities.

The system needs to carry different kinds of measuring devices such as sensors and cameras simultaneously. The system must operate with payloads varying anywhere from a few grams to a couple of kilograms, depending on what kind of equipment is tested at given time. This kind of system could be developed in different ways. A testing

system could be built using for example a sledge moving on a rigid railway track or a UAV (Unmanned Aerial Vehicle) such as a drone. However, to make sure that the tests and measurements meet the requirements placed on repeatability and adaptability, a cable cam system is used to carry the measuring instruments. A cable system is more adaptable and easier to move to different locations than a rigid track and more stable than a normal drone.

This master's thesis covers some of the known phenomena that appear in pictures taken in motion and proceeds then to the topic about commonly used positioning methods, which will be used later in the tests. Some sensors designed for positioning and mapping are presented as they are needed in this project. Then a system for classifying drones as well as the general use of cable camera systems are presented. Next topic approaches the designing of the testing system in a more mathematical aspect. It covers the catenary curve and the forces acting on the cables. At the end of this section, some of the features used in assessing sensor performance are listed as an example of what kind of information the finalized testing system should provide.

After that the main focus will move on to the solution which the thesis will suggest. This starts by presenting the cable drone. The solution includes the design of anchorage as well as the portable sensor system. Modifications made to the original cable cam system are shown and a method for automating the cable drone's movement is presented. A solution for lifting and anchoring the cables of the cable drone system are then thoroughly presented with relevant static calculations. The portable sensor system chapter covers the designing of the portable sensor system's frame and presentation of the used sensors. Finally, this master's thesis goes through the tests, and the results, which are done to the system while it's being developed and evaluated.

2 SENSORS IN MOTION

This chapter will consider phenomena and factors which are known to have effect on the outcome when image sensors are used while in motion. The problem of tracking a moving vehicle has been addressed and some commonly used sensors are given as an example on how this problem can be solved. The topic “drones as a method of movement” offers basic knowledge about drones’ classification and use of cable cam systems. Essential equations used in the applications of cable cam systems are derived. Equations included in this chapter are for the catenary and the forces acting on the cables. Key factors used in sensors’ usability and performance validation are briefly described. This is to provide enough information on the subject so that the importance of valid and consistent sensor evaluation is clear.

2.1 Phenomena and related research in aspects of image sensors in motion

Digitally converting and transmitting signals derived from sensors will always cause some errors to the signals. The image data may show different kinds of errors such as motion blur, defocus and deterioration or loss of either bit, pixel or frame while copying or reading the image. Noise may occur when capturing or transmitting the image. These kinds of errors can be corrected with image restoration. The quality of the resulting image is dependent on the amount and speed of relative movement between camera and object as well as on characteristics of the camera. (Bovik, 2005, McHugh 2019)

The noise effect can be seen as grain-like random spots and uneven disturbance everywhere on the background of the image. Image noise on digital images can be described as the digital equivalent of film grain on analog cameras. Image noise occurs on digital images for various reasons and can be hard to remove without degrading the image. Noise can appear on images as random, fixed-pattern or banding type of disturbance. Unavoidable nonperiodic high-frequency random noise mostly results from thermal noise as well as from the amount and arriving position of incoming photons. Fixed-pattern noise (FPN) shows in the image as errors in pixels. The pixel causing the error can be either stuck, dim or hot, so FPN is due to characterize every individual sensor. FPN stays the same between the photos which are taken with the same settings on camera and at the same temperature. Banding noise occurs as data is read from the

image sensor and therefore it is rather more dependent on the camera itself than any external factors. Banding noise is most visible in dark areas of an image. (Mansurov 2020, McHugh 2019)

Image noise occurs on digital images for various reasons and can be hard to remove without degrading the image. Noise's appearance is often described in electronic systems with signal-to-noise ratio (SNR) which compares relative amounts of signal with noise captured. High SNR means that noise is relatively small compared to the rest of the received signal. If the SNR is sufficiently high, the noise effect is reduced to almost non-existent. One way to reduce noise is to learn the pattern which FPN makes on a certain environment and then filter it out of the final image. Image restoration methods using stochastic relaxation, Gibbs distributions and the Bayesian restoration, have been found functional also when reducing noise. Noise can be reduced from data measured with a time-of-flight device with suitable customized filters. (McHugh 2019, Georgiev et al. 2015, Geman & Geman 1984)

Imperfect image formation process causes an effect called blurring. According to Lagendijk and Biemond (2009), blurring happens when the bandwidth of an ideal image is reduced. Imperfections appearing during the formation of the image can be caused by relative motion between camera and photographed object while the camera's shutter is open, or the rotating sensor is moving while turning. Illustration of a scene where motion blurring will occur is presented in Figure 1. The quadrangle in Figure 1 depicts a camera, and the triangle shape depicts the field of view which camera sees. The image is being formed while the camera moves from position A to position B. Optical system itself can also cause blurring in images if it is out of focus. (Lagendijk, Biemond, 2009)

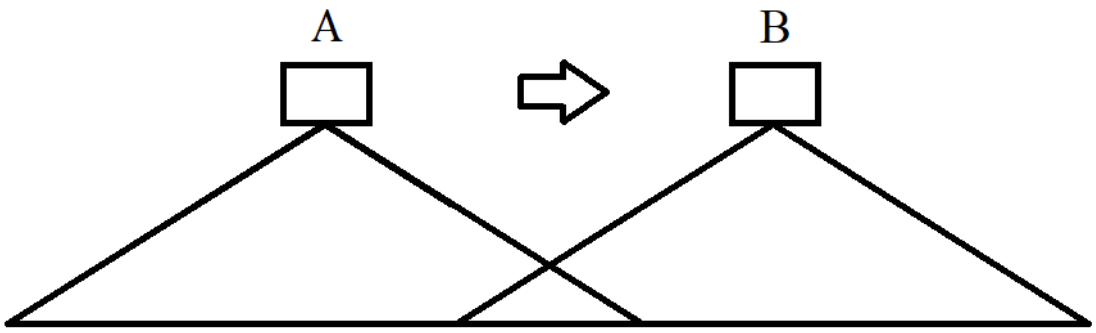

Figure 1. Illustration of a scene where motion blur will occur.

Rotational and translational movement will also cause the same kind of blurring effect. Red areas in Figure 2 visualizes for example a field of view of a rotating sensor or camera. Figure 2 is created in MATLAB. Figure 2 shows a possible outcome of scenarios where a camera is on translational motion. The camera rotates 360° counterclockwise while it moves from point A to point B. The path is illustrated with a thin black line. Distance between points A and B increases to show how the area changes. Any kind of movement while the camera's shutter is open will cause blurring and distortion on image if the effect is not otherwise prevented or corrected afterwards.

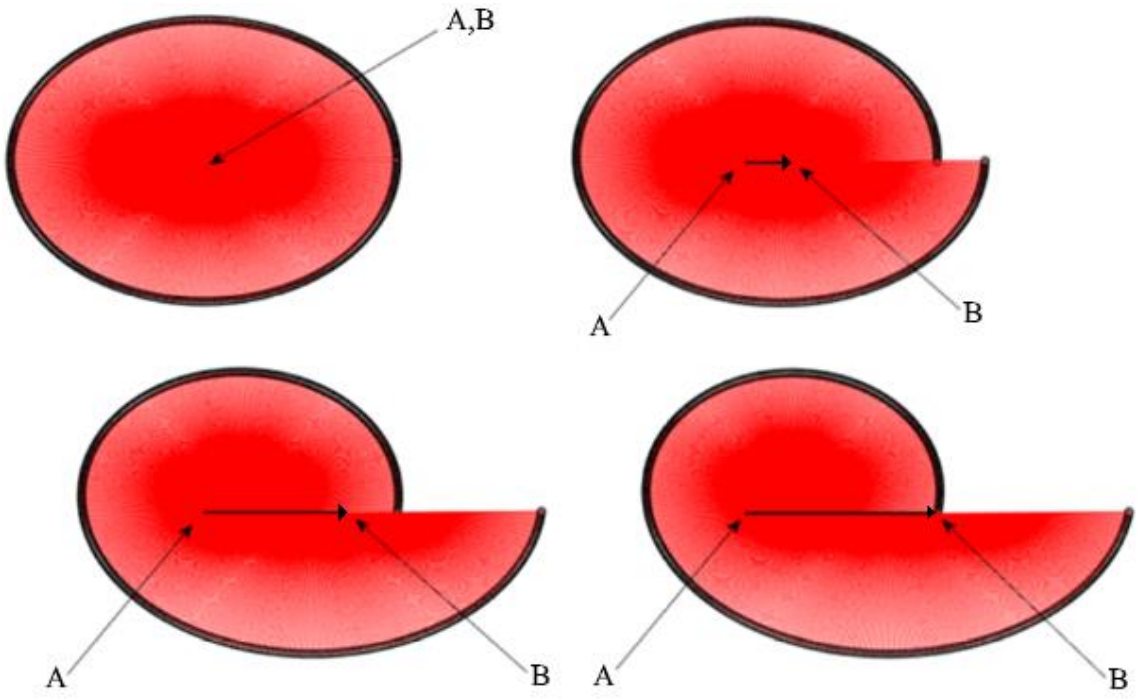

Figure 2. A camera's field of view on rotational and translational motion.

Blur can also be caused from other factors than motion e.g., defocus, diffraction, optical aberrations, and detector crosstalk. On occasions where there are large variations in scene radiance, one or more contrast enhancements may be required to improve images. Applying methods like edge enhancement, histogram equalization or filters such as a sharp filter on the image change the appearance of the scene compared to the original image. (Rastogi 2015)

In their article called Motion-Based Motion Deblurring (published in 2004), Ben-Ezra and Nayar presented a differing solution to previous methods for deblurring the motion blurring effect from images. While the previous methods for dealing with motion blurring had used blind restoration, optical correction with stabilized lenses and CMOS

sensors which shorten the exposure time, Ben-Ezra's and Nayar's method was to construct a camera which can measure its motion while integrating an image. To use this information to deblur the image, it is first computed to a point spread function which corresponds to the camera's path while taking the picture.

In their book Chellappa and Rajagopalan (2014) list methods for dealing with blurring. First blurring was reduced in a non-blind way by designing a stable estimate for the original image. This works for images which can be assumed to have a simple form motion blur kernel. This kind of point spread functions (PSF) come from uniform motion of the camera. Methods have developed greatly, and nowadays shaking and nonuniform motion can be estimated. Traditional solutions post-process the image into the deblurred version with information gathered by comparing the data from the stationary sensor with the blurred image taken with a moving camera. More developed ways combine constantly evolving aspects of motion deblurring and sensor design, which leads into completely new solutions. Solutions which Chellappa and Rajagopalan (2014) presented in their book include for example multi-sensor fusion which is an extension to the already mentioned hybrid-imaging system by Ben-Ezra and Nayar, a fluttering camera shutter and hybrid-imaging implemented with multiple cameras.

More recent way to deblur image and estimate depth in image was introduced by Anwar et al. (2021). Their method utilizes fully connected cascaded convolutional neural networks on a patch-pooled set of feature maps to depth estimation. Depth information is then used to deblur and re-focus the image. This method can reconstruct the image from a single image without any additional information which is a great advancement if compared to earlier methods. This method also increases depth accuracy and efficiency of deblurring. Image restoration methods are showing promising results and constantly evolving.

2.2 Tracking the movement

Remote tracking of the location and movement of a robot or vehicle is one of the basic problems with remotely controlled and automated vehicles. Some options are suitable for one purpose and one for the other. When making a choice, it is necessary to decide what features are required for the system and how it fits in the budget. Prices of options can vary widely, depending on for example the accuracy of the system and the principle

of operation. It is common to use multiple methods at the same time to support each other.

Wheel odometry

One commonly used technique to estimate the location of a moving system is wheel odometry. This method can be basically implemented in any system which moves on wheels, for example in robots and cars. Wheel odometry is based on collecting information from a rotating wheel. Revolutions of the wheel can be measured for example with an encoder. This information is then translated into linear displacement in relation to the ground.

Wheel odometry is a popular solution for localization because it is an inexpensive method which allows high sampling rates. Wheel odometry is a relative positioning method. It does not consider if the wheel spins without moving the object linearly as intended. This will cause inaccuracy and drifting on the estimated position. Wheel odometry works best on short distances because the errors accumulate relative to the increase in travelled distance. (Aqel et al. 2016)

Errors that occur can be treated as systematic and non-systematic depending on the cause. Systematic errors can be due to geometric differences between the actual and the used nominal values of tire or wheelbase. Misalignment of the wheels will also lead to systematic error in measurements. Encoder sets restrictions on accuracy due to the available resolution and sampling rate. Non-systematic errors can be the result of for example uneven or rough terrain, slipping wheels or unnoticed obstacles. If a drive wheel loses contact with the surface, it can lead to excessive rotation of the wheel compared to the linear movement. Both internal and external forces restricting free turning of the wheel can cause non-systematic error. (Gaudiot et al. 2020 p.39)

Global Navigation Satellite System based positioning

Another way to track location is to use GNSS (Global Navigation Satellite System) receivers. GNSS includes all operating and planned satellite positioning systems which are GPS (Global Positioning System) from United States, Russian GLONASS, (Globalnaya Navigazionnaya Sputnikovaya Sistema), Galileo from European Union,

Chinese BeiDou, Indian IRNSS (Indian Regional Navigation Satellite System) and Japanese QZSS (Quasi-Zenith Satellite System).

GNSS radio frequency signals operate at around 1,5 GHz. The GNSS receivers get the signal from the satellites via antennas. Antennas need to be able to connect with at least four satellites to get the position and time. This means that the satellites must be clearly in sight so there may be no buildings or other obstructions between them. There are many different antennas for different applications, differing, for example in size, shape, and performance. The receiver calculates propagation time by comparing the received PRN (pseudorandom noise code) signal's phase to the known PRN which was transmitted. Positions of satellites are known so the receiver can use the propagation time to calculate its position and time. With standalone GNSS the accuracy of position calculations is in few meters. (Georgy 2013 p.66, Cook 2011, NovAtel 2015)

One way to improve the accuracy is to use is Real-time kinematic (RTK) GNSS, which is a high precision positioning method. It makes it possible to improve the position estimation's accuracy significantly from a standalone system's few metres and reach an accuracy of 2 cm. This is achieved by using a carrier-based technique instead of a code-based one. Carrier-based ranging uses magnitudes instead of PRN phase which makes it much more precise. RTK has two types of techniques called float and fix. Float is easier to achieve as it needs 4 reachable satellites where fix needs 5. The float technique can offer accuracy from 1 meter to 20 cm. The fix technique can manage to reach the mentioned 2 cm accuracy. (Cook 2011, Georgy 2013 p.67, Morales 2007, NovAtel 2015)

RTK GNSS uses one GNSS receiver as a stationary base station and another as a rover station, which is attached to the moving object like a drone or robot. Rover must be within 10 km to the base station. Rover's position is estimated by using information which it receives from the satellites' transmitted signal and then to achieve the high accuracy the errors are corrected with base stations measurements. Most of the errors are caused by delay due to ionosphere and troposphere but also from errors in satellite clock and ephemerides. Position is calculated by using ambiguity resolution and differential correction algorithms. Resolving the phase ambiguities is essential part of the RTK GNSS' accurate position estimation. (Georgy 2013, Morales 2007, NovAtel 2015)

Correction data transmitted to the rover can be used in real-time or it may be post processed later. Corrections' accuracy depends on how accurate the base station's location is to satellite observation and connection quality. RTK suffers from the same problems as typical GNSS in the sense that signal can easily be interfered with by the environment and cause multipath issues where the signal ricochets from somewhere and does not move on a straight path. (Cook 2011, Georgy 2013 p.75–76, NovAtel 2015)

Simultaneous localization and mapping

Robots and drones can use SLAM (Simultaneous localization and mapping) to learn about their surroundings and pose in real-time. SLAM is a technique which estimates the state of a robot while simultaneously constructing a model of its surroundings and environment. This is done with robot attached sensors. Robot's state describes its position and orientation, but it can also include velocity, sensor biases and calibration parameters if required. (Cadena et al. 2016 p.1309) The constructed model of its surroundings and environment including aspects of interests for example obstacles or landmarks is called the map.

Other applications can use the map as aid to perform better in their task. The map offers valuable visualization of surroundings if the robot is controlled by humans. Path planning can use the map's information to optimize the calculated path. Errors in state estimation can also be limited with the map, because when drifting is detected on the map it can be corrected in calculations. Localization error of the robot can be corrected by going to the already constructed place on the map with recognizable objects or landmarks. This is called a loop-closure. (Cadena et al. 2016 p.1309)

Noisy data from the sensors cause the mapping process to include errors to the constructed map. Landmarks may not be located precisely where they are calculated to be according to the sensor's data. Uncertainty of the sensors is therefore important to know so it needs to be evaluated. When the uncertainty is sufficiently well evaluated, the landmarks' real locations can also be estimated for example with Gaussian estimation. (Haataja et al. 2018 p.2)

SLAM is a part of several different fields of research which are divided to a higher and a lower level. The higher level can be called the back end and lower level as the front end. On the back end SLAM involves geometry, probabilistic estimation, optimization,

and graph theory. On the front end SLAM is part of computer vision and signal processing. The front end can be described to consist of feature extraction and data association. The front end's data association has also two subcategories: short-term which handles feature tracking and long-term which works on loop-closure. Sensor's data is processed in the front end and that information is passed to the back end. The back end handles the map estimation. The front end uses feedback information received from the back end to properly detect loop closures and to verify features. (Cadena et al. 2016 pp.1310–1311)

In vision-based SLAM, or VSLAM, the estimation of movement is based on visual inertial odometry (VIO). This is an iterative task which begins with taking a picture of surroundings. A feature detection algorithm is then applied to the picture, which diminishes the number of white pixels on the picture by first replacing it with black picture and adding only detected features. What features are detected depends on what algorithms were used. The features are named by another algorithm so they can be treated as individual feature vectors. Because this is done to every picture or frame, a feature tracking algorithm can be used to compare the consecutive frames to estimate the movement of the sensor. (Brook et al. 2020)

Besides the already mentioned cameras, SLAM can be implemented with different kinds of sensor combinations including for instance LiDAR, inertial sensors or GNSS. VSLAM also needs other sensors or multiple cameras to work properly, as a single camera cannot by itself recognize how much the sensor has moved. (Brook et al. 2020). The basic principle of operation, recognizing features and tracking them, stays the same whether the sensor is based on vision or laser scanning. With LiDAR the depth estimation and loop-closure are easier to achieve but it can fail in challenging weather conditions. (Basri et al. 2017 p. 338)

Haataja et al. (2018) present in their paper three principal paradigms of SLAM problem solving. The paradigms are extended Kalman filter (EKF), particle filter and graph-based SLAM. They are probabilistic techniques which are used to evaluate the uncertainty caused by observation noise and poor data association in different situations. EKF is a solution when the problem is about Gaussian distribution, and the particle filter is used when the problem is involved with multimodal random distribution. Graph-based SLAM minimizes the sensor's raw measurements and generates a

simplified graph of the system and uses it to find out the configuration of the robot's pose at a certain time.

Light detection and ranging

A common abbreviation for light detection and ranging sensors is LiDAR. LiDAR sensors an amplitude modulated laser diode. In one scanning period, the laser scans a specific area once. This area is called a field of view or FOV. In some LiDARs the FOV can be 360° so one or more directed laser rays rotates a full circle. This can be done with a rotating mirror which deflects the ray. A noticeable amount of energy is reflected back to the sensor as a ray interferes with sensor's surroundings for instance a wall or another obstacle. The distance between the sensor and the object is calculated from the transmitted and received pulses. These pulses move at the speed of light and some LiDARs transmit 150 000 pulses per second. The LiDAR generates a point cloud of the scanned area. Points include the distance information and the intensity based on the reflected ray's energy. Signal processing handles the difference in variations of reflected energy. (Gröll and Kapp 2007 p. 2945, Gaudiot p. 23, Ibanez-Guzman and Li 2020 pp. 51-52)

Ibanez-Guzman and Li (2020) explain in their article working principles of LiDAR by dividing it into subsystems. A LiDAR sensor is a combination of the laser rangefinder system and the scanning system. The laser rangefinder system includes the laser transmitter, the photodetector, optics and the signal processing electronics. There are direct or coherent detection rangefinders. The direct detection laser rangefinders use pulsed laser's time-of-flight to calculate the distance. Coherent detection laser rangefinders are used with frequency-modulated continuous wave signal lasers. Coherent detection laser rangefinders calculate distance and velocity indirectly from Doppler effect. The scanning system directs the laser beam to a wide area of the sensor environment in different angles by either mechanically with for instance a rotating mirror or without moving parts by solid state scanning.

LiDARs are widely used in the robotics and automotive industry. Applications include for example UAV drones, autonomous vehicles, geographical mapping, traffic speed measurement and safety systems to name but a few. Typically, LiDARs are used to detect obstacles and to map the surroundings. LiDARs are not capable of recognizing objects as well as cameras do but they are superior in depth estimation and therefore

they are often used together. Working with LiDARs in real-time applications does have some downsides. The gathered data is computationally expensive which sets requirements for the computer. The received power, which means the amount of power the photodetector receives from backscattered photons, diminishes when LiDAR is used in challenging weather conditions, for instance fog, rain, dust or snow. The number of particles in the air which scatter and absorb the photons increases in this kind of weather. There are other factors too which affect the received power, for example distance to the object and objects' reflectivity. To keep LiDAR safe to use, the ray leaving the sensor must not contain too much energy, so the problem caused by a decrease in energy must be solved by other means. (Cherian and Motaz 2020, Georgy 2013 p. 13, Ibanez-Guzman and Li 2020 p.51)

Inertial sensors

An IMU (inertial measurement unit) can be used to measure device's orientation, forces acting on it, as well as angular and linear velocities. For example, in drone applications IMUs are used in the flight stabilization, as they can provide crucial information of the attitude and heading of the drone. Inertial sensors can keep the drone straight and prevent it from drifting as they can detect changes in attitude and movement on the horizon. The IMU should be placed near the drone's center of mass. Vibrations should be dampened to improve IMU's data quality and reduce unwanted noise on the data. (Cultofdrone 2021)

IMUs consist typically of gyroscopes and accelerometers. It is also common to have an IMU equipped with a magnetometer to enhance reading of the gyroscope, but it does not fuse data to make estimates of orientation. Sensor which provides orientation estimates is called an AHRS (attitude and heading reference system) or a VRU (vertical reference unit). Difference between AHRS and VRU is that AHRS has a true magnetic north referenced yaw. Gyroscopes are used to measure angular rate with respect to an inertial reference frame and accelerometers to measure specific force. Magnetometers provide information of the magnetic field around the system. (Vectornav 2021b, Xsens 2021a)

Gyroscopes have different performances depending on their type. One of the parameters by which gyroscopes are evaluated is the minimum bias that cannot be estimated. It is called in-run bias stability. The higher the stability, the smaller the bias is which can be

estimated. Mechanical gyroscopes have the highest in-run bias stability which can be less than 0,0001 °/hour. Other types are FOG (fiber-optic gyroscope), RLG (ring laser gyroscope) and quartz/MEMS gyroscope. MEMS is an acronym for Micro-electro-mechanical System. (Vectornav 2021b, Xsens 2021c)

There are also different types of accelerometers differing in how they work. The types are mechanical, quartz and MEMS. An accelerometer measures inertial acceleration or change in velocity over time. Three inertial sensors are needed to get three-dimensional measurements because an individual inertial sensor is measuring changes along or about a single axis. Three orthogonally placed individual sensors form a triad, which can measure 3-axis at the same time. Hence this type of sensor is called 3-axis inertial sensor. 6-axis inertial sensors, which provide information on the three axes with two different measurements, are a combination of three accelerometers and three gyroscopes. Similarly, adding 3 magnetometers to the 6-axis inertial sensor system makes it a 9-axis system. A 10-axis system has an additional barometer included. (Vectornav 2021a, Vectornav 2021b)

IMUs can be used as retrofitted external measurement units, but there are many applications which have integrated IMUs already included as part of the product. Cars, drones, robots, navigation and tracking systems or even other sensors like LiDARs and cameras are typical applications which benefit either directly or indirectly from the information IMUs are providing. One example of sensor systems which combines the data from an IMU, a VRU and an AHRS with external positioning data is GNSS/INS (Global Navigation Satellite/Inertial Navigation System). (Xsens 2021b)

2.3 Drones as methods of movement

Sophisticated devices are designed to make it easier to take pictures in movement and to minimize imperfections of images resulting from the user. Stabilized mounts and gimbals can prevent cameras and sensors from shaking. A gimbal reduces rotation of a device about a single axis. Using multiple gimbals mounted at 90° to each other makes it possible to create a 2- or 3-axis gimbal. A 2-axis gimbal rotates freely on one axis whereas a 3-axis gimbal allows the mounted device to be fixed on any direction. (Unmanned Systems Technology 2021, Artlist 2020)

Figure 3 shows a cube which now represents an object mounted on a gimbal. If the cube is mounted to a 2-axis gimbal, then undesired rotation of two axes can be corrected. In the 2-axis gimbal, it is rolling and pitching which are corrected and yaw is left uncontrolled. Roll, pitch, and yaw can also be called tilt, roll and pan. (Artlist 2020) The cube in Figure 3 has an X, a square and a circle marked on its sides. The side with an X is the front and the side with a circle is the top. If the cube were to represent a camera the X-side would have a lens, the pitch would tilt the lens up and down and yaw would pan the lens to left and right.

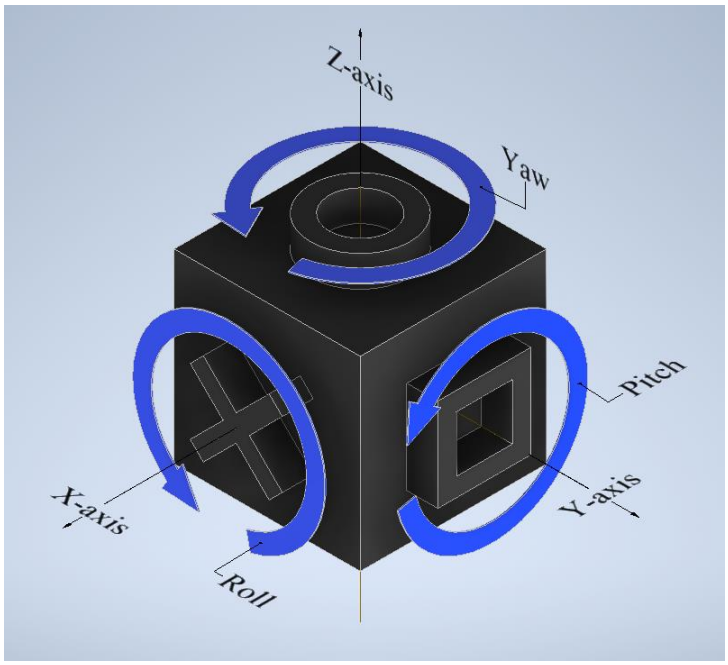

Figure 3. Roll, pitch, and yawn represented with a cube.

A gimbal balances the mounted device with separate motors which are activated with data collected from movement with integrated Inertial Measurement Unit (IMU). The data is used as an input to a controller which then activates motors needed to cancel the movement. A 3-axis gimbal has one motor more than a 2-axis gimbal which makes it more expensive and heavier, but it outperforms a 2-axis version in image quality. (Unmanned Systems Technology 2021)

The first one to revolutionize the film industry with a handheld stabilizing mount was cinematographer Garret Brown who invented the Steadicam in early 1970s. He got a patent for the Steadicam in 1977 and a year later he was awarded with an Academy Award for Technical Achievement. In 1979 Brown invented the SkyCam which is also a stabilized camera system, but it is operated on suspended cables for airborne filming

and imaging. In addition to the Tiffen company that owns Steadicam, other manufacturers such as for example DJI, Freefly Systems and ZHIYUN-TECH offer suitable gear for consumers and professionals. Manufacturers offer a comprehensive range of gimbal cameras, camera stabilizers, integrated systems, accessories, and maintenance services. (DJI 2021, Freefly Systems 2021, The Tiffen Company 2020, ZHIYUN-TECH 2021)

Cable camera systems are widely used in sport events, music festivals and in the movie industry. References include lots of both indoors and outdoors footage from events like FIS Nordic world ski championship 2017 in Finland, the Oscars 2019-2020, film shooting of Molly's game and 2020 Biathlon IBU World Cup. Cable cams are proven to be capable of carrying out challenging tasks with strict requirements. (Motion Compound Engineering 2021b, Newton Nordic 2021)

Air Drone Craze (2021) divides the drones into 7 generations. The first generation includes all forms of basic remote-control aircrafts. The second generation drones have static design, and they are still manually controlled. They come with a fixed camera mount and the ability to take still photos and record video. The third generation's design is still static, but control is assisted, and they come with basic safety modes, 2-axis gimbal, and a camera to record HD video. In the fourth generation the design has changed to a transformative one and safety modes are also improved. Their gimbals are upgraded to have 3 axes and they have cameras which can capture at least 1080p HD video. Autopiloting mode is introduced for the first time in the generation 4 models. The fifth generation devices come with more intelligent piloting modes, and they have 360° gimbals and the capability to record 4K or higher quality video.

Drone generations above the fifth generation are suitable for commercial use. Currently drone technology is in its sixth generation. The drones' design is now based on safety and regulatory standards, and they have intelligent controlling modes with automated safety features. Sixth generation models are adaptable to different platforms and payloads. They have full awareness of their surroundings in air and can operate autonomously. The seventh generation technology design is fully compliant with safety and regulatory standards. They have interchangeable platforms and payloads. Piloting modes are enhanced, and drones can perform landing, taking off and other actions on their own. (Air Drone Craze 2021)

2.3.1 Cable camera systems

The aforementioned SkyCam is basically a camera, which is hung with four cables. The cable-suspended camera's movement is controlled with reels by altering the cables' length. This type of cable cam system is 3 dimensional. There are also 2 dimensional cable cam systems which can move in specified direction along one cable but also up and down. They require less reels and winches than the 3 dimensional cable cam systems. Point-to-point cable cam systems, for example 1D Cable Cam from Newton Nordic and MCE_CC_AEC_18 from Motion Compound Engineering, differ from cable cam systems with multidimensional motion. Their motion is generated with a motor which is attached to the same body as the camera. In one dimensional cable cam systems the cables do not produce the movement. The driving wheel is placed on the cable in such a way that rotating it produces the translational motion of the camera system. (Newton Nordic 2021, SkyCam 2021)

When using a 1 dimensional cable cam system, it is beneficial to know about the cable's shape while it is hanging freely from the anchoring points. The shape which the cable forms can be described by the catenary equation. The catenary equation approximates the ideal situation where cable hangs from two same height anchoring points. This equation considers no other forces than the tension force and uniformly distributed cable's own weight.

Cable will be tensioned with force T. Ideally cable's shape can be described as Equation 1.

$$y = a \cdot (\cosh\left(\frac{x}{a}\right) - 1), \tag{1}$$

Equation 1 is a general equation of the catenary curve, where x is distance between anchoring points of the cable and the parameter a is defined in Equation 2

$$a = \frac{T_0}{g \cdot q}, \tag{2}$$

where T_0 is vertical tension force [N],
g gravitational acceleration [m/s^2] and
q distributed weight of the cable [kg/m].

With Equation 1 it is easy to calculate sagging of a cable by substituting half of the distance between the anchoring points in the x, which then forms Equation 3

$$h_{\text{sag}} = a \cdot \left(\cosh\left(\frac{L}{2 \cdot a}\right) - 1\right), \tag{3}$$

where L is the distance between poles where the cable is hung.

Equation 4 can be used to plot the catenary shaped curve to the right height

$$y_{\text{cable}} = y + (h - h_{\text{sag}}), \tag{4}$$

where h is the height of the anchorage.

In Figure 4 a curve representing the shape of a cable is plotted in MATLAB by using Equation 4 with appropriate values to form a visible arc. The forces acting on a small segment of the cable which are then used in mathematical proof of Equation 1 are also shown.

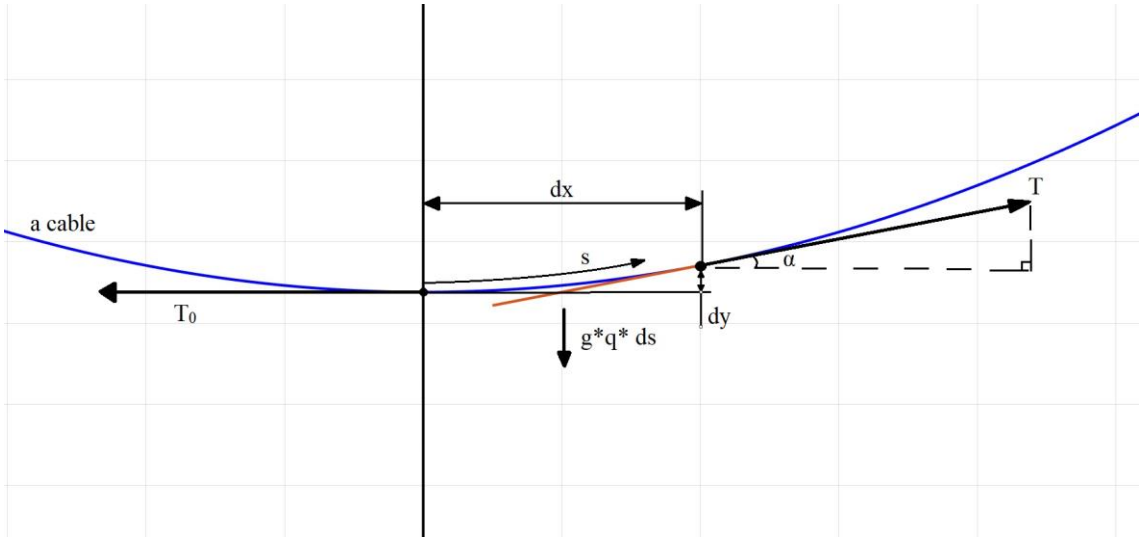

Figure 4. Catenary curve with tangent plotted with MATLAB.

Equation 5 uses the assumption that the force on the string remains constant. Equation 5 is derived from the forces in Figure 4.

$$\begin{cases} q \cdot g \cdot ds = T \cdot \sin(\alpha) \\ T_0 = T \cdot \cos(\alpha) \end{cases} \Rightarrow \tan(\alpha) = \frac{q \cdot g \cdot ds}{T_0} = \frac{dy}{dx} \tag{5}$$

Next by manipulating Equation 5 with Equation 6

$$\frac{ds}{dx} = \sqrt{1 + \left(\frac{dy}{dx}\right)^2}, \tag{6}$$

and then differentiating both sides with respect to x, the got result is Equation 7 as follows

$$\frac{q \cdot g}{T_0} \cdot \sqrt{1 + \left(\frac{dy}{dx}\right)^2} = \frac{d^2 y}{dx^2} \Rightarrow \frac{q \cdot g}{T_0} \cdot dx = \frac{d^2 y}{\sqrt{1 + \left(\frac{dy}{dx}\right)^2}}. \tag{7}$$

Equation 7 will simplify into Equation 1 after two integration operations and substitution of values determined by initial conditions. Initial conditions state that at x = 0 both y and $\frac{dy}{dx}$ are equal to zero.

Static calculations including the weight of a payload can be done as follows. First using an idealized approximation, that the cable's weight distributes uniformly across the whole length. The impact of this load is only half of the cable load concentrated on the centre point. Now an idealized resultant force which the cable's weight and the payload's weight exerts towards the ground is calculated with Equation 8 (Reinelt 2015, SFS-EN 1991-1-4 2010)

$$G = \gamma \cdot \left(m_{\mathrm{p}} + \sum l_{\mathrm{c}} \cdot q_{\mathrm{c}} \cdot 0{,}5\right) \cdot g, \tag{8}$$

where m_{p} is mass of the system, l_{c} cable's length in meters, q_{c} cable's distributed weight in kg/m and g acceleration of gravity in m/s^2. γ is a safety factor.

The wind force F_{w} acting on the structure may be determined by using Equation 9. Equation 9 is a modified version of the equation in SFS-EN 1991-1-4 (2010 p. 45).

$$F_{\mathrm{w}} = \gamma_{\mathrm{G}} \cdot (c_{\mathrm{s}} c_{\mathrm{d}} \cdot \sum c_{\mathrm{f}} \cdot q_{\mathrm{p}}(z_{\mathrm{e}}) \cdot A_{\mathrm{ref}}), \tag{9}$$

where γ_{G} is the partial safety factor for permanent actions in amusement devices. The force itself consists of the structural factor $c_{\mathrm{s}} c_{\mathrm{d}}$, the force coefficient for the structure or structural element c_{f}, the peak velocity pressure $q_{\mathrm{p}}(z_{\mathrm{e}})$ at reference height z_{e} and the reference area of the structure or structural element A_{ref}.

The force coefficient c_f is determined in SFS-EN 1991-1-4 (2010 p. 131) with Equation 10 as follows

$$c_f = c_{f,0} \cdot \psi_\lambda, \tag{10}$$

where ψ_λ is defined as the end-effect factor and $c_{f,0}$ is the force coefficient of structural elements without free-end flow.

The peak velocity pressure $q_p(z_e)$ is determined in SFS-EN 1991-1-4 (2010 p. 41) with Equation 11 as follows

$$q_p(z_e) = c_e(z) \cdot 0{,}5 \cdot \rho \cdot v_b^2, \tag{11}$$

where $c_e(z)$ is the exposure factor, ρ is air density and v_b is basic wind velocity.

The reference area of the structure or structural element A_{ref} can be calculated with Equation 12

$$A_{ref} = \begin{cases} \sum w \cdot h, & \text{cable cam system} \\ b \cdot l_c, & \text{cable} \end{cases}, \tag{12}$$

where w is the width and h is the height of the cable cam system in the direction of wind. The b is diameter and l_c the length of the cable.

Now the resultant force acting on the cable is the vector sum of the forces defined in Equations 8 and 9. Applicable coefficients φ need to be considered due to dynamic factors, when this resultant force is calculated by using Equation 13.

$$F_{tot} = \varphi \cdot \sqrt{G^2 + {F_w}^2} \tag{13}$$

Maximum force acts on the cable when the cable cam system is in the middle of the cable. The angle which the cable forms with horizontal plane in anchoring point can be calculated with Equation 14

$$\alpha = \tan^{-1}\left(\frac{D}{0{,}5 \cdot l}\right), \tag{14}$$

where α is the angle, D is the sag in meters and l is the length of the cable in meters.

Maximum force the cable cam system exerts to the anchoring point can now be calculated with Equation 15 depending on if the cable cam system is used indoors or outdoors.

$$F_C = \begin{cases} \frac{G}{2 \cdot \sin(\alpha)}, & \text{indoors} \\ \frac{F_{tot}}{2 \cdot \sin(\alpha)}, & \text{outdoors} \end{cases}, \tag{15}$$

where G is the force calculated with Equation 8, F_{tot} the force calculated with Equation 13 and α the angle calculated with Equation 14. The indoors part of Equation 15 considers only the cable cam system's weight, and the outdoors part considers both the cable cam system's weight and the wind forces.

2.4 Sensors' performance testing

Ouster has tested an OS1 LiDAR and a 4K GoPro camera in moderate rain. They conducted the test by placing the LiDAR and the camera on top of a car and driving around in the streets of San Francisco. The camera was used as a reference data of the image produced by LIDAR. The result was that rain degraded the camera's performance more than it did LiDAR's performance. LiDAR did better because it has larger aperture, faster shutter speed and ability to pick out strongest signals and ignore signals at other ranges caused by for example reflections. (Mardirosian 2020)

Perception sensors in robots and autonomous vehicles provide information of their surrounding environment. Performances of these sensors are affected by different weather conditions and environmental factors. Thus, evaluating the performance is important and the sensors' evaluation process should consider not only the optimal laboratory conditions but also changing weather and different environments.

Standardization of sensors' testing would make the comparison between different products easier and set clear, unequivocal, limitations for the sensors in different circumstances. Testing of different products with the same field of applications can vary between the manufacturers. Senior vice president of quality and validation at Velodyne, Dr Mircea Gradu, has stated that "There is far too much – sometimes misleading –

information on the precision, accuracy and range of lidar sensors. To be of value to the car manufacturers, all lidar sensors should be evaluated with the same measurements." (Burgess et al. 2020a) As the sensors are yet to be evaluated in such manners, reliability and performance of the sensors need to be established for oneself with reproducible experiments. (Burgess et al. 2020a)

2.4.1 Sensor's characteristics to define performance

Burgess et al. (2020a) have listed multiple important features of sensors which need to be tested and acknowledged. Angular/Spatial resolution defines how capable the sensor is to recognize two targets next to each other. Information of the targets' location can be acquired by using spatial resolution's information together with the range position. Range resolution defines the sensor's capability to discriminate between two targets located at different distances from the sensor. Other two important values to measure in range performance tests are the maximum and the minimum distances the target can be detected. The angle at which the sensor can detect incoming radiation or signal is called the sensor's field of view. (Burgess et al. 2020b pp. 2–7)

Maximum unambiguous speed and minimum detectable speed are important factors when testing a sensor's performance in speed measurements. Speed resolution describes the sensor's ability to distinguish speeds of two objects from each other while they are moving at different speeds. The smallest possible difference in relative velocity between the two objects, that the sensor still detects, is the sensor speed resolution. (Burgess et al. 2020b pp. 3–5)

When trying out a sensor's ability to track a target or targets, there are two main features. They are called tracking capability and capacity. Tracking capability describes if the sensor can track a target or targets and how well it can perform it. Capability is the result of combining tracking algorithm with speed and position estimates. Tracking capacity is the number of targets which can be tracked at the same time. (Burgess et al. 2020b p. 5)

It is important to know how responsive sensors are. Responsiveness describes how fast the sensor can give outputs to the user including information about the objects or environment it detects. Responsiveness consists of three main factors called update rate, object revisit rate and latency. Update rate is the same as frame rate. Object revisit rate

is the time it takes the sensor to detect the same object twice in the same location. Latency means how long it takes for information to travel between the imaging process and sensor output. (Burgess et al. 2020b p. 5)

One tool used to demonstrate the usability and limitations of certain waveforms is called ambiguity diagram. It represents the ambiguity function which is a two-dimensional autocorrelation of waveform in time and frequency. It can be used to select functional waveforms for different applications. The plotted ambiguity function has lobes, and these lobes are used to measure performance of a radar. Sidelobe level is the ratio between the main lobe's peak and the level of the first sidelobes. Integrated sidelobe ratio is the ratio between the main lobe's power and the power of all the sidelobes summed together. Both the sidelobe level and integrated sidelobe are evaluated along delay and Doppler domains. Delay represents the range and Doppler represents the velocity. Radiation patterns the transmitter and receiver antenna forms are called antenna patterns. Main lobe, back lobe and sidelobes can be identified from this pattern. (Burgess et al. 2020b pp. 6–7, Kiang and Li 2004 p. 684)

Probabilities which one needs to think about when evaluating sensors' performance are detection probability and false alarm probability. Detection probability refers to sensor's probability to detect the target when it is visible to the sensor. False alarm probability in turn is the probability for the sensor to detect the target even if the target is not visible. False alarms are harmful and the probability for them to occur increases when the detection probability is increased. Detection must be designed in a way that has high detection probability while minimizing the false alarms. (Burgess et al. 2020b p. 6)

Dynamic range of the sensor means the ratio between the power of the received signal's minimum and maximum values. The maximum and the minimum values are the extreme values which the sensor can still successfully use. A small dynamic range will, for example in cameras, cause the sensor to blind in bright light due to the saturation of the image sensor. On the other hand, if there is not enough light, the sensor will not be able to detect targets. In ultrasonic sensors the ultrasound signal is generated by the sensor itself meaning that the maximum value cannot be exceeded. Dynamic range is defined for ultrasonic sensors as the difference between linear operation's upper limit and the noise floor. Noise floor of a signal is the sum of all the noise sources' signals and other unwanted signals which the sensor receives. (Burgess et al. 2020b pp. 6–7)

3 THE CABLE DRONE

In this chapter the focus is on main functionalities of the chosen system. Requirements and preferable capabilities for the system are first listed. An overview of the customized cable drone with the portable sensor system as payload is shown Figure 5. The portable sensor system is presented more thoroughly later in chapter 4. Hinged truss tower structure which can be used to lift main and safety cables will be presented in this chapter.

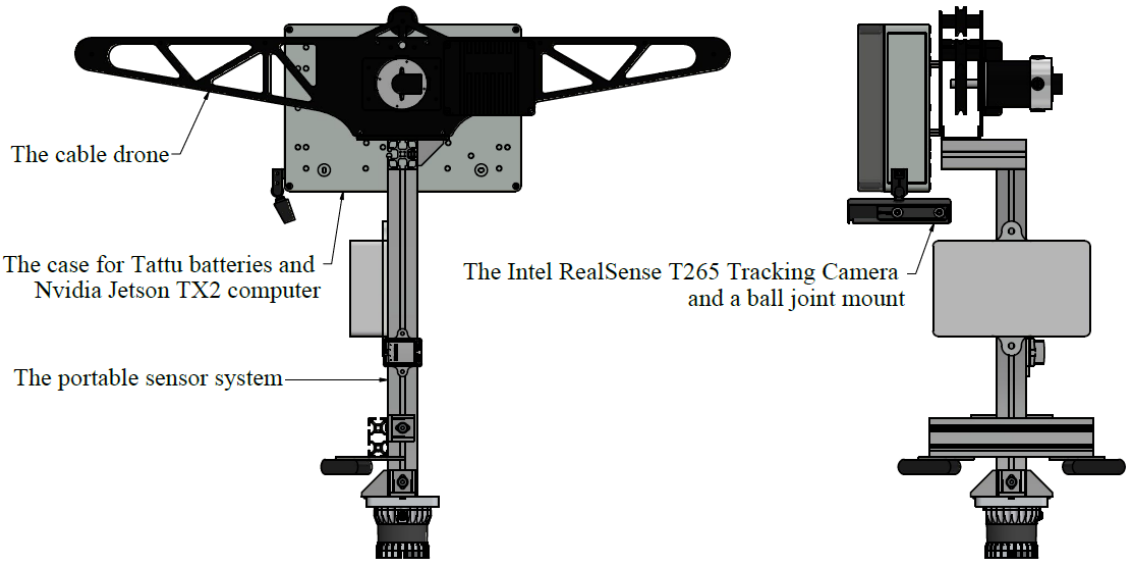

Figure 5. An illustration of the customized cable drone system with a payload.

3.1 System requirement specification

The selected system must implement a few requirements specifications. They contain aspects associated with safety, usability, and performance of the device. The importance of equipment safety goes without saying, so devices must be easily deployable and safe to use. The equipment is supposed to withstand a variety of weather conditions, including windy ones, so they should be usable at a wind speed of 15 m/s.

Practical things expected of the device include good transportability as it is meant to be used in different locations. Deployment itself shouldn't take too much time, so if there is need for installations, they should be possible to be prepared beforehand at the

wanted spot. The required equipment needs to fit in a regular passenger car if it is necessary to test equipment quickly without a van.

The chosen system should be able to carry a payload of 15 kg. The payload needs to be easily attached to the system itself. The speed is important in this application, and the system should be able to move at a decent speed of 5 m/s with the payload. Speed without payload is less important because it has insignificant role in tests, but preferably without a heavy payload the system should reach over 11 m/s speed.

The system should not require any additional licenses. This does eliminate a few possible alternatives, such as regular drones. A cable cam system seems to be a valid option. The cable cam system should have cable length of 200 meters and the cable should not sag more than 3 meters. The system can be modified to be controlled both manually and automatically. The cables must be able to lift in the air in a way that does not require climbing on ladders.

3.2 Basic information of the cable drone

The Motion Compound Cable Cam (rope camera system) is manufactured by Motion Compound GbR in Germany. The Motion Compound Cable Cam (hereinafter referred to as "cable drone") is to be used as a carrier sled. It shall be fitted with various sensors and measuring instruments when the system is being developed. Later, it can be used to carry sensors which are to be tested at the given time. In Figure 6, there is a simplified sketch of the cable drone system modelled in Inventor.

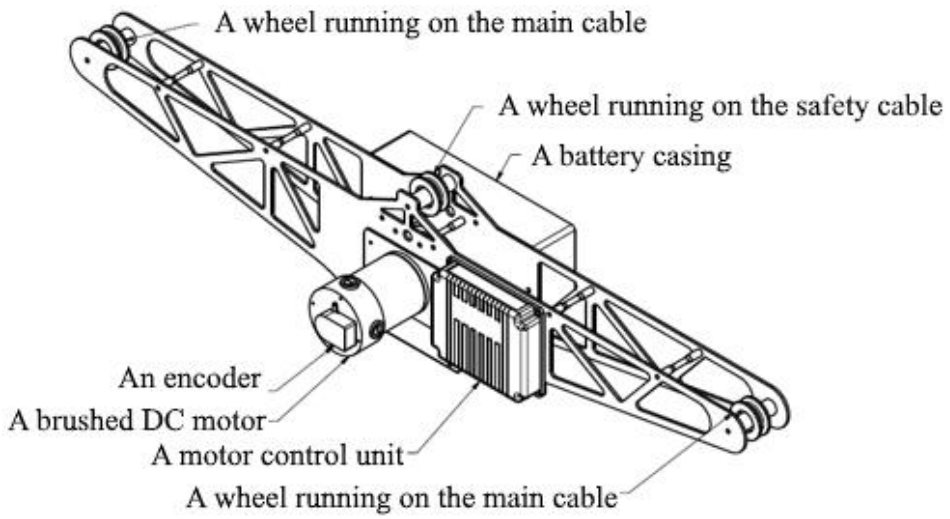

Figure 6. The cable drone system.

The cable drone requires two cables, the main cable, and the safety cable, to work properly. The drive wheel is located directly on the motor's shaft, and it is not visible in Figure 6. The tensioned main cable goes under two smaller wheels running freely on the main cable and over the driving wheel. As they are not in the same line, but they overlap slightly, the smaller wheels press the main cable to the driving wheel. The safety cable is also tensioned. It pulls up the cable drone and so it's increasing the force between the main cable and the driving wheel. An illustration of how the cable drone can be used with truss towers as anchoring points is shown in Figure 7.

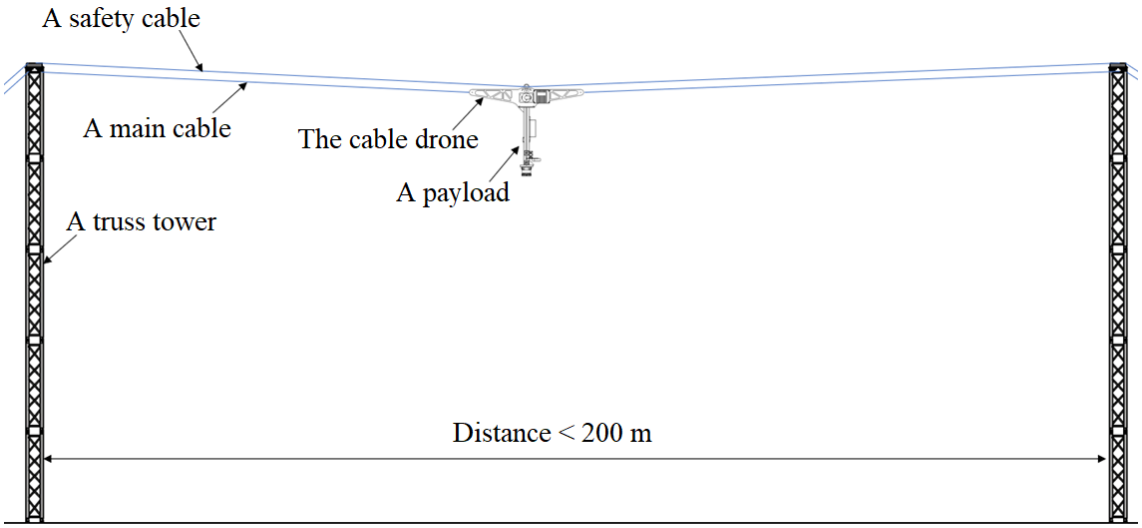

Figure 7. Basic setup of the cable drone.

The body is made of aluminium, and it weighs 3,85 kg alone. Its dimensions are 1000 x 220 x 230 mm presented as L x W x H. Surface is anodized to enhance corrosion resistance. Maximum payload of the cable drone is 15 kg. A cable's maximum slope should not exceed 9°. Speed of the system can be set from minimum 3 km/h to the maximum of 45 km/h. (Motion Compound Engineering 2018 p. 10–11)

The speed control is stepless as the power comes from a brushed electric motor A28-150-24. The motor itself is powered by LiPo batteries. Drive motor's connection values are 24 V for nominal voltage, maximum rated current is 98 A, and the installed power is 2,2 kW. Operating voltage for the motor is 14,8–25 V. Installed power is not the power which is supplied in practice as it is defined as the sum of nominal powers of all power consuming devices in the installation. The installed power refers to the output power of the driving shaft. The motor is operated as desired with a motor control unit. In the

cable drone's case, the control unit is manufactured by Roboteq. Control voltage of this motor controller is 4,8–6 V, rated current 150 mA and transmission power 90 mW. (Motion Compound Engineering 2018 p. 10–11, Motion Compound Engineering 2021a)

EU drone regulation EU 2019/947 has been into force since 31.12.2020. This regulation places all operators and remote pilots, except for those whose device is CE marked as a toy in accordance with the Toy Safety Act, as subject to a registration obligation. The aforementioned group is also obligated to comply with the UAS geographical zone. This regulation does not affect cable cam systems, so they can be used instead of UAV drones in order to avoid any violation of the regulation. It is also possible to attach a UAV drone to the cable drone if a licensed pilot is not available and data from the drone's sensors needs to be acquired. (Droneinfo 2021)

3.3 Controlling and modifications

In this cable drone system the motor controller is used to drive one brushed DC motor to which an encoder is connected. The motor used in the cable drone is AmpFlow A28-150-24. Roboteq MDC1460 motor control unit converts received commands from RC radio, Analog Joystick, wireless modem, PC or microcomputer into high voltage and high current output for the DC motor. Motor control unit is mounted on metallic surface to conduct the heat it generates during operation. Picture of the motor controller on top of the metal plate is shown in Figure 8. (RoboteQ 2018 p. 1)

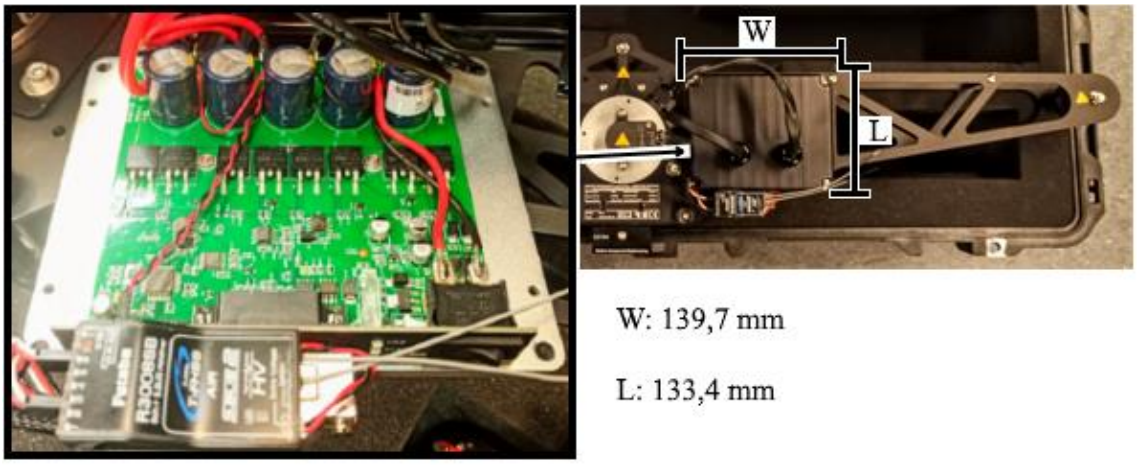

Figure 8. Motor control unit Roboteq MDC1460 and R3008SB receiver.

Automated driving can be achieved by using scripts written in MicroBasic language. As the controller responds to the commands from multiple different sources the command

priority order must be defined. This order can be changed with Roborun+ PC Utility. Roboteq MDC1460 responds to commands from RS232, 0–5 V analog and pulse command modes. Controller has the ability to change automatically between these modes when a mode with higher priority becomes available. In this case the pulse command is transmitted with the T10J radio remote controller and received with the R3008SB. The receiver is shown in Figure 8 under the motor controller. (RoboteQ 2018 p. 1)

The encoder module used to collect information about rotatory position of the motor shaft is manufactured by Anaheim Automation. The encoder model is ENC-A5SN-1000-375-G. It is a single-ended, transmissive optical encoder which consists of a code wheel disk, an LED source lens and a monolithic integrated circuit covered with plastic housing. A code wheel is attached to the motor shaft and the optical module is aligned with the code wheel. (Anaheim Automation 2021a, Anaheim Automation 2021b)

Primary goal is to find a way to control the position of the cable drone as it moves along the cables. In chapter 6 results of different tests are shown which lead us to choose Intel RealSense Tracking Camera T265 for this application. Automation of the driving sequence is done with a python script which uses commands from a library with all the needed MicroBasic commands. Jetson TX2 runs the python script and controls the tracking camera. Control diagram of this system is shown in Figure 9.

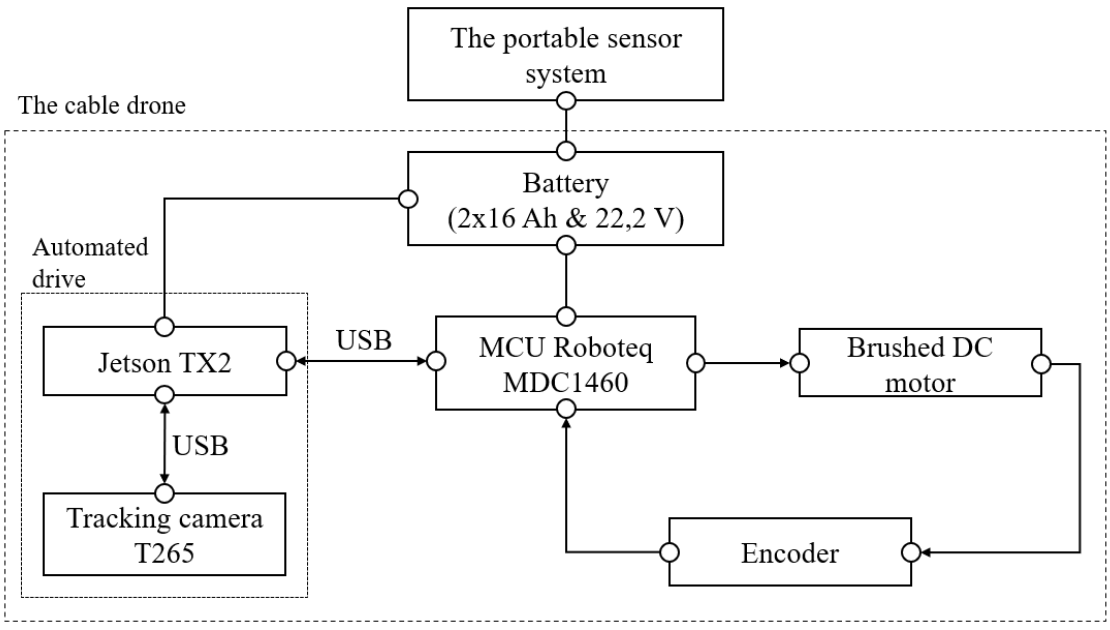

Figure 9. Schematic diagram of the modified cable drone with tracking camera.

Inter RealSense T265 is a tracking camera for SLAM applications based on a combination of visual inertial odometry and IMU odometry. It is a computer vision device which provides data of 6 DoF (degrees of freedom) poses. T265 is equipped with two OmniVision's OV9282 high-speed global shutter image sensors with fisheye lenses and Bosch's BMI055 IMU. The IMU has higher update frequency than the image sensors do, but the IMU is also prone to drift over the course of time due to lower stability. Re-localization can be done with data from visual odometry. The camera is shown in Figure 10 on the bottom right corner of the case. (Brook et al. 2020, Intel 2019 pp. 7–8)

A T265 can store and export maps it constructs for other applications to use. This is called cooperative mapping. As SLAM algorithms can be computationally expensive, it is not optimal to leave this task for the host computer, which in this case is the Jetson TX2. A T265 runs the algorithms itself on an embedded Intel Movidius Myriad 2 vision processing unit which enhances CPU utilization and memory usage on the host computer. (Brook et al. 2020)

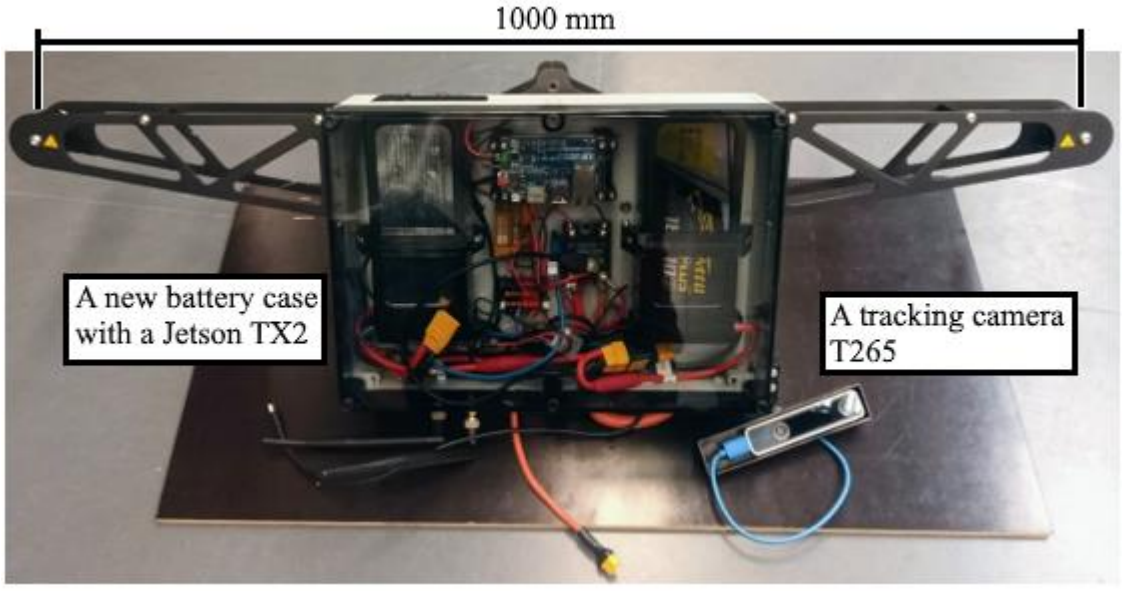

Figure 10. Modified cable drone with Intel RealSense T265 tracking camera.

With double fisheye lenses the T265 has a circular FOV (field of view) of 163°. OV9282 uses a sensor with 848x800 active pixels to capture monochrome images. Sample rate of BMI055 IMU's accelerometer is 200 Hz and gyroscopes 62,5 Hz. The host platform receives pose data at sample rate of 200 Hz over USB. (Intel 2019 pp. 9–10)

The most visible modification is the new battery case for two Tattu Plus 16000 mAh 6 S 15 C 22,2 V Lipo Batteries. The case has enough room for the Jetson TX2 which controls the cable drone's motor controller. The case is equipped with a power switch. The cable drone and the new battery case with the batteries, Jetson TX2 and the T265 camera are shown in Figure 10. The camera is on the bottom right corner of the case in its own fastening frame equipped with a ball joint.

The Jetson TX2 runs the code which has a socket-client connection to another computer via Wi-Fi hotspot the TX2 makes. This way the values for acceleration, deceleration, and desired power or speed can be changed remotely. The code is also used to switch between manual and automated drive modes. Endpoints of the automated drive can be set by driving the cable drone in manual mode to the desired position and sending a command "positionA" and then proceeding to the other end and sending a command "positionB".

When the endpoints are set, and drive mode is switched to the automated driving, the cable drone will drive from one point to another and then stop until direction is switched from forwards to backwards or vice versa. This single mode is set as default for automated driving. If the cabledrone is wanted to drive back and forth between the endpoints, the mode can be switched to the roundtrip mode. As a safety feature in the automated drive mode, the code halts the motor's rotation when the remote controller's left switch is not in the top position. This acts as a dead man's switch, as the switch returns to the center position when not held.

Motor controller supports different control modes. In the Open Loop Speed -mode, the Go to Speed -commands given for the controller sets the desired power output level to be applied to the motor. For example, a command "speed 200" sets power to 20% and correspondingly "speed 500" sets power to 50%. When using the same command in Closed Loop Speed -mode, the given value sets speed in relation to maximum speed stored in corresponding configuration parameter MXRPM. This means that if for example the value 4000 is stored in MXRPM parameter, the Go to Speed -command with the value 500 sets speed to 50% of the MXRPM value so the controller commands the motor to go to 2000 RPM. Closed Loop Speed -mode will not be used in the tests of this master's thesis.

3.4 Anchorages

Cable drone a requires safety cable and main cable to operate. These cables must be attached to rigid places and tensioned so that the safety cable is about 15 cm over the main cable. Even though large trees are indeed sufficiently sturdy anchor points for the cables, it was decided to acquire suitable trusses for a tower structure where the cables can be fixed. This broadens the number of possible testing locations considerably. Trusses can then also be used in other applications such as configuration points for UAV drones.

The comparison of trusses took into account aspects of both transportation and rigidity. Trusses are connected to each other with conical connectors which are locked in place with pins. To minimize the amount of these connection points, the longest suitable trusses that satisfy the transport requirements were compared with each other. Excessive number of joints could result in unwanted motion and precarious structure. To avoid confining the possibilities of transport and storage, one truss has a maximum length of 1500 mm. The structure is meant to reach the height of 7500 mm, so five of these trusses are needed. The number of joints is quite large for a structure this tall, so the structure is stiffened by other means. The truss' main pipes' outer diameter and the wall thickness shall be sufficiently large to withstand static stress exerted on the highest point of the truss.

Comparison resulted in the acquisition of 10 pieces of Global Truss' F34150P trusses. They are 1,5 m tall straight 4-point truss. The main pipe has diameter of 50 mm and increased wall thickness from 2 mm to 3 mm. F34150P has the same dimensions as regular F34150; 1500x290x290 mm. One of the trusses is shown in Figure 11. Four vertical aluminium tubes are the main pipes, and they are connected to each other with horizontal and diagonal braces. Braces are 20 mm diameter aluminium tubes with 2 mm wall thickness. One F32150P truss weighs 12 kg.

Figure 11. Global Truss F34150P with top base plate.

In addition to the basic truss structure, Figure 11 also shows the end plate on the top. End plates are required for installing a cable guider system on top of the tower and a hinge to the bottom. Towers are to be assembled on the ground and then lifted into place. The cables must be securely on the cable guider so that they will not fall off when lifting the tower. A couple of different mechanisms were designed to keep the cables in place. In Figure 12 the top base plate with the cable guider is shown with a cap that prevents the safety cable from falling while simultaneously acting as a cover for the bearing-mounted axles. The base plate weighs 1 kg. Pillow block ball bearing units with sheet metal housing and shaft diameter of 30 mm are used to hold the cables in place. One set of bearing- mounted axles weighs 1,5 kg, so the top of the tower weighs approximately 7,5 kg.

Figure 12. Top of the tower.

Truss towers are anchored to the ground with a ground base and guy-wires. One 800 mm long screw pile is attached to a 430x430x8 mm steel plate with six M10 bolts to act as the ground base. The screw pile is screwed into the ground so that the flat bracket is at the same level with the ground as shown in Figure 13. Same kind of aluminium base plate as the one on top is used at the bottom end. The aluminium plate is hinged to the steel plate to ease the lifting of the fully assembled tower. Hinged plates of the ground base weigh together 14 kg.

Figure 13. The screw pile and the assembly tools.

The aluminium plate has a hole in the middle to make room for the fastening bolts. The

primary purpose of bolts is to attach the metal plate to the screw pile, but they are also used to fine-tune the angle of the metal plate. The metal plate has long holes for the bolts so that the direction can also be adjusted without rotating the screw pile. Assembled ground base is shown in Figure 14. As the tower is lifted the aluminium plate will be bolted to the metal plate with 3 M12 bolts. The holes for the M12 bolts are also long holes, so the threaded holes are accessible even if the tower would move slightly when lifting it. It is expected that the tower may move slightly when raised upright. The hinge shafts are left slightly loose, and their diameter is a little bit smaller than the diameter of their mounting holes so that they would not resist lifting.

Figure 14. Assembled ground base with assembly tools.

First the truss tower is assembled horizontally on the ground. The main and safety cables are placed on the bearing-mounted axles and anchored to the ground. Smaller, also screwable, ground anchors with an eye for hooks and straps are used for anchoring the guy-wires and the cable drone's cables. Even though the truss towers are free standing structures with the ground base, three galvanized steel wires with 5 mm thickness are used as guy-wires to stabilize the structure. Each guy-wire is tightened with ratchet cable pullers attached to the ground anchors with 10 mm snap hooks. The

guy-wires' breaking load is 11,2 kN. A truss tower and the cable drone are shown in Figure 15.

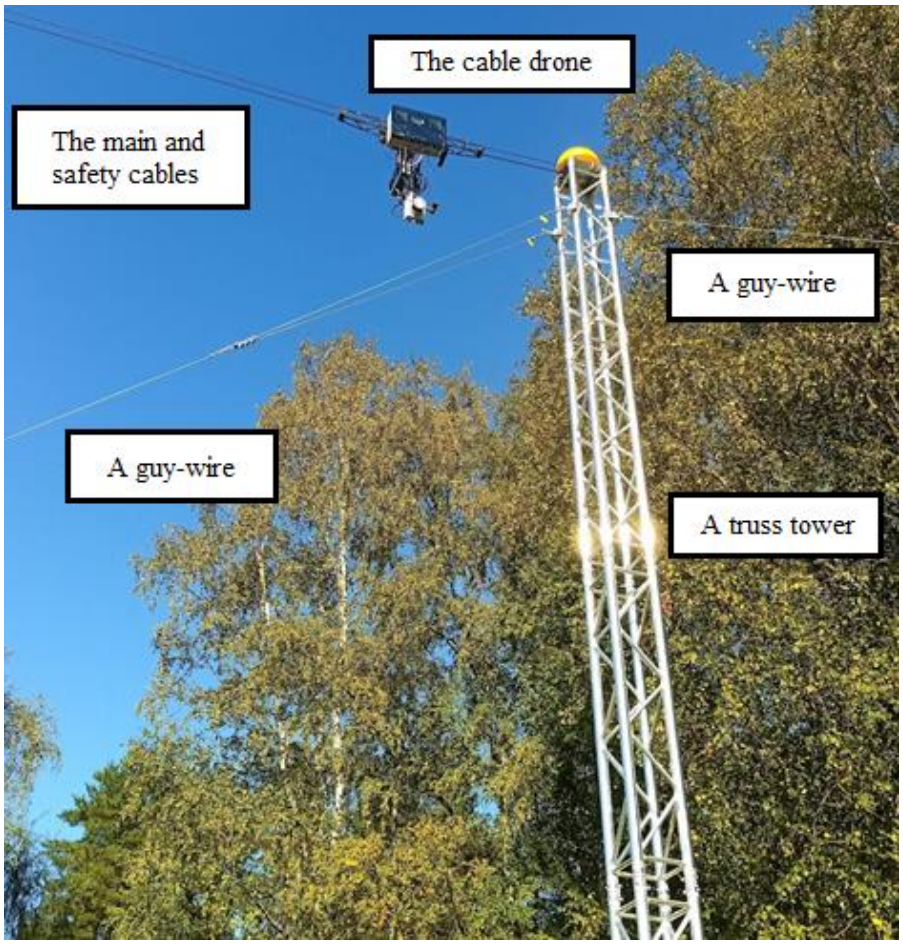

Figure 15. A truss tower and the cable drone.

One end of a cable can be anchored straight to the ground. However, if the ground anchors for cables are anchored firmly enough, the cables can be tightened with one pulling hoist at one end. This way cables can be tightened simultaneously with desired force. Fine tuning for the cable's tension can be done from the other end, where both cables are anchored separately with ratchet cable pullers.

3.4.1 Cables and static calculations

Consider the situation where the cable drone's main cable and safety cables are assembled to hang from their ends and the ends are at the same height. This is the case when the cable drone is not on the cables. This situation should be taken into consideration as the cables will be left hanging in their place even when the cable drone is not in use. A catenary equation can be used to estimate how much force is needed to tension the cables. Tension force will affect how much the cables will sag and thus it

can be used to estimate how high the cables need to be anchored so that they will not interfere with other activity in the area.

Figure 16 shows an example of a situation where two cables are hung with values stated in Table 1. Equation 4 is used to plot the curves. By using the catenary equation, the tensioning force required to lift the cables out of the way can be estimated while the cable drone is not attached.

Table 1. Values used to plot curves in Figure 16

Abbreviation	Value safety cable	Value main cable	Definition
T_0	500	500	Vertical tension force [N]
g	9,81	9,81	Gravitational acceleration [m/s^2]
q_c	0,024	0,045	Cable's weight per meter [kg/m]
l_c	100	100	Distance between the poles [m]
h	7,6	7,4	Height of the anchoring points [m]
h_{sag}	0,58	1,12	Sag on the cable [m]

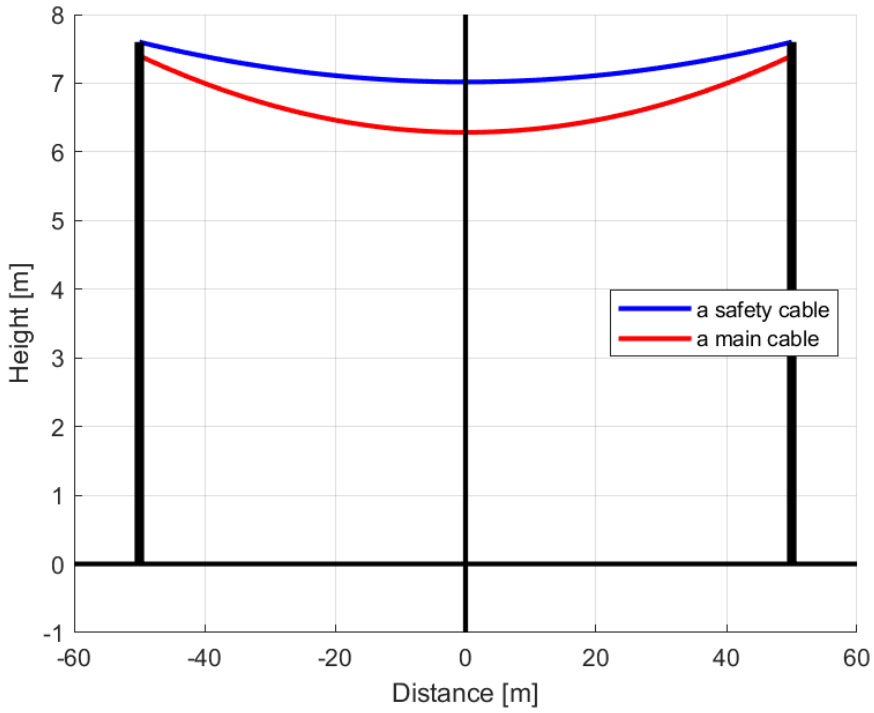

Figure 16. An example of a situation where cables are hung between poles.

This catenary equation is an approximation of an ideal situation where cable hangs from two same height and it does not consider other forces than the tension force and uniformly distributed cable's own weight. In the situation where the cable is hung outside, and the cable drone is running on it, there will be more weight and forces to consider. The Motion Compound GbR has provided some information on one of their similar devices. This information is now used in the static strength calculation for anchorage. (Reinelt 2015)

Weight of the payload and the cable can is calculated with Equation 8. The safety factor γ, given in standard SFS-EN 13814-1, for unfavourably acting proportion of the dead load is 1,1. Maximum mass of the cable drone M_{p} is 15 kg. Cables' weight per meter are the same as used in the Table 1 so $q_{\mathrm{c,main}}$ is 0,045 kg/m and $q_{\mathrm{c,safety}}$ is 0,024 kg/m. Results are shown in Table 2. All the forces include safety factor γ. The first row has the safety cable's weight, the second row has the main cable's weight, the third row has the drone's weight and on the last row these values are used in Equation 8.

Table 2. Calculated forces the cables' and the cable drone's weight exert to the anchorages with different lengths

Length [m]	25	50	75	100	125	150	175	200	
Force [N]	3,20	6,40	9,60	12,80	16,00	19,20	22,40	25,60	safety
	6,13	12,27	18,40	24,53	30,80	36,80	42,93	49,07	main
	161,87	161,87	161,87	161,87	161,87	161,87	161,87	161,87	drone
	171,20	180,53	189,86	199,20	208,53	217,86	227,20	236,53	total

Some further definitions are needed in order to calculate the force which the wind actions exert to the system with Equation 9. The safety factor γ_{G}, given in standard SFS-EN 13814-1, for permanent actions in amusement devices is 1,35. The structural factor $c_{\mathrm{s}}c_{\mathrm{d}}$ can be considered in this case as 1.

Equation 10 gives value for the force coefficient c_{f}. Motion Compound Engineering provided values for similar cable camera system, and they correlate with standard SFS-EN 1991-1-4 (2010). (Reinelt 2015) The force coefficient of the cables is 1,2. The value for the end-effect factor $\psi_{\lambda,\mathrm{drone}}$ is 0,7 and for the value the force coefficient of structural elements without free-end flow $c_{\mathrm{f,0,drone}}$ is 2,0.

Force coefficients used in the calculations are:

$$\begin{cases} c_{\mathrm{f,cable}} = 1{,}2 \\ c_{\mathrm{f,drone}} = 2{,}0 \cdot 0{,}7 = 1{,}4 \text{ (Equation 10)} \end{cases}$$

According to the SFS-EN 1991-1-4 (2010), the peak velocity pressure $q_{\mathrm{p}}(z_{\mathrm{e}})$ can be calculated by using the value 1,5 for the exposure factor $c_{\mathrm{e}}(z)$. The air density ρ is 1,25 kg/m^3. The system requirement specify that it must be possible to use the cable drone at a wind speed of 15 m/s, thus basic wind velocity v_{b} is 15 m/s. Now the peak velocity calculated with Equation 11:

$$q_{\mathrm{p}}(z_{\mathrm{e}}) = 1{,}5 \cdot 0{,}5 \cdot 1{,}25\ \mathrm{kg/m^3} \cdot (15\ \mathrm{m/s})^2 = \ 0{,}2\ \mathrm{kN/m^2}$$

The reference areas A_{ref} of the cable drone and the cable which the wind affects approximated by using Equation 12, and the results are:

$$\begin{cases} A_{\mathrm{ref,safety}} = 0{,}006\ \mathrm{m} \cdot l_{\mathrm{c}} \\ A_{\mathrm{ref,main}} = 0{,}008\ \mathrm{m} \cdot l_{\mathrm{c}} \\ A_{\mathrm{ref,drone}} = 0{,}5 \cdot 1\ \mathrm{m} \cdot 0{,}25\ \mathrm{m} + 0{,}2\ \mathrm{m} \cdot 0{,}5\ \mathrm{m} = 0{,}23\ \mathrm{m^2} \end{cases}$$

Now the required values are known, and the wind force can be calculated with Equation 9. Results of the calculations are shown in Table 3. The wind load on the rope is comparable to its own weight over the entire length and thus causes only half the loads as an equivalent central point load. The wind load on the rope is reduced by a factor of 0,5. (Reinelt 2015)

$$\begin{aligned} F_w = \ & \gamma_{\mathrm{G}} \cdot q_{\mathrm{p}}(z_{\mathrm{e}}) \cdot \left[\left(c_{\mathrm{f,cable}} \cdot 0{,}5 \cdot \left(A_{\mathrm{ref,safety}} + A_{\mathrm{ref,main}} \right) \right) + \left(c_{\mathrm{f,drone}} \cdot A_{\mathrm{ref,drone}} \right) \right] \\ & = 1{,}35 \cdot 0{,}2\ \mathrm{kN/m^2} \cdot [1{,}2 \cdot 0{,}5 \cdot (0{,}006\ \mathrm{m} \cdot l_{\mathrm{c}} + 0{,}008\ \mathrm{m} \cdot l_{\mathrm{c}}) + 1{,}4 \cdot 0{,}23\ \mathrm{m^2}] \end{aligned}$$

Table 3. Calculated wind forces the cables and the cable drone exert to the anchorages with different lengths

Length [m]	25	50	75	100	125	150	175	200	
Force [N]	24,3	48,6	72,9	97,2	121,5	145,8	170,1	194,4	safety
	32,4	64,8	97,2	129,6	162	194,4	226,8	259,2	main
	86,94	86,94	86,94	86,94	86,94	86,94	86,94	86,94	drone
	143,64	200,34	257,04	313,74	370,44	427,14	483,84	540,54	total

Now from Tables 2 and 3 the total values are used in Equation 13 to calculate the resultant force acting on the cable with dynamic factors taken into account with appropriate coefficient. Applicable coefficient φ due to unfavourably acting wind loads is 1,2 according to the SFS EN 13814-1:2019. The forces calculated with Equation 13 are shown in Table 4.

Table 4. Total force due the weight and wind calculated with Equation 13

Length [m]	25	50	75	100	125	150	175	200	
Force [N]	171,2	180,5	189,9	199,2	208,5	217,9	227,2	236,5	Dead load G
	143,6	200,3	257,0	313,7	370,4	427,1	483,8	540,5	Wind load F_{w}
	268,2	323,6	383,5	446,0	510,1	575,4	641,4	708,0	Total F_{tot}

The angle α which the cables form with a horizontal plane is calculated with Equation 14 in terms of sag D and cables length l_{c}, results are shown in Table 5. Then the angle α is used to calculate the maximum cable force with Equation 15.

Table 5. Angles which the cables form with a horizontal plane calculated with Equation 14

Angles [°]		Length l_{c} [m] 25	50	75	100	125	150	175	200
sag D [m]	0,5	2,29	1,15	0,76	0,57	0,46	0,38	0,33	0,29
	1	4,57	2,29	1,53	1,15	0,92	0,76	0,65	0,57
	1,5	6,84	3,43	2,29	1,72	1,37	1,15	0,98	0,86
	2	9,09	4,57	3,05	2,29	1,83	1,53	1,31	1,15
	2,5	11,31	5,71	3,81	2,86	2,29	1,91	1,64	1,43
	3	13,50	6,84	4,57	3,43	2,75	2,29	1,96	1,72

The results of angle α are used to calculate the cable forces with Equation 15. Before calculating the forces which both cables and the cable drone exert to the anchorages, main cable's permissible rated loads need to be calculated. Main cable's breaking load R_{B} is 32 kN so the maximum permissible rated load with appropriate safety factor 0,5 is (Reinelt 2015)

$$R_P = \frac{R_B}{\gamma} \cdot 0{,}5 = \frac{32\ \text{kN}}{1{,}1} \cdot 0{,}5 = 14{,}54\ \text{kN}$$

Next a situation where only the main cable is attached is considered to find the minimum sag at different spans so that the cable force remains within the permissible limits. Calculations are done with Equation 15, and the results are shown in Tables 6 and 7 for both indoors and outdoors situations. Forces which exceed the maximum permissible rated load R_P are marked in red.

Table 6. Total cable force on main cable. Indoors with different sag and cable length

F_C Indoors [kN]		Main cable length l_c [m]							
		25	50	75	100	125	150	175	200
sag D [m]	0,5	2,10	4,35	6,76	9,32	12,03	14,90	17,92	21,09
	1	1,05	2,18	3,38	4,66	6,02	7,45	8,96	10,55
	1,5	0,71	1,45	2,26	3,11	4,01	4,97	5,97	7,03
	2	0,53	1,09	1,69	2,33	3,01	3,73	4,48	5,27
	2,5	0,43	0,88	1,35	1,87	2,41	2,98	3,59	4,22
	3	0,36	0,73	1,13	1,56	2,01	2,49	2,99	3,52

Table 7. Total cable force on main cable. Outdoors with different sag and cable length

F_C Outdoors [kN]		Main cable length l_c [m]							
		25	50	75	100	125	150	175	200
sag D [m]	0,5	3,09	6,93	11,60	17,14	23,60	31,00	39,34	48,64
	1	1,55	3,47	5,80	8,57	11,80	15,50	19,67	24,32
	1,5	1,04	2,31	3,87	5,72	7,87	10,33	13,12	16,22
	2	0,78	1,74	2,90	4,29	5,90	7,75	9,84	12,16
	2,5	0,63	1,39	2,32	3,43	4,72	6,20	7,87	9,73
	3	0,53	1,16	1,94	2,86	3,94	5,17	6,56	8,11

From Table 6 can be seen that with over 125 metres of span the sag more than 0,5 meter when the cable drone is used indoors. Minimum sag for outdoors use is read from Table 7. For example, the same 125 meters span requires at least 1 m of sag when the cable drone is used outdoors. Now that the minimum sag is known with each span, situations where both cables are used can be evaluated. Equation 15 is used again, this time with values from Table 4 for dead load G and total force F_{tot}. Indoors situation is calculated with the dead load G and outdoors situation with F_{tot}. Results of the calculations for both situations are shown in Tables 8 and 9.

Table 8. Total cable forces. Indoors with different sag and cable length

F_C Indoors [kN]		Length l_c [m] 25	50	75	100	125	150	175	200
sag D [m]	0,5	2,14	4,51	7,12	9,96	13,03	16,34	19,88	23,65
	1	1,07	2,26	3,56	4,98	6,52	8,17	9,94	11,83
	1,5	0,72	1,51	2,38	3,32	4,35	5,45	6,63	7,89
	2	0,54	1,13	1,78	2,49	3,26	4,09	4,97	5,91
	2,5	0,44	0,91	1,43	1,99	2,61	3,27	3,98	4,73
	3	0,37	0,76	1,19	1,66	2,17	2,73	3,32	3,94

Table 9. Total cable forces with different sag and cable length

F_C Outdoors [kN]		Length l_c [m] 25	50	75	100	125	150	175	200
sag D [m]	0,5	3,35	8,09	14,38	22,30	31,88	43,16	56,13	70,80
	1	1,68	4,05	7,19	11,15	15,94	21,58	28,06	35,40
	1,5	1,13	2,70	4,80	7,44	10,63	14,39	18,71	23,60
	2	0,85	2,03	3,60	5,58	7,97	10,79	14,03	17,70
	2,5	0,68	1,63	2,88	4,47	6,38	8,64	11,23	14,17
	3	0,57	1,36	2,40	3,72	5,32	7,20	9,36	11,81

Table 8 shows that the maximum permissible load while used indoors is 13,03 kN and it occurs when span is 125 meters and sag 0,5 m. Outdoors-use is more interesting in the view of static calculations for the anchorage, as there are greater forces, and the calculations are made according to them. From Table 9 can be read, that the maximum permissible load 18,71 kN occurs when the span is 175 meters, and the sag is 1,5 meters. The truss towers and the anchorage need to bear this force. The calculations use the assumption that the cables are anchored at the same point, making the results slightly different from the actual situation. However, the results can be seen as a sufficiently accurate estimate.

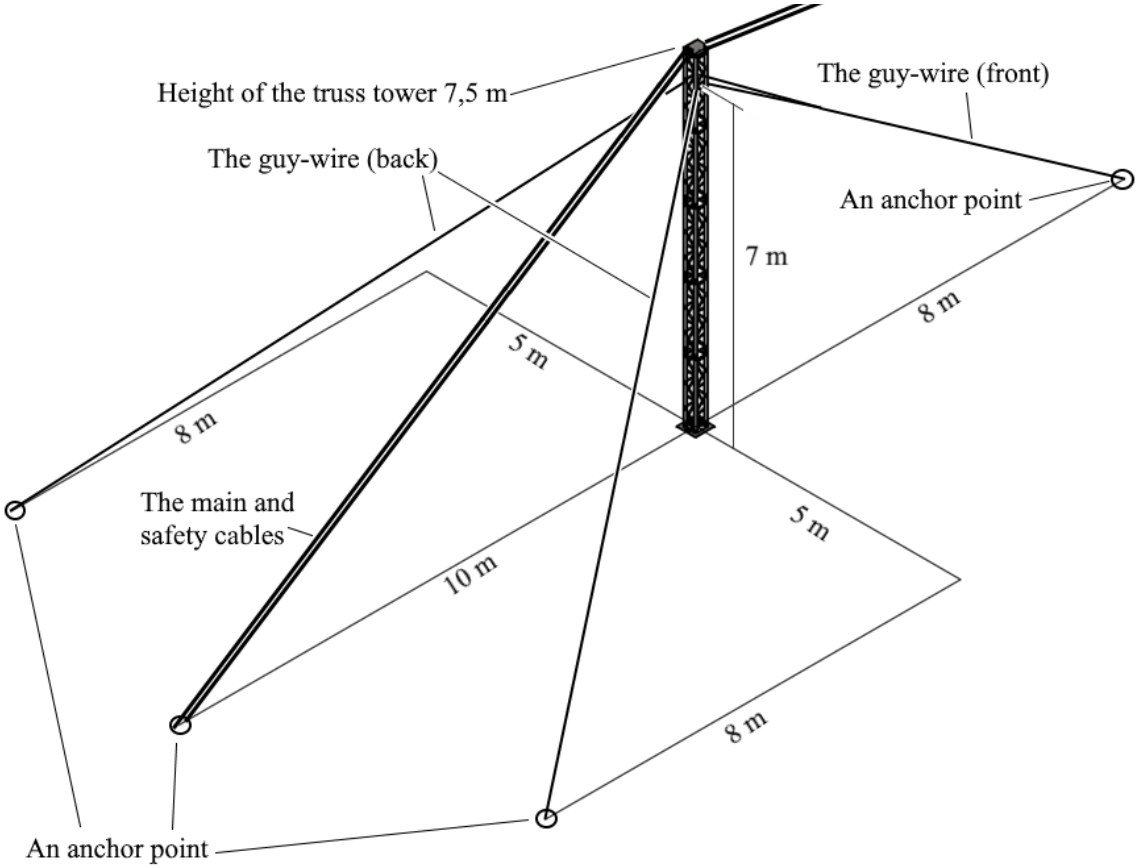

Figure 17. An oblique illustration of the truss tower, cables, and guy-wires.

In Figure 17 is a setup of the truss tower with three guy-wires. The guy-wire in the front branches into two parts so that the ends can be fixed symmetrically to the larger 50 mm pipes. By placing the anchor point of the main and cable on the ground, the direction of the unfavourable forces that the tower needs to bear can be changed. The further the anchor point is from the tower, the smaller the magnitude of the horizontally pointing force applied to the tower. If the cables would be anchored to the top of the tower instead of the ground, the tower would have to bear all the forces which the cables exert. In this application the main and safety cables' anchor point is 10 meters away from the tower.

A free-body diagram drawn from the situation according to Figure 17 is shown in Figure 18. From the forces visualized in Figure 18 can be derived a formula for the minimum bearing capacity of the tower's main ground anchor and the bolted connection. Derived equations for the horizontal and the vertical forces and the bending moment about the point A are shown in Equation 16.

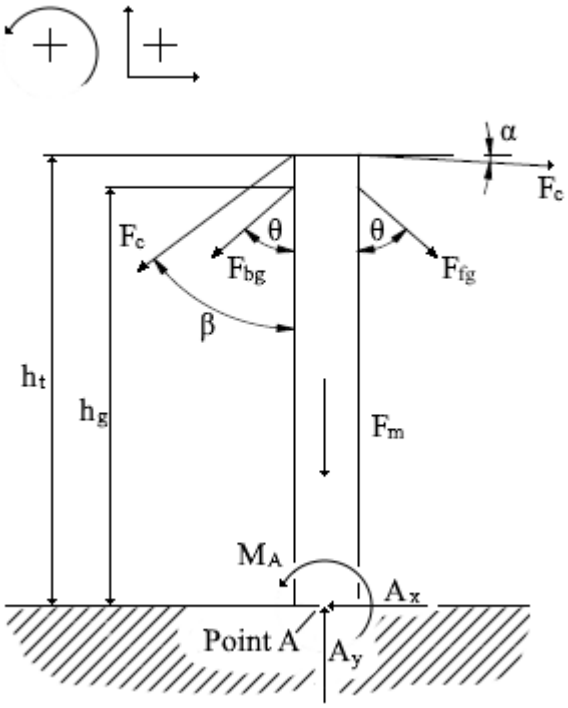

Figure 18. Free-body diagram of the truss tower.

$$\begin{cases} \rightarrow: F_{\mathrm{C}} \cdot \cos(\alpha) + F_{\mathrm{fg}} \cdot \sin(\theta) = A_{\mathrm{x}} + F_{\mathrm{C}} \cdot \sin(\beta) + 2 \cdot F_{\mathrm{bg}} \cdot \sin(\theta) \\ \uparrow: A_{\mathrm{y}} = F_{\mathrm{m}} + F_{\mathrm{C}} \cdot \sin(\alpha) + F_{\mathrm{fg}} \cdot \cos(\theta) + F_{\mathrm{C}} \cdot \cos(\beta) + 2 \cdot F_{\mathrm{bg}} \cdot \cos(\theta) \\ \mathrm{A}: F_{\mathrm{C}} \cdot \cos(\alpha) \cdot h_{\mathrm{t}} + F_{\mathrm{fg}} \cdot \sin(\theta) \cdot h_{\mathrm{g}} = M_{\mathrm{A}} + F_{\mathrm{C}} \cdot \sin(\beta) \cdot h_{\mathrm{t}} \\ \qquad\qquad +2 \cdot F_{\mathrm{bg}} \cdot \sin(\theta) \cdot h_{\mathrm{g}} \end{cases} \tag{16}$$

where A_{x} is the horizontal component of reaction force A [N],

A_{y} is the vertical component of reaction force A [N],

F_{C} is the force exerted by main and safety cables [N],

F_{bg} is the projected tension force of the guy-wire in the back [N],

F_{fg} is the tension force of the guy-wire in the front [N],

F_{m} is the force caused by mass of the structure [N]

h_{g} is height of the guy-wires anchoring point [m],

h_{t} is height of the truss tower [m],

M_{A} is the bending moment about the point A [Nm] and

α, β, γ are angles [°].

The guy-wires have breaking strength of 11,5 kN and they are tensioned with 10% of this force to stabilize the structure. Both front and back guy wires are tensioned with

1150 N. To use the projected force F_{bg}, as presented in Figure 18, the magnitude of the total tension force $F_{\mathrm{bg,tot}}$ needs to be reduced accordingly. Now the $F_{\mathrm{bg,tot}}$ is 1150 N so the projected tension force of the guy-wire in the back is calculated with Equation 17 as follows

$$F_{\mathrm{bg}} = F_{\mathrm{bg,tot}} \cdot \cos\left(\operatorname{asin}\left(\frac{5}{\sqrt{7^2 + 5^2 + 8^2}}\right)\right) = 1040{,}63 \text{ N} \tag{17}$$

The tension force F_{fg} is 1150 N as it points straight ahead.

Now let's consider the situation where the cables sag 1,5 meters at 175 meters span, so the main and safety cables exert the maximum force of 18,71 kN. The angle α is the same angle, which is calculated earlier with Equation 14, so it is

$$\alpha = \operatorname{atan}\left(\frac{1{,}5}{0{,}5 \cdot 175}\right) \approx 0{,}98°.$$

The anchor points are located as in Figure 17, so the angles β and θ are:

$$\begin{cases} \beta = \operatorname{atan}\left(\frac{10}{7{,}5}\right) \approx 53{,}13° \\ \theta = \operatorname{atan}\left(\frac{8}{7}\right) \approx 48{,}81° \end{cases}$$

The force caused by mass of the structure is calculated with Equation 18. As one F34150P truss weighs 12 kg, top of the tower 7,5 kg and ground base plates 14 kg, the force is

$$F_{\mathrm{m}} = g \cdot \sum m = 9{,}81 \text{ m/s}^2 \cdot (12 \text{ kg} \cdot 5 + 7{,}5 \text{ kg} + 14 \text{ kg}) \approx 800 \text{ N} \tag{18}$$

Substituting these values to Equation 16 gives the following result:

$$\begin{cases} A_{\mathrm{x}} = 3040{,}6 \text{ N} \\ A_{\mathrm{y}} = 14481 \text{ N} \\ M_{\mathrm{A}} = 23155 \text{ Nm} \end{cases}$$

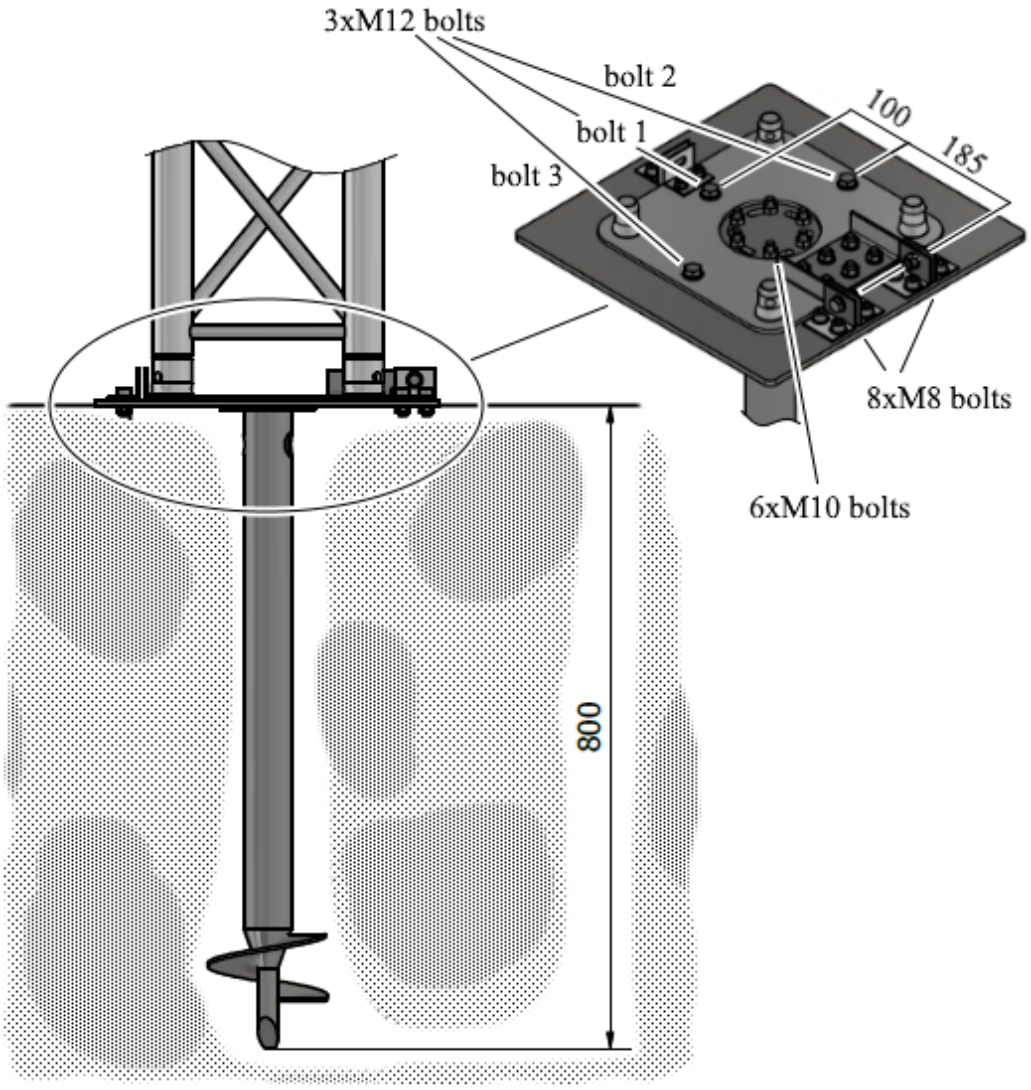

Figure 19. Simplified picture of the ground anchor

In Figure 19 shown screw pile anchor holds the ground plates in place. Six M10 bolts connect the steel plate to the screw pile. Four L-profiles serve as hinge bases and two M10 bolts as hinge pins. Each L-profile part is bolted to the steel plate with two M8 bolts. The three M12 bolts and the eight M8 bolts conduct the forces to the steel plate from which it is directed to the screw pile via the six M10 bolts. The screw pile then exerts all the forces to the ground. The M12 bolts also bear the amount of bending moment which can be derived from M_{A} and A_{y}.

Distances between the M12 bolts and the hinge's axle is shown in Figure 19. The force A_y and the moment M_A are reaction forces so the force and the moment point now to the opposite directions. Now the solved Equation 19 for the force on the M12 bolt 1 which is furthest away from the hinge axle is

$$F_b = \frac{\sum M \cdot (y_1 + y_2)}{\sum {y_b}^2} = \frac{(M_A - (A_y - m_{sp} \cdot g) \cdot y_2) \cdot (y_1 + y_2)}{((y_1 + y_2)^2 + 2 \cdot y_2^2)}, \quad (19)$$

where A_y is the vertical component of reaction force A [N]

F_b is the tensile force acting on a bolt [N],

g is the gravitational acceleration [m/s^2],

$\sum M$ is the sum of all moments,

M_A is bending moment about the point A [Nm]

m_{sp} is mass of the steel plate [kg],

y_1 is the distance to between bolts [m],

y_2 is the distance between bolts in the middle and the hinge axle [m] and

y_b is the distance between the bolt and the hinge axle [m].

Bolts 1, 2 and 3 are shown in Figure 19. As all the variables are known, the force in bolt 1 is calculated with Equation 19 as follows

$$F_b = \frac{(23155 \text{ Nm} - (14481 \text{ N} - 11{,}2 \text{ kg} \cdot 9{,}81 \text{ m/s}^2) \cdot 0{,}185 \text{ m}) \cdot (0{,}1 \text{ m} + 0{,}185 \text{ m})}{(0{,}1 \text{ m} + 0{,}185 \text{ m})^2 + 2 \cdot (0{,}185 \text{ m})^2}$$

$$\approx 39000 \text{ N}.$$

This means that M12 bolts with property class 8.8 or higher are suitable for this application as they have a proof load of 48900 N. Same kind of bolts are used as bolts 2 and 3.

4 THE PORTABLE SENSOR SYSTEM

The portable sensor system needs to be customizable rather quickly. The same portable sensor system should be usable in different applications besides the cable drone. Sensor setup should also be changeable to fit the current interest at given time. Various types of methods and materials were considered while deciding how sensors and cameras should be mounted. Mounting should extend the distance between measuring equipment and the cable drone. This minimizes drone's effect on measurements and pictures taken with mounted cameras.

Originally Motion Compound Cable Cam was equipped with an MCE QR-Mount shown in Figure 20. This mount is compatible with many camera stabilizers like for example DJI Ronin and Freefly Movi, but these will not be used in this project. The MCE QR-Mount is a firm and steady mounting device, but it does not quite fit our needs. The frame of the portable sensor system is quite long compared to its cross-sectional area. This means that in order to remain stable, the frame needs a larger contact surface with the cable drone's body than what the MCE QR-mount provides.

Figure 20. Detached MCE QR-Mount.

4.1 Basic design of the frame

New mount will have to endure changing weather conditions. At first, the plan was to make an extension piece from a steel rod or a steel pipe. The mounting piece would be fastened to the rod by screws, or it would be welded to it. In view of future use, it was decided to make the whole frame from aluminium. This way the weight will not become

an issue and there are a lot of possibilities for quick and easy modification in the aluminium profile. MiniTec Framing Systems' aluminium profile 45x45F pieces were ready in stock so prototyping with this profile was a logical choice.

Aluminium profile seems like a good option as it enables multiple possible attachment points for the sensors and various ways for quick modification of the frame. One of the first options tested for the portable sensor system's frame is shown in Figure 21. The black piece in Figure 21 is a bottom part from the original cable drone where an MCE QR-Mount was mounted. Now the MCE QR-Mount is replaced with an extension piece combined with a fastening part.

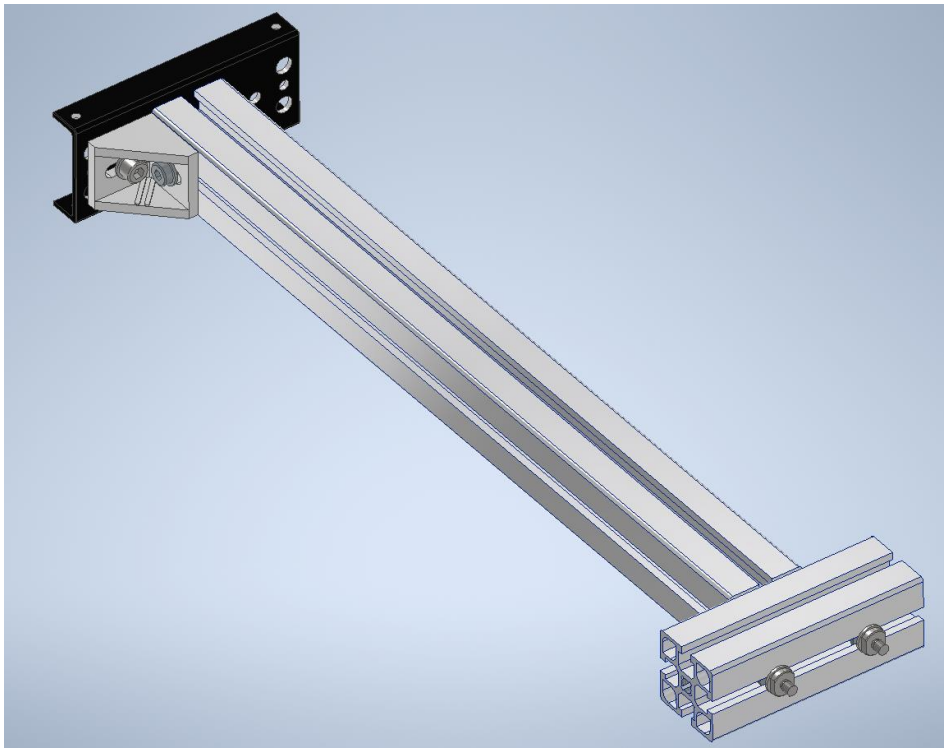

Figure 21. The extension piece with a fastening part in Autodesk Inventor.

Nuts with ISO metric screw threads are used to attach cameras and sensors to the frame. However, it is not always possible straight away, as it is common for cameras, stands and mounts to have ¼ inch thread. This problem is solved with an adapter bolt which has an M8x1,25 male thread and a ¼-20 UNC male thread. The design of the adapter is shown in Figure 22. The adapter makes it possible to quickly lock a thread to the desired location anywhere along the aluminium profile's slot with a M8 nut and then screw the cameras into place.

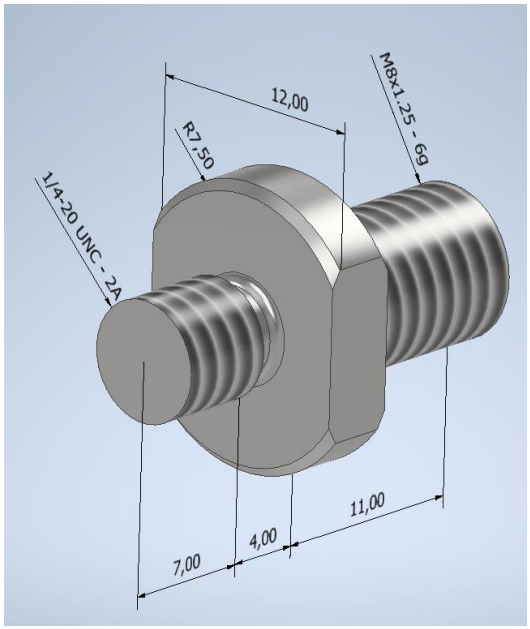

Figure 22. The adapter for M8x1,25 male thread to ¼-20 UNC male thread.

The first version of the frame went through some changes as the tests were carried out. The main idea remained the same; a long piece with several installation options for devices, expanding the distance between the sensors and the cable drone. The last version of the frame is shown in Figure 23. There the bottom end is left without the fastening part. The bottom end has an M8 screw thread drilled into it. Wider fastening part is attached higher to the frame. This makes the bottom end a good place for a rotating sensor with limited field of view, which in our case is a LiDAR sensor.

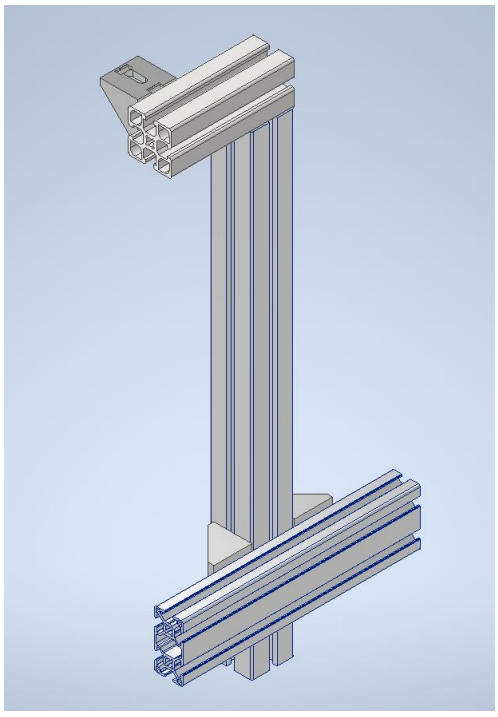

Figure 23. The frame of the portable sensor system.

The horizontal extension piece on top of the vertical frame is easily detached. This way the extension piece can be attached permanently to the cable drone's original bottom plate, shown in Figure 21, without the rest of the heavier payload. Later, when the cables are ready on the wheels and the extension piece is in its place, the rest of the portable sensor system's frame can be easily slid into the extension piece's slot and tightened into place with a Power-Lock fastener. The extension piece is required to balance the weight. In other words, it restores the centre of mass back to the middle when the cable drone uses heavier batteries and the Jetson TX2.

4.2 Attachments

The portable sensor system can be equipped with different cameras. In this project, two Logitech's BRIO 4K pro webcams, shown in Figure 24, are used. BRIO 4K is relatively small sized, its dimensions are 102x27x27 mm, and it is quickly mountable with ¼ inch bolt. BRIO can take ultra-HD resolution 4K (4096 x 2160 pixels) pictures at a rate of 30 frames per second. By lowering the resolution to 1080p FPS can be raised to 60 while the 90 FPS can be reached with image resolution of 720p. Diagonal FOV is configurable to 65°, 78° and 90°. The camera is connected to the computer via USB 2.0 or USB 3.0. The maximum resolution USB 2.0 can upload is 1080p, 4K requires USB 3.0. (Logitech 2017)

Figure 24. Logitech BRIO 4K attached to the portable sensor system.

Xsens MTi-G-710 GNSS/INS, shown in Figure 25, is a high-end sensor which uses both a GNSS and an AHRS (Attitude and Heading Reference System) to provide accurate information of the system's state. Xsens MTi-G-710 GNSS/INS provides data of velocity, acceleration, rate of turn and magnetic field in 3D. Free acceleration with no gravity component is also collected. Inclination is represented with roll and pitch. Yaw represents heading and it can be set as true magnetic north-referenced or based on

gyroscope measurements. Sensor also provides data of latitude, longitude, and altitude position. (Xsens 2021b)

A GNSS antenna can be attached to the system with SMA connector to make the MTi-G-710 capable of providing position, velocity, and time data output also with GNSS receiver. However, the MTi-G-710 is primarily an orientation sensor so the positioning accuracy may not meet requirements of high accuracy applications. In Figure 25 the brass colour connector is the SMA connector. Data collected by AHRS and GNSS receiver can be combined and thus obtain more versatile information on the state of the sensor. Combining is executed onboard with a sensor fusion algorithm to maximize the performance and to minimize the drift. A strapdown integration algorithm generates orientation and velocity increments Δq and Δv. They, as well as other processed data, are uploaded with 400 Hz frequency. (Xsens 2020 p.11, Xsens 2021b)

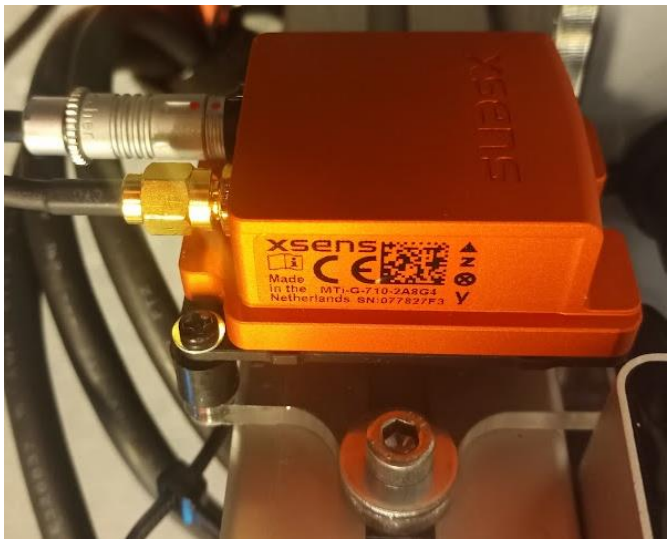

Figure 25. Xsens MTi-G-710 GNSS/INS attached to the portable sensor system with dampeners.

Gyroscopes used in MTi-G-710 can measure angular velocities in the range of 450 °/s with initial bias error of 0,2 °/s. They offer in-run bias stability of 10 °/h. Gyroscopes' noise density is 0,01 °/s/√Hz. Accelerometers standard full range is 200 m/s^2 with 0,05 m/s^2 initial bias error and in-run bias stability of 15 µg. Noise density of the accelerometers is 60 µg/√Hz. (Xsens 2020 p.37)

The Xsens' reference trajectories state position estimate's horizontal accuracy to be 1,0 m and vertical accuracy 2,0 m. Results are 1 σ values which means that approximately 68% of collected data points range within of these values. These values

are measured with Satellite Based Augmentation System (SBAS). The integrity of the vertical value is ensured with a barometer in addition to the SBAS. Reference trajectory's velocity's accuracy 0,05 m/s is 1σ value of root mean square (RMS). Autonomous GNSS position horizontal accuracy is 2,5 m CEP and with SBAS it is 2,0 m CEP. CEP means Circular Error Probable, which is the radius of a circular area which holds half of the collected data points. The mentioned performance in horizontal positioning, 1,0 m (1 σ) accuracy, is achieved with AHRS-augmentation. Tracking sensitivity is of the MTi-G-710 is -165 dBm with GPS and GLONASS. This means that tracking the satellites and gaining position fix with them is not possible if the incoming signal's power level is lower than this. Not even in warm or hot start, where the sensor has the right time or even location of the satellite. (Xsens 2020 pp.36–38)

The portable sensor system is equipped with Ouster's OS0-128 ultra-wide view high-resolution imaging LiDAR, shown in Figure 26. It is designed for both outdoor and indoor applications. With IP68 and IP69K ratings OS0 can withstand challenging weather conditions. It has a vertical resolution of 128 channel which means it uses 128 laser beams to scan the surroundings with maximum of 2 621 440 points per second. The vertical FOV is 90° which is divided evenly on both sides of the horizontal line (±45°). The vertical angular resolution is 0,7º. The horizontal resolution is configurable to 512, 1024 or 2048. The rotation rate is also configurable to either 10 Hz or 20 Hz. The OS0 has an InvenSense ICM-20948 9-axis IMU integrated to it. OS0 uses IMU's gyroscope and accelerometer data to provide samples at rate of 100 Hz. (Ouster 2021)

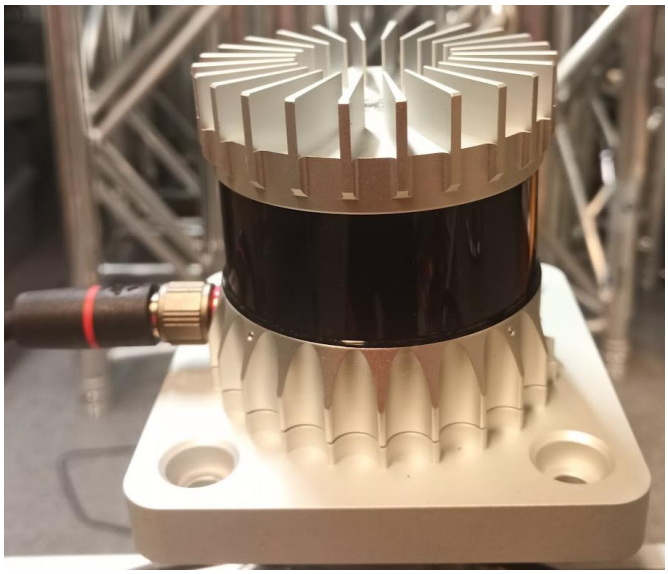

Figure 26. Ouster LiDAR OS0-128.

The maximum scanning range is 50 meters. The minimum scanning distance, for OS0 to provide point cloud data, is 0,3 meters. As mentioned in the previous chapter there are also other factors too which affect the received power. Ouster uses Lambertian reflectivity as one variable factor when describing functional range. Table 10 shows different ranges with detection probability in 100 klx sunlight using a specific operating mode. (Ouster 2021)

Table 10. Ranges in operating mode with resolution of 1024 and rotation rate of 10 Hz (Ouster 2021)

Lambertian reflectivity	Range [m]	Detection probability [%]
80%	50	>50
	45	>90
10%	20	>50
	15	>90

These sensors are controlled with the NVIDIA Jetson Xavier NX. This project uses a Developer Kit version of which dimensions are 103x90,5x34 mm. It requires a power supply which can provide 9-20 V. The Jetson is shown in Figure 27, positioned on the right side of the case. It is especially developed for system prototyping and software development. The Developer Kit has three levels of caches; a 6-core NVIDIA Carmel ARM v8.2 64-bit CPU, a 6 MB L2 and a 4 MB L3. This computer has a 384-core NVIDIA Volta GPU with 48 Tensor Cores. Jetson Xavier NX has 8 GB 128-bit LPDDR4x 51,2 GB/s memory. The microSD card is used as storage. NVIDIA Jetson Xavier NX Developer Kit has four USB 3.1 ports, one USB 2.0 Micro-B port and one port for Gigabit Ethernet. Besides that, the Developer Kit has two ports for displays: HDMI and DisplayPort. (NVIDIA 2021)

The Gigabit Ethernet port is used to connect the Ouster OS0 to the Jetson Xavier NX. The Jetson Xavier NX is mounted inside a case to the portable sensor system's frame. Connectors and wires take quite a lot of space inside the case. To reduce the number of cable glands needed for the case, an additional USB 3.0 hub with 4 ports is used outside of the case. This allows us to use a smaller case and still have enough room for the required components and wiring. Picture of the case without the cover, Figure 27, shows how little space the assembled system takes.

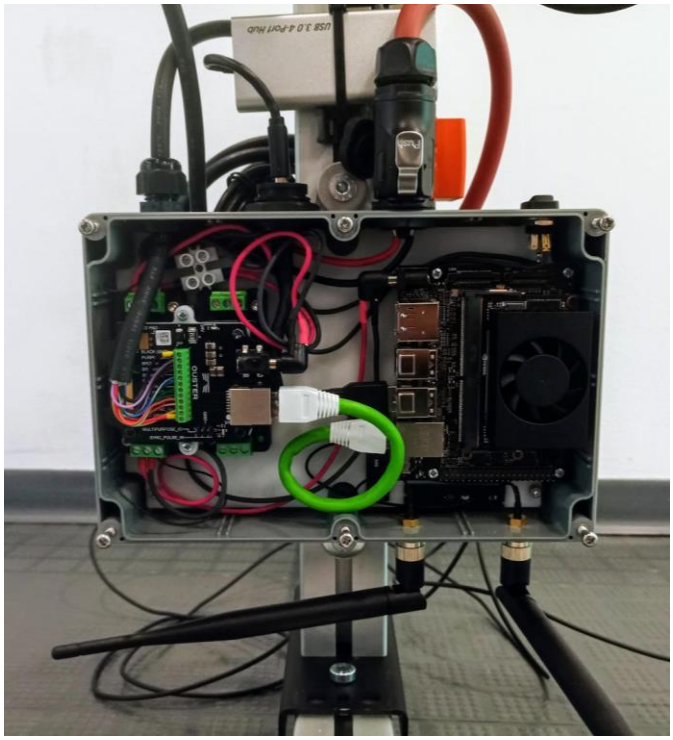

Figure 27. The assembled case without a cover.

The mounting plate for the components is made of POM (polyoxymethylene). There are two voltage regulators under the OS0's interface box, of which only one is currently used. The interface box took too much space, so it was disassembled. The casing was removed, and the remaining interface circuit board was mounted on a smaller laser-cut POM bottom plate. This bottom plate was then lifted with spacers to fit the regulators under it. Diagram of the portable sensor system is shown in Figure 28.

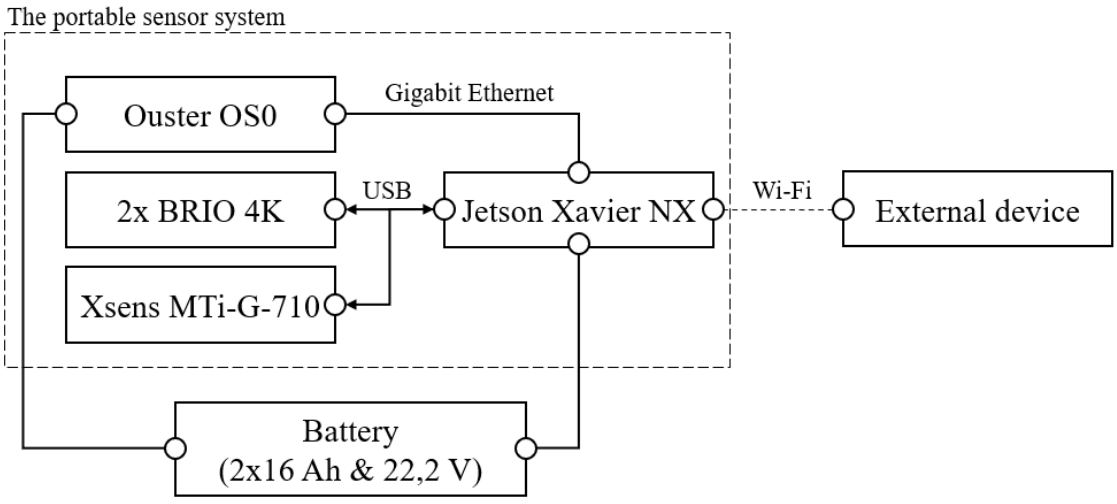

Figure 28. A schematic diagram of the portable sensor system.

A connection between the Jetson and a laptop, or some other external device for instance a phone, can be established through Wi-Fi the Jetson creates. This connection is used for example to configure the Jetson's settings and to start or stop data recording while testing. The two antennas in Figure 27 were added to the Jetson to provide more reliable Wi-Fi connection during the tests.

An overview of the portable sensor system is shown in Figure 29. In this figure there is no vertical extension piece on top. All the sensors are pictured in the place where they are typically attached. No other configurations are shown in the picture except the one which is most used in the tests. One configuration for example included an ARS 408 Continental radar in the middle of the horizontal aluminium frame to which the cameras are attached.

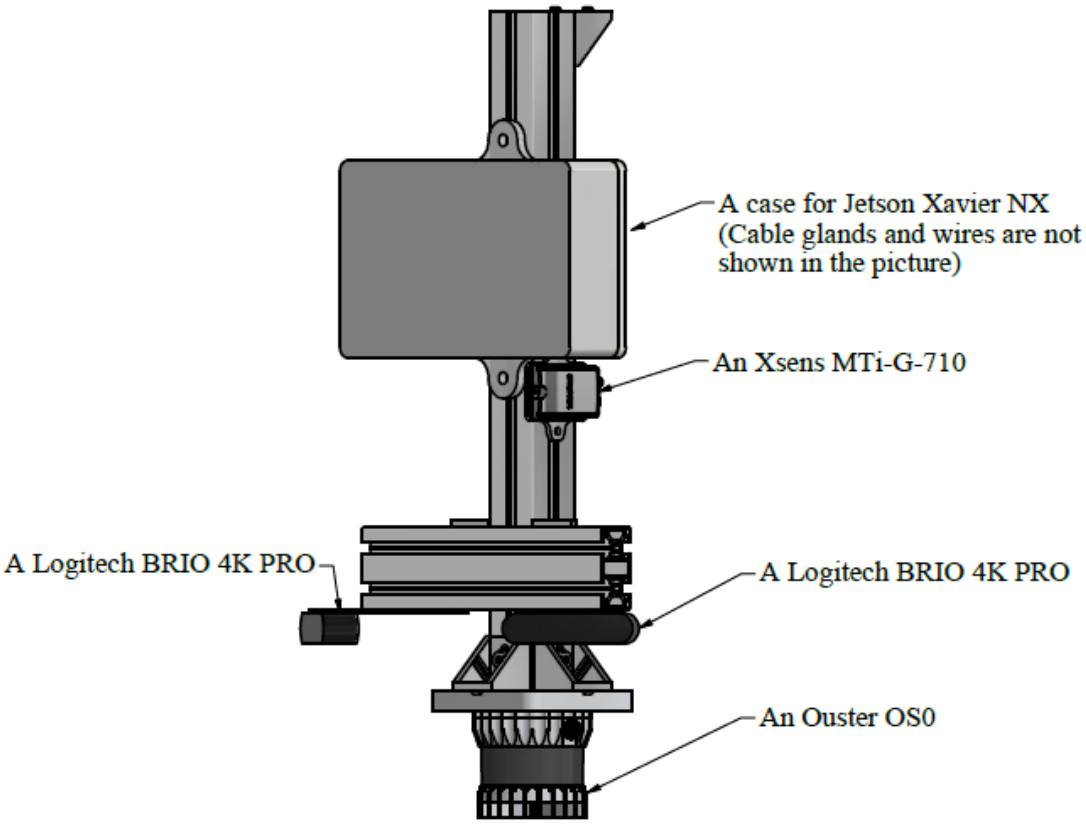

Figure 29. Overview of the portable sensor system.

5 TESTING

This chapter goes through the tests which are done to prove that the cable drone is able to fulfil the requirements set for it. Examples of the measurements which will be done with the finalized cable drone system is listed in chapter 5.1. Some of these measurements are done while testing the cable drone. Testing consists of initial testing, positioning, and automated driving tests. The cable drone, anchorages and the portable sensor system are tested in these tests.

5.1 Use of the cable drone

The cable drone is to be used in tests which aim to find out how changing environmental conditions and the movement speed of the observing sensor or camera affects acquired data. There are three main issues which can be measured.

The first issue is the accurate positioning of the drone. When its actual location is known, the data collected from the sensors attached to the drone can be compared to it. By comparing different sets of data, one collected while stationary and other from the moving drone. The result of the comparison could be used for example to produce numerical data of the error and uncertainty of the moving sensors' data.

The second issue to measure is the drone's perception. This can be done by placing objects and materials which are known to be recognizable near the cable drone's track. Then by accelerating the cable drone to the desired speed and measuring the exact distance between the drone and the recognized object at that moment of recognition the perception can be evaluated. Repeating this kind of test at different speeds gives data that can be used to evaluate the effect of speed on the drone's perception

The third issue to find out is about drone communication. This includes inspection on radio quality while using different kinds of antennas. Different technologies which are to be tested can be for example Bluetooth, UWB (Ultra-wideband) and Wi-Fi. The cable drone can be mounted with a transmitter while the receiver can be placed to one end of the track or further away. Points of interest in drone communication are factors which affect data transfer rate such as bandwidth, speed, and network latency. A Wi-Fi signal strength data logging can collect information of the dBs at a given time. Furthermore, it

can be used to track how many packages are sent and resent due to failures at given time. Implementing this on the moving cable drone could provide information on effects of the speed or movement on the communication.

Measuring these three issues must be possible with the cable drone. This means that the cable drone must move the same route several times at a constant speed while providing data of its speed and location. Data can be processed either in real time or it can be saved to the cable drone or the portable sensor system to be processed later.

5.2 Testing locations

The cable drone can be used both in- and outdoors. To capture more interesting data while doing the tests, the majority of the tests will be held outside. In order to ensure safety, the testing site should not be too crowded, especially when tests of the automatic drive will be conducted. An easy access from the university is also desirable. Outdoor testing is performed in University of Oulu, OuluZone or the Botanical Garden of the University of Oulu.

The Botanical Garden has a versatile environment that provides an excellent place for the tests. Different kinds of experiments like for example laser scanning and drone testing have been done before in the Botanical Garden. The location is optimal as it is next to the university and can be reached with a car so it will be used as the main testing place. After the cable drone is first tested in the Botanical Garden, and everything is ready it can be taken somewhere else.

OuluZone has a lot of flat terrain as well as a 5G network, so it could therefore be a good place to take measurements. A flat terrain also has its downsides. The terrain offers very little shelter, which is why the wind may become too strong for testing on windy days. OuluZone is about 40 km drive from the university. Outdoor facilities of the University of Oulu offer an urban environment for the tests if that is required.

5.3 Initial tests

During initial testing, the plan is to get acquainted with the operation and deployment of the device. The assembly process is repeated a few times in different places in order to

ensure that the process goes well and if problems occur, they can be dealt with. The need for a different way of building the track is considered. These tests will determine whether some installation operations require more people. Tightening the cables may cause problems if there are not enough people. Adjustable length of the main cable and the safety cable is made possible with four Port-A-Wraps, two ratchet cable pullers and four lifting straps and shackles.

The tests aim to find out if the cable drone is a suitable device for testing sensors. An automated driving mode will be implemented with the cable drone later. If flaws are detected in the original cable drone system, it will be modified to match its purpose. The portable sensor system is developed during these tests. In the initial tests the cable drone is operated with a T10J radio remote controller, and the cables are installed between trees.

The first test takes place in woods near the University of Oulu. This test is mostly about finding a good way to assemble the track. After testing the assembly process, the cable drone will be briefly tested. The purpose of this short test is to find out more about general behaviour of the cable drone. The goal is to find out whether the movement will cause a lot of vibrations to sensors which will be used later. This issue will be visually examined. Another factor that will be elucidated in this first experiment is the long piece induced swing. A long piece will serve as a replacement for a future portable sensor system. The long piece is made from MiniTec Framing systems' aluminium profile 45x45F. It is the same profile which is used in the portable sensor system's frame. It is first tested here without any sensors attached. If vibration and shaking significantly affect the data or otherwise interfere with sensor operation, it needs to be stabilized in the future but for now in this test it will be examined visually.

The second test takes place in the Botanical Garden where the cable drone is set between two trees in the same way as it was set in the first test. This time the distance between the trees where the cables are fastened is longer. The payload of the drone is also larger. Longer track will make the assembly more difficult so the assembly method will get tested again. The cable drone will be equipped with a portable sensor system which includes a computer, two cameras, a LiDAR sensor, and a radar.

The purpose of the second test is to determine whether the portable sensor system requires additional equipment to function properly with a stationary computer while

attached to the moving cable drone. With changed payload and longer distance, behaviour of the cable drone needs to be tried out before making longer tests. Communication with a stationary laptop and the portable sensor system is tested by sending commands to the sensor system while monitoring connection between them. These will also be assessed in future tests.

The third test is about trying how Xsens MTi-G-710 GNSS/INS works as part of the portable sensor system. The goal is to establish a connection between satellites and the GNSS/INS sensor. Then the velocity and the position of the cable drone will be measured with this sensor. Because no large problems were noticed while assembling tracks in earlier tests, the testing site is going to be moved to a more remote location. Installing the cables somewhere where they can be left in place for a longer period of time will accelerate the progress of the project. The general behaviour of the cable drone is examined throughout the tests to ensure safe testing and operation.

The deployment of the MTi-G-710 on the drone continues in the fourth test session. The cables are already fastened which makes it faster to conduct the tests. In addition to testing functionality of the entire system, the main points of interest now are to establish a connection between the MTi-G-710 and the satellites, gather data from three runs at different speeds and visually follow up the wearing of the rubber ring. The tests are simultaneously trying to establish a more reliable remote connection between a stationary laptop and the Jetson Xavier on the cable drone.

The data will be collected while driving at three different velocities from one end to another and back. The acceleration and velocity data from these runs will be visualized in graphs to show how the manually controlled cable drone behaves. Satellite C/N_0 represents carrier-to-noise density ratio. In other words, this means the signal strength unit is dBHz. Satellite C/N_0 will be plotted into the same graph to analyze the reliability of data. The higher the measured C/N_0 is, the less noise there is on the measured speed and acceleration data.

The usable portion of the track is approximately 80 meters long. This also counts appropriate braking distances at the ends. First, data will be collected as the cable drone drives as fast as possible. The first-round of these tests whether the drone reaches constant speed when controlled to travel at maximum speed. The second run will be done at a little bit slower speed and the third run is the slowest run of this test set.

Besides collecting data with MTi-G-710 these test runs also test the general behaviour of the cable drone when it is controlled manually.

This time testing includes setting up also a Wiral LITE Cable Cam alongside our cable drone. An Insta360 one X camera is attached to the Wiral. With this setup, a video will be shot of the cable drone as it is driven. The same Insta360 one X camera will also be attached later to the cable drone for extra video footage. The video is to be shown at a project meeting.

5.4 Positioning

Positioning is one of the most important factors of this system. The main purpose of these tests is to find a reliable way to track the cable drone's location so that the control of the automated driving can later be implemented by depending on this information. The accuracy of the position estimation is also important for the portable sensor system. The position estimates for the portable sensor system do not necessarily have to be from the same source as the position estimates which are used to control the cable drone.

The wheel odometry's suitability for this application will be tested first. Roboteq MDC1460 motor controller can use an encoder to track the rotation and the angular velocity of the motor. This feedback can be used to achieve precise speed and position control. This method would be a logical choice because the cable drone is already equipped with an encoder. Testing and evaluation of this method is carried out simultaneously with the initial tests of the cable drone and the portable sensor system.

This is a relative positioning method and thus the position's accuracy will be evaluated by examining endpoints. The tests are done by placing endpoints for the cable drone. Here the endpoints are the encoder's values at the given position. The encoder's value is tracked with the motor controller, and the movement is allowed only between these two endpoints. If the encoder's count reaches the endpoint's value, the motor will halt. The cable drone can then move only to the direction that takes the value towards the allowed interval. The rotation of the motor in the other direction is prevented until the cable drone is again between the endpoints.

The second possible choice is to use the GNSS based positioning method. With an appropriate antenna and a tracker, the movement of the drone could be traceable. The Xsens MTi-G-710 is used as an external GNSS/INS sensor, measuring velocity and acceleration. Testing and evaluation of this sensor begins at the end of initial tests, after the portable sensor system is first tried out and tested on the cable drone. The suitability of this method for positioning is examined by plotting location data into a map. The sensor calculates position data with sensor a fusion algorithm. This data is plotted into Google Earth for further analysis. The data is given as latitude and longitude in the WGS84 datum so plotting will not cause problems. Carrier-to-noise density ratio will be considered when evaluating the accuracy of measurements. The higher the measured C/N_0 is, the less noise there is on the measured position data.

The third method to be tested is RTK GNSS positioning with a u-blox C94-M8P. RTK GNSS would offer very accurate position estimates for the cable drone. This method shall be tested first without the cable drone in order to find out whether the RTK fix is possible and if the accuracy of the base station is adequate. The only u-blox C94-M8P available for these tests is known to have potential malfunctions, so if its implementation produces difficulties, then it will be left to be resolved later. The rover can be attached to the cable drone and the stationary base station to one end of the cables.

The fourth method differs from the two earlier methods as it does not rely entirely on a strong satellite connection. The suitability of VSLAM based Intel RealSense Tracking Camera T265 for positioning method is tested. Testing and evaluation of this method is carried out first in this section and later while testing the automated driving sequence. These tests will examine the functionalities of the T265. The first goal with the camera is to obtain usable data of the moved distance in real time. This data must be available for use all the time when the camera is connected to a computer. After this, the data must be connected to the motor controller. The motor controller needs to notice the changes in position quickly.

Tests are done in a similar manner to the encoder-based wheel odometry. Endpoints will be placed for the cable drone. The T265's lens is parallel to the T26's pose's Z direction. Endpoints are T265's values for position in Z direction in a certain location. Therefore, the value of the camera's position estimate along Z direction is tracked. This

method is attempted because the cable drone's movement is also 1-dimensinal so tracking a single direction will most likely be enough. The endpoints delineate the area where movement is permitted. If either one of the endpoint values is exceeded, the cable drone's movement will be restricted. Then it can only move to the direction which takes the T265's position's value towards the allowed interval. This resembles the operating principle of automatic driving but on a smaller scale.

The T265's tracking method is a relative positioning method and thus the position's accuracy will be examined with endpoints. The motor is controlled in the same way it would be controlled in the automated driving sequence. The camera resets its location when it is switched on. The following driving sequence needs to be achieved with a python script. The python script creates two endpoints point A and point B. Point A is located 20 cm in front of the camera's lens and point B 20 cm behind the camera's lens. Initially, the motor controller gives a command to drive forward until the camera reaches its pre-set point A. When the camera reaches this point, the motor stops. If, for any reason, the camera moves backwards and ends up to the wrong side of point A, the motor starts to spin forwards again until the camera reaches point A. This continues until the python script gives it command "backwards". Then the motor starts to run backwards until the camera reaches the point B and the motor stops. If, for any reason, the camera ends up on the wrong side of point B, the engine starts to spin backwards again until the camera reaches point B. This is a sufficiently accurate method to begin the tests with the T265. This type of an operating principle is needed later in an automated driving sequence. Therefore this type of functionality must be tested with the T265.

5.5 Automated drive

The primary goal of these tests is to find a way to automatize the cable drone's movement. The movement is limited between two points with the same method which was used in the earlier positioning test with T265 camera. This time the points are set further apart to test this method on a larger scale. The position of these endpoints must now be set remotely. The cable drone is supposed to move without operator influence. However, this is not fully implemented in these tests, as the operator still needs to press the enabling switch to ensure the safety of the tests. This will make the tests safer without the need for limit switches on the cable or proximity sensors.

The position of the cable drone is tracked as it moves along the cables with two methods. Tracking which controls the motor controller is done by an on-board T265 tracking camera. In addition, the position is tracked also with Xsens MTi-G-710 so that the cable drone's location can be visualized in Google Earth and the tracks can be analyzed later. The automation of the driving sequence is done with a python script which uses commands from a library with all the needed MicroBasic commands. Jetson TX2 runs this python script which controls both the motor controller and the tracking camera.

Testing automated drive with a motor controller in Open Loop Speed -mode. As mentioned earlier in chapter 3.3, here the Go to Speed -commands given for the controller sets the desired power which is applied to the motor. Testing includes the endpoint setting, dead man's switch test and driving in roundtrip mode with different power outputs. These tests try out automated driving mode so it can be decided if it needs to be improved. Necessity of Closed Loop Speed -mode will be tested. Tests are to find out how well configuring driving settings remotely works.

The motor's acceleration is set to 3000 rpm/s and deceleration to 3500 rpm/s. The desired power will be increased from 20 per cent to 50 per cent of the maximum power. Between the rounds, the power output is increased by ten percentage points. Similar to the manual test runs; in addition to position information, also data of acceleration, velocity and satellite signal's strength will be collected from each of these rounds. The data from these four test rounds will then be shown in graphs for further analysis.

6 RESULTS AND DISCUSSION

This chapter goes through the results of the tests and shows how the planned tests were carried out. During the tests different aspects will be evaluated. The pictures of different testing setups are also provided. Later the results are shown in graphs with acceleration and velocity plotted as a function of time. The same kind of graphs are presented for both manual and automated drive. Further studies compiled from this project are listed at the end as a guideline for future research. They contain some of the things that have come up when doing this work but cannot fit into this master's thesis and serve as examples of what to do next.

6.1 Initial tests

In the first test the equipment was tried out and assembling the cable system was practiced for the first time. The used setup of the cable drone is shown in Figure 30. Both the main and the safety cables had to be able to be left in place while the cable drone was taken off. First the cables were laid straight between the trees and Port-A-Wraps were attached to them. Then lifting straps were tied to the trees. Port-A-Wraps were joined directly to the lifting straps on one tree by shackles. On the other tree ratchet cable pullers were put between the lifting straps and the cables. Both cables were slightly tensioned before attaching the drone. The cables were tightened simultaneously when the cable drone was securely on the cables. This assembly method worked out well at the woods nearby University of Oulu where the track's length was short. A short track made the assembling easier. The safety cable wheel was attached to the cable drone with a nyloc nut, which was later switched to a wing nut to speed up assembly.

With no cameras or sensors attached the system seems to be quite stable. The testing period was short and further experiments are needed to ensure that the movement is sufficiently smooth. Visually, the swinging did not appear to be so strong as to substantially impede the performance of the tests. MiniTec Framing Systems' aluminium profile 45x45F seemed to be a little oversized for this application at first. When the applications for the portable sensor system were roughly outlined, requirements for it could be placed for it as well. Weight is not the only significant factor in the system. The cable drone, as well as other equipment such as the LiDAR sensor, causes some vibrations to the portable sensor system. Additional corner piece

and wider mounting surface between the cable drone and the portable sensor system helps to reduce these vibrations.

Figure 30. Assembly of the device used in the first test.

Second test took place in the Botanical Garden. Although the longer track caused the cables to sag more than in the first test, the cables could be tightened sufficiently enough for these tests to be performed properly. Adequate initial tightening of the cables reduces their sagging after their final assembly. Lifting straps must be tightened securely around the trees to prevent them from slipping during the assembly. Due to the long distance between the anchorages, it takes a significantly longer time to secure the cables than desired. The process also required quite a lot of people, especially in the initial tightening of the cables. Figure 31 shows assembly of the device used in the second test.

The communication between the portable sensor system and the laptop was carried out with Wi-Fi. The communication between the devices appeared to be unreliable and therefore an extra antenna needs to be added to the sensor system to see if it will fix the problem. Placement of the antenna depends on what causes interruptions. As there were no connection problems when the sensor system was tested on the ground, pointing the antenna away from the cable drone might be a good place to start.

Figure 31. Assembly of the device used in the second test.

Testing setup on the third test was the same as in the second test except for the Continental radar ARS 408 which was removed and the Xsens MTi-G-710. After rigging the cables again between trees, the third test session was ready to begin. Not long after the start, it was noticed that the wheelspin had increased considerably. The rubber O-ring on the wheel was worn out which led the wheel to lose traction to the cable. Because of this, the tests were stopped, and the cable drone was overhauled.

Testing the MTi-G-710 GNSS/INS was cut short, and not enough data was collected to draw conclusions. Somewhat alarming is that Xsens appeared not to get GPS signal at all, because velocity data was not gathered. However, the testing location itself was good, and a permission was granted from the Botanical Garden staff to leave the cables in place for further testing. After replacing the worn-out rubber ring with a new one, implementation of the MTi-G-710 on the sensor system continues.

The fourth test succeeded in establishing a link between Xsens MTI-G-710 and satellites, so that GNSS-based location and speed information was received. The position of the antenna was corrected, and a sheet of metal was placed under it to

amplify the signal. The antenna was placed on a flat surface in such a way that there was nothing above it that would disturb the connection. Dampers were also added between the body of the sensor system and the Xsens MTI-G-710. Setup of the fourth test is shown in Figure 32. The Wi-Fi connection between a stationary laptop and the Jetson Xavier is still quite weak. After this test session, larger antennas are added to the portable sensor system to improve the quality of remote connection.

The rubber ring on the wheel wears out noticeably fast. This means that automated drive cannot rely purely on the assumption that the encoder's data would be accurate enough for positioning. Because the wheelspin increases considerably, especially when accelerating with a worn-out rubber ring, the encoder could potentially be used to monitor wearing of the O-ring. Multiple kinds of O-rings differing in hardness and material were ordered to find out which ones will endure this kind of usage the best.

Figure 32. Testing and filming setup including the cable drone and a Wiral LITE.

Figure 33. Installation of the cables between trees.

Throughout the initial tests the anchoring method shown in Figure 33 was used. Installation of the cables and assembling the system seemed to work as expected. Installation requires trees at appropriate distance from each other. This will become a problem in rough terrain where there are no trees or on the other hand if there are too many trees the distance between them might be too short. Thus, in order to broaden the testing site options, it was decided to design a truss tower structure that can support the cables. More of this new anchoring method can be found in chapter 3.4. (Anchorage).

When performing test runs at different speeds, neither speed nor power was limited to certain values. The speed was manually controlled by a radio controller. The accelerations and velocities achieved in the tests can be read from the graphs in Figure 34, Figure 35 and Figure 36. Velocities and accelerations are presented as positive values. Acceleration, satellite C/N_0 and velocity data are obtained by the Xsens MTI-G-710 GNSS/INS sensor. Length of the run was approximately 60 meters. In Figure 37 the longest (black) track is 84 meters. 10 meters safety distance at the ends of the track was used in manual runs for safe breaking. This figure is presented in chapter 3.6 (positioning) where positioning methods are evaluated.

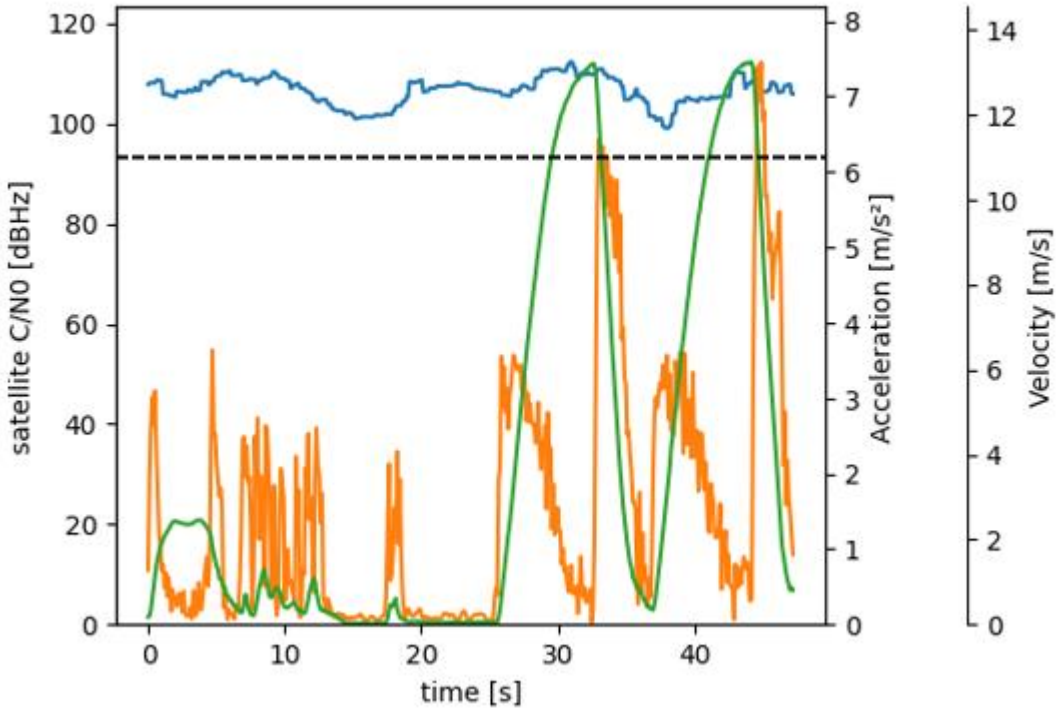

Figure 34. Acceleration (orange), velocity (green), satellite C/N_0 (blue) data from the first test round.

Figure 34 shows that the drone did not reach a constant speed within these runs. The first 25 seconds of the data is not relevant as it is recorded while the starting position for the run is still being adjusted. Satellite C/N_0 varies from 100 dBHz to 110 dBHz which means that the signal is strong, thus the measurements are accurate. The acceleration is presented with an orange curve, and it peaks at 3,5 m/s^2. It is a decent acceleration for the cable drone. The deceleration peaks at around 7 m/s^2. In the second run the deceleration peak is a little bit higher. It is possible that the cable drone's wheel would have a better grip at the other end of the cable. One of the system requirements was that the cable drone would have to move without a heavy payload at 11 m/s speed. The aimed speed is highlighted in Figure 34 with a black dashed line. The maximum velocity the cable drone reached was 13 m/s. This can also be considered as a good result for the drone with a 5,5 kg payload. In this test the speed requirement was fulfilled. In this round plotted data operator's effect is not visible because the run was done in full throttle.

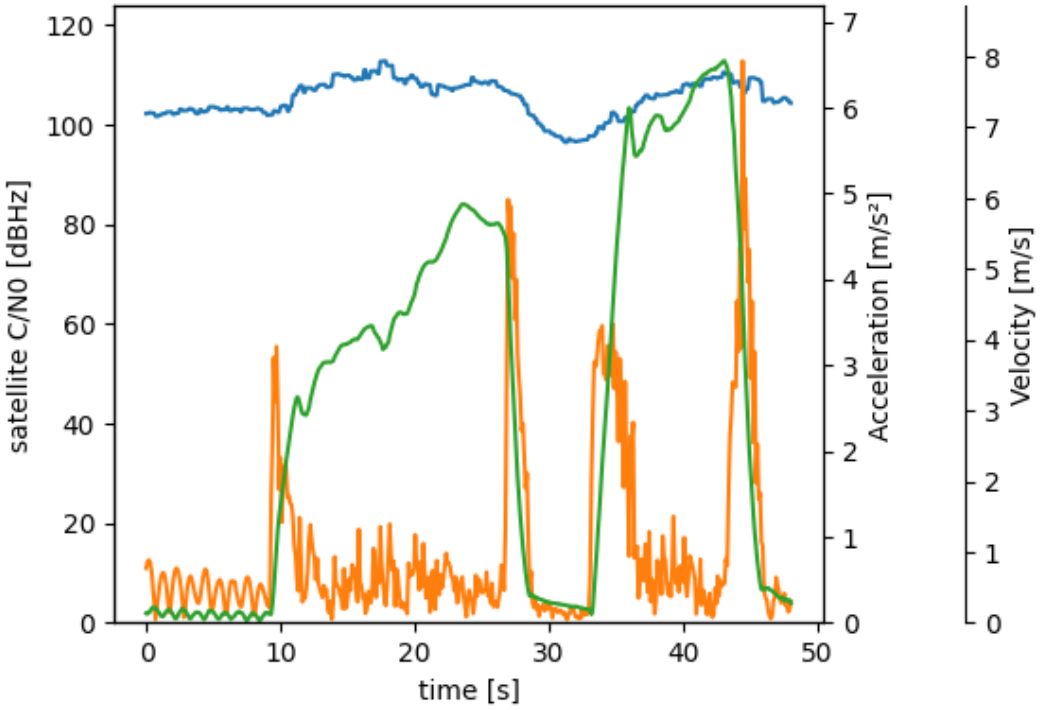

Figure 35. Acceleration (orange), velocity (green), satellite C/N_0 (blue) data from the second test round.

Figure 35 shows the data from the second test round where the cable drone was manually driven with slower speed. The drone would have reached a constant speed within these runs. Constantly increasing velocity was caused by the operator's finger's misplacement. This led the control switch to move slightly upwards and thus increasing the velocity. This is why the velocity is not constant in the first run. The second run is done in the other direction. In the second run average velocity was 7 m/s. The operator's effect can be reduced in automated drive where the speed or power is limited by a code. The acceleration peaks at 3 m/s^2 in both runs. Similar to the first round; even though the deceleration of the motor remains the same, the deceleration in the graph is larger in the second run than it is in the first run. This might be because the velocity was also larger, and the wheel could have had a better grip at the other end of the cable. This would lead to shorter braking distance and greater peak acceleration in the graph. In the first run the deceleration's maximum value is 5 m/s^2 and in the second run it is 6,5 m/s^2. Carrier-to-noise density ratio is high, so the measurements are accurate.

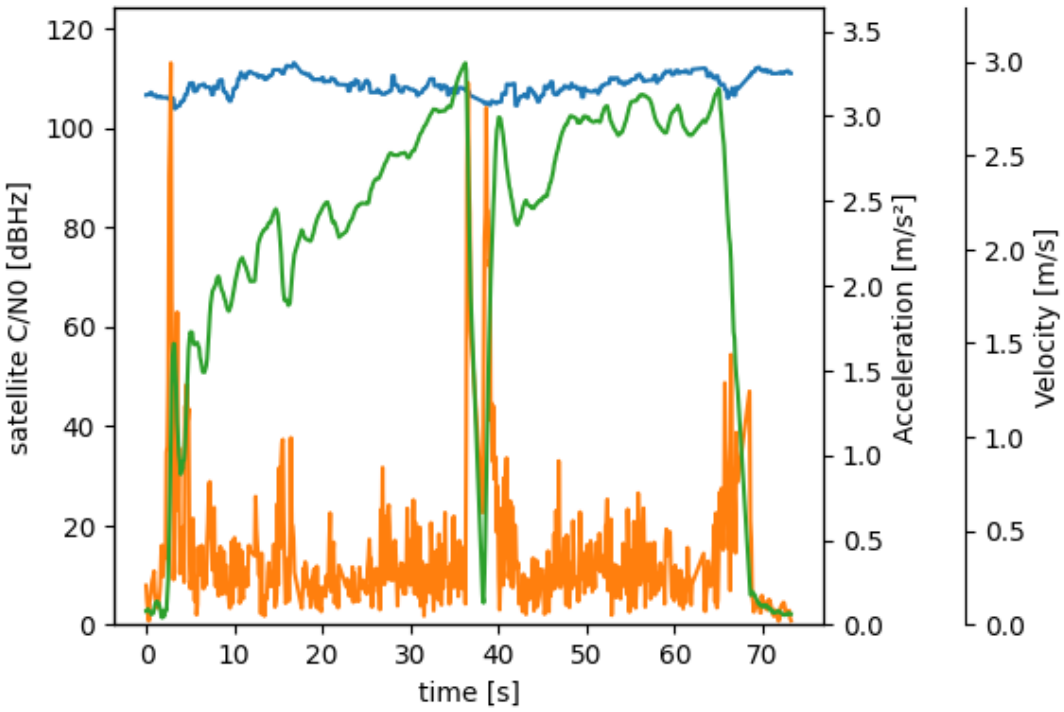

Figure 36. Acceleration (orange), velocity (green), satellite C/N_0 (blue) data from the third test round.

Figure 36 shows data from the slowest run. The drone reached a constant speed within these runs. Constantly increasing velocity on the first run is due to the same reason as in the previous runs at medium speed. It is relatively hard to achieve constant speed with the cable drone if the speed is not limited. The average velocity the cable drone reached in the second run to the other direction was 2,5 m/s. The acceleration peaks at 3 m/s^2 in both runs but they decrease rapidly after the start. The operator's effect can be reduced in automated drive where the speed or power is limited. High frequency variation in the acceleration graph is caused partly from shaking and vibrations. This can be seen in all three test rounds, but it increases in the last round. Increased vibration may be due to O-ring wear. In Figure 34, Figure 35 and Figure 36 can be seen that the high frequency variation in acceleration graph diminishes when the cable drone is stationary. This supports the idea that this variation would be due to vibration. The satellite signal was strong, over 100 dBHz, so these measurements can be considered accurate.

6.2 Positioning

Wheel odometry cannot be used as a primary positioning method for this application. The encoder keeps up with the rotation of the motor, but it is not enough because it does

not correspond with the linear motion of the cable drone. Slipping or sliding of the wheel on the cable cannot be fully controlled without considerably reducing the acceleration. Even if the acceleration is reduced, it is not certain that the wheel slipping would not occur when the weather conditions are not optimal, and the rubber ring wears out.

An excessive wheel rotation makes the position estimates quickly drift from the actual position. This will eventually lead into shifting the allowable interval from its original location and eventually the cable drone will crash. The endpoints have to be reset often to keep the cable drone at a safe distance from the track's ends. If the wheel slipping could be prevented the wheel odometry would probably be an accurate enough method for positioning in the automated driving mode. After all the movement is one dimensional and it could not drift in other directions. One way to fix this problem would be to add another encoder to a non-pulling wheel. This would not consider the wheel slipping at the beginning of the acceleration as the actual movement which seems to be the biggest problem in this method.

Problems were encountered with the satellite connection during tests with Xsens MTi-G-710. At first the satellite connection appeared to be too weak for Xsens to provide position estimates. As mentioned earlier a sheet of metal was added under the antenna to improve the signal. Furthermore, the antenna was relocated to the top of the battery case to remove disturbances caused by objects above it. With these corrections the connection to the satellites was established. The accuracy of position provided by the MTi-G-710 is stated to be around 1 meter.

The position data was gathered during the initial tests and later during the automated test runs. The position data used in Figure 37 were gathered from the initial test's manual runs. The sensor gives position data output as latitude and longitude in the WGS84 datum. The data of these runs were saved as KML files. KML files were then plotted directly into Google Earth to visualize the results. Figure 37 shows that the sensor's estimates of the tracks overlap each other. As the cables stayed in the same place this is a good result. As mentioned earlier, the satellite C/N_0 was between 100 dBHz and 110 dBHz which means that the measurements are accurate. The cable drone's location can be followed with this method quite accurately and the 1 meter accuracy of the MTi-G-710 seems to be achievable.

Figure 37. Position data from initial tests' first (black), second (red), and third (white) manual test run collected with Xsens and plotted into Google Earth while yellow line represents the cable.

In Figure 38 the position data were gathered from automated test runs. There the movement was already controlled with position information from T265. The plotted position estimates are from Xsens MTi-G-710. Even though the cables stayed in the same place the measured tracks are not overlapping in Figure 38 as they do in Figure 37. This means that the tracks in Figure 38 are not as accurate as in manual runs. The sensor was moving for most of the time which can affect the accuracy. The position estimates may deteriorate if the number of satellites drops, and the sensor loses its place. Then as the sensor is on the move, it is harder to get accurate estimates.

Also, the carrier-to-noise density ratio was smaller in automated runs than in manual runs so the accuracy may have deteriorated because of the noise. There is more noise in the data which leads into less accurate position estimates. In the automated test runs the satellite C/N_0 was approximately 80 dBHz. The Xsens found less satellites during the manual test runs, but the C/N_0 is larger. Carrier-to-noise density ratio could be increased by removing possible causes of interference. A more reliable solution is needed for automated drive as the problems with the satellite connection may unexpectedly return. The Xsens MTi-G-710 works well for the portable sensor system.

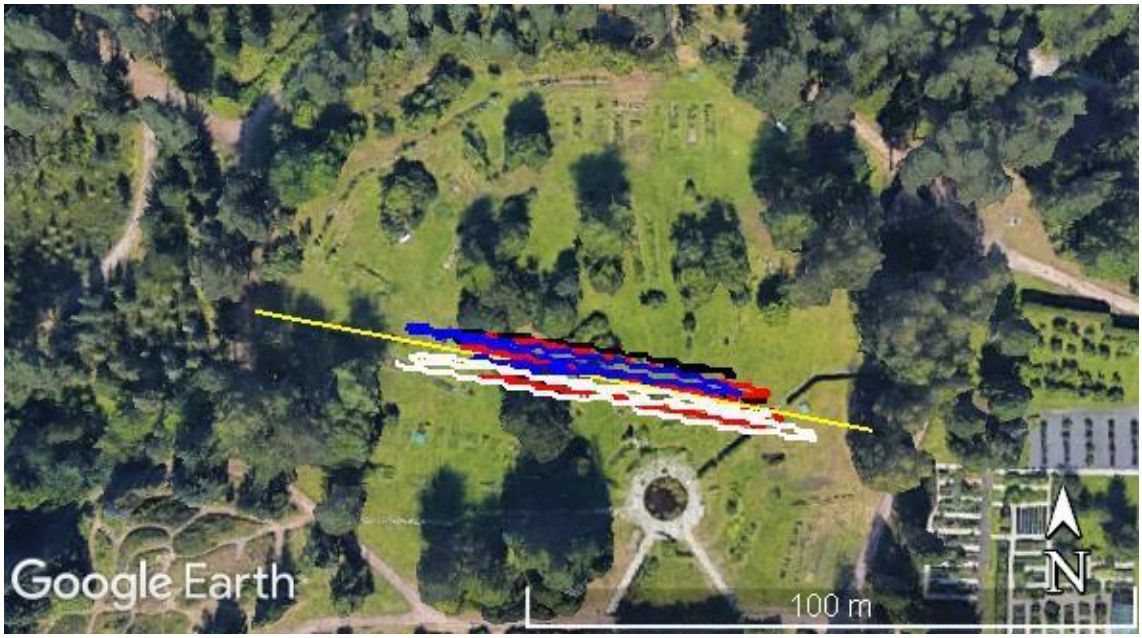

Figure 38. Position data from automated runs with 20% power (white), 30% power (red), 40% power (blue) and 50% power (black) measured with Xsens and plotted into Google Earth while yellow line represents the cable.

The testing period with the u-blox fell short because the testing environment for GNSS-based positioning is relatively challenging at the University of Oulu. Tall buildings block and reflect the signal quite effectively, making quick testing much more difficult. RTK fix was momentarily established between the base and the rover. The accuracy of the rover's position estimate was not sufficient due to the stationary base receiver's poor position estimate's accuracy. Problems in accuracy were caused, at least to some extent, by the reflected signals. It should be given more time for the RTK fix to be established and for the stationary base receiver to find its correct location. However, if the incoming signal is reflected, it will lead into incorrect calculations on the position estimation process. This method needs more time to work, and the condition of the u-blox C94-M8P needs to be checked.

The position estimation with a tracking camera T265 was successful. The location information from the tracking camera was obtained quickly with a Jetson TX2 computer running a python script which polls this information. The T265 gives position estimates in relation to its original location. Both the camera and the motor controller are connected to Jetson TX2 via USB. The communication between the camera and the motor controller is tested by using another python script, which connects the T265 position information to the motor controller. The python script orders the motor

controller to send a command to drive the motor forwards and backwards depending on where the camera is located.

Driving sequence which makes the motor drive automatically from one endpoint to another was achieved. The tracking camera notices changes in its position quickly. If the motor controller was giving a command to drive forwards and the camera was in between the endpoints, the motor kept running forwards. As soon as the camera was moved to the endpoint A the motor stopped. The accuracy was approximately 1 cm. Then the controller's command was changed to "backwards" and the motor started to run backwards. It stopped only when the camera had reached the endpoint B. The accuracy was still approximately 1 cm. This was repeated multiple times and the accuracy remained the same. When the relocalization feature was disabled, the camera quickly lost its position if movement was quick or otherwise unpredictable. The relocalization feature needs to be enabled so that the camera can correct its position if it notices drifting. Similar driving sequence could possibly be done on a larger scale for the cable drone when the driving is going to be automated.

With this test layout the accuracy was centimeter-level, which is very good result for this application. It is important to remember that the distances were small, the camera was used indoors, and the camera had many features around it which it could track. The motor controller's response time when the position estimates reach the endpoint was very short; command which halts the motor was sent almost instantaneously. The automated driving sequence will be implemented on the cable drone with this method. The T265 camera is stated to have 1 per cent error. It means that for example after moving a 150 meter long route, the camera's location estimates may be expected to be 1,5 meters off. The accuracy may be impaired when the device is used outdoors. This should be considered when the automated driving modes endpoints are defined later.

6.3 Automated drive

The communication between the T265 and the motor controller was working well in the test script in positioning tests, thus a similar python script was made which also includes a socket server. The Jetson TX2 runs the code which has a socket-client connection to another computer via Wi-Fi hotspot the TX2 makes. This communication method worked reliably and will most likely be used also in the final version.

This Wi-Fi communication method via the socket server made it possible to configure settings remotely. This way the values of for example acceleration, deceleration, and desired power can be changed while the cable drone is on the cables. The code is also used to switch between the manual and the automated drive modes. Endpoints of the automated drive can be set remotely by driving the cable drone to the desired position in manual mode and sending a command “positionA” and then proceeding to the other end and sending a command “positionB”. Configuring settings is rather quick via the socket server.

Some modifications were made to the positioning test’s script besides the socket server. For example, one additional automated driving mode was added and an ability to remotely change between these modes. When the endpoints are set the driving mode can be changed from manual to automated. The two different modes for automated driving are “single” and “roundtrip”. The drive mode called “single” makes the cable drone to drive to one endpoint, just like in positioning tests with T265. Direction can then be changed by sending commands ”backwards” or “forwards”. The mode called “roundtrip” causes the cable drone to drive between the endpoints for as long as the enabling switch is pressed. This mode makes testing faster and more automated.

The single -mode was briefly tested and it worked as expected. Endpoints set with the T265 camera were first tested with this mode before changing the mode. Just like in positioning tests, the motor controller’s response time when the cable drone reached an endpoint was fast. The command which halts the motor was sent almost instantaneously and the cable drone stopped near the endpoint. The cable drone moved a little bit beyond the endpoint, which was expected due to braking time. This crossing distance increased as the velocity was increased. Drifting of the endpoints’ locations and length of the braking distance was visually examined by following the cable drone’s movement and behaviour.

The roundtrip -mode was used later when the test runs presented were conducted. In the same way as in the single -mode test, this method was also visually examined. In addition to the visual examination, the commands which the motor controller sent to the motor was also followed from the screen by polling it with the code. Location of the cable drone was followed in a similar way. According to the T265’s position information the places where the cable drone changes direction did not drift or move

significantly. The variation remained well below one metre. This mode worked well, but the cable drone needs more time to stop completely before starting to accelerate in another direction. Now it can be seen in the velocity graphs in Figure 39, Figure 40, Figure 41, and Figure 42 that the velocity starts to increase immediately after the cable drone has stopped. It was also visible while conducting the tests that the acceleration had already started before the cable drone had stopped. This is very consuming for the O-ring and must be corrected.

The realized tracks measured by Xsens MTi-G-710 are shown in Figure 38 which is presented earlier in the previous chapter. From the plotted tracks it can be seen that the T265 did not lose its position during these tests in such a manner that the cable drone's track would have shifted or stretched considerably. The T265's position estimates seem to be around the stated 1 per cent error on a larger scale. This accuracy may be impaired if visibility gets worse for example in bad weather. With appropriate safety distance considered at the ends of the track, and the T265's relocalization feature enabled, this method should be accurate enough for automated driving.

To test and demonstrate how the automated drive works, the cable drone was driven with four different power outputs. This demonstration was done in Open Loop Speed -mode because of the mentioned problems with Closed Loop Speed -mode. At first the cable drone was programmed to drive with 20% of the maximum power. Between different parts of the test, the power was always increased by 10 percentage points. The accelerations and velocities achieved in the tests can be read from the graphs in Figure 39, Figure 40, Figure 41, and Figure 42. The acceleration and velocity data as well as the signal strength and the position estimates are obtained by the Xsens MTI-G-710 GNSS/INS sensor.

These tests do not use trees to anchor the cables but utilize truss towers instead. Distance between the towers is approximately 100 meters. When endpoints were defined for automated driving sequence, the towers were left with a safety distance from these endpoints. As this was the first time the automated driving sequence was tested, the safety distance may have been even too large. This shortens the track quite considerably.

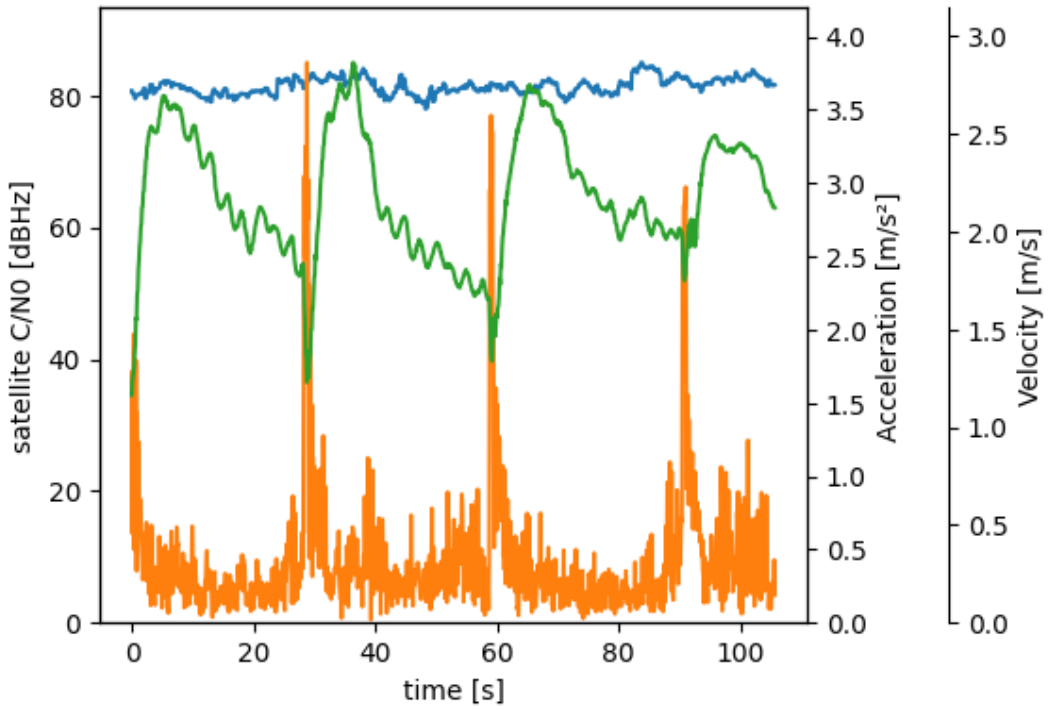

Figure 39. Acceleration (orange), velocity (green), satellite C/N_0 (blue) data when driving at 20% of maximum power.

Figure 39 shows how the acceleration peaks in the beginning and in the end of each run and stabilizes quickly when the power output is reached. The acceleration peaks briefly at 1,5 m/s^2 and the deceleration peaks are about at 3,5 m/s^2. There is noise-like variation in the acceleration graph which can be the result of shaking and vibrations or possibly the GNSS data's accuracy. Satellite C/N_0 is around 80 dBHz which is smaller than in manual runs in the initial tests. Some of the variation is due to poor and unstable traction on the wheel which will cause vibrations. According to the speed curve the velocity decreases from 2,75 m/s to 2 m/s during the runs, even though the output power remains the same. This is caused by relatively small power as the cumulative effect of air resistance, cable drone's payload, form of the cable and effect of wheel spin is quite large. These factors will cause problems in Open Loop Speed -mode. This run was also the first time the cable drone's location was controlled with the position data from the T265 tracking camera and it did not produce any significant problems.

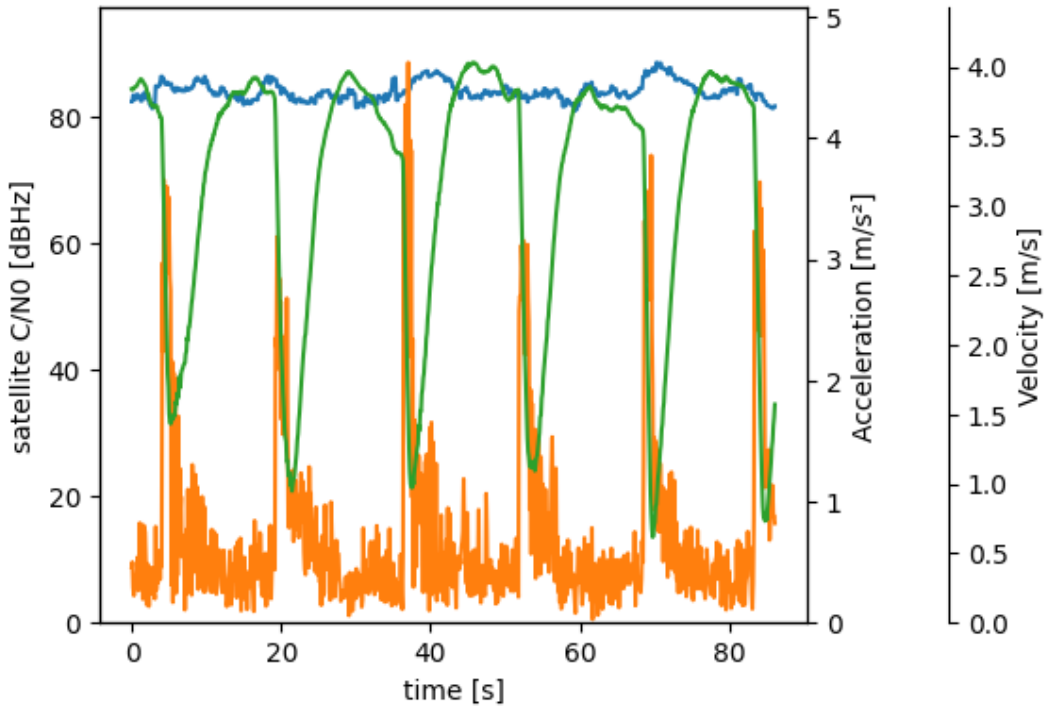

Figure 40. Acceleration (orange), velocity (green), satellite C/N_0 (blue) data when driving at 30% of maximum power.

The deceleration peaks are higher in Figure 40 than in Figure 39. The acceleration peaks are about at 1,5 m/s^2 thus they are the same height as in Figure 39 but wider, so the acceleration takes more time. The reason for this can be that the power was increased but the acceleration remained the same. This time the velocity stabilizes as the cable drone reaches the speed 3,9 m/s. These results are quite good. Other test rounds aim for similar results such as in this round, where the top speed is achieved relatively quickly, and the speed does not vary during the run. There are still some variations between the runs, thus it needs to be examined in more detail which causes them. The direction of the run seems to influence the maximum velocity. The cables' form can result in this kind of phenomenon. The Closed Loop Speed -mode would neutralize these kinds of errors. The cable drone seemed to keep its location quite well within permissible limits with the points it has been given. The carrier-to-noise density ratio is still around 80 dBHz so accuracy is at the same level as in the previous test.

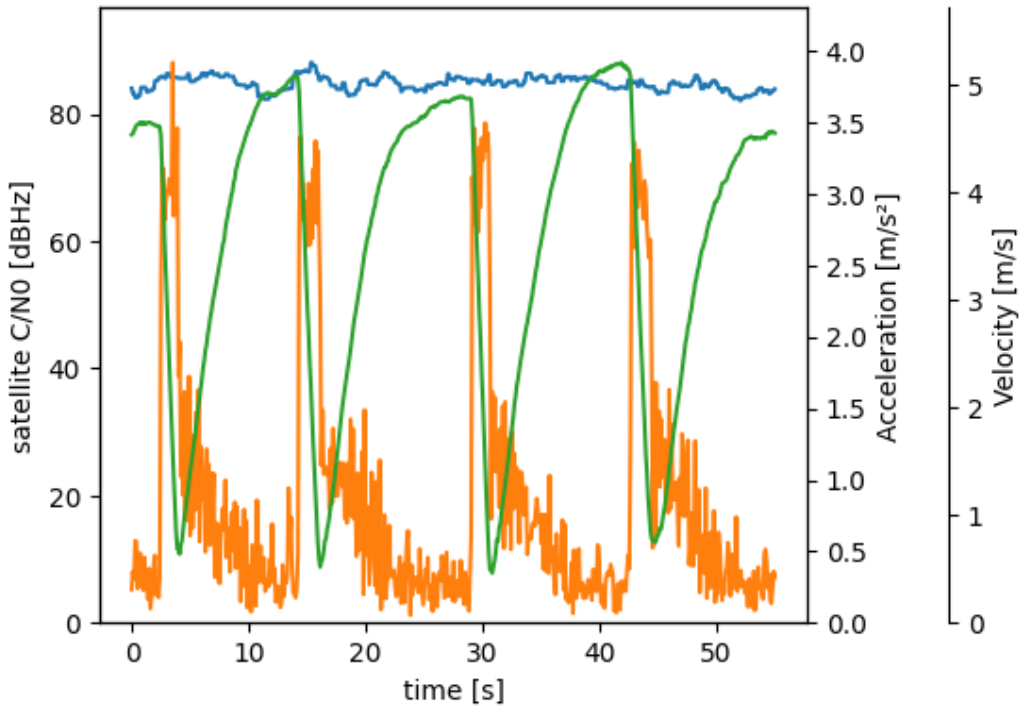

Figure 41. Acceleration (orange), velocity (green), satellite C/N_0 (blue) data when driving at 40% of maximum power.

The velocity graph in Figure 41 shows a similar problem to the one in the fastest manual run in Figure 34. The cable drone is almost not able to reach constant speed. The maximum acceleration is 1,5 m/s^2 and the maximum deceleration is about 3,5 m/s^2. Now the acceleration takes about 5 seconds. The acceleration graph is relatively wide in all the runs compared to the overall length of the run. This means that the cable drone keeps accelerating for approximately half of the run until it needs to change its direction. The reached top speed is about 5 m/s. The satellite signal strength is a little bit over 80 dBHz so it is in the same level as it was in the previous rounds. Faster acceleration of the motor would most likely lead into more wheel spinning. A smoother acceleration could help with the wheel spinning problem and thus lead to faster acceleration. This would naturally widen the part where the cable drone moves at constant velocity. The direction of the cable drone seems to have an effect on the maximum velocity. This can be caused by wind and the form of the cable. These kinds of factors can be corrected with the Closed Loop Speed -mode, where the power is not constant but varies based on how much power is needed.

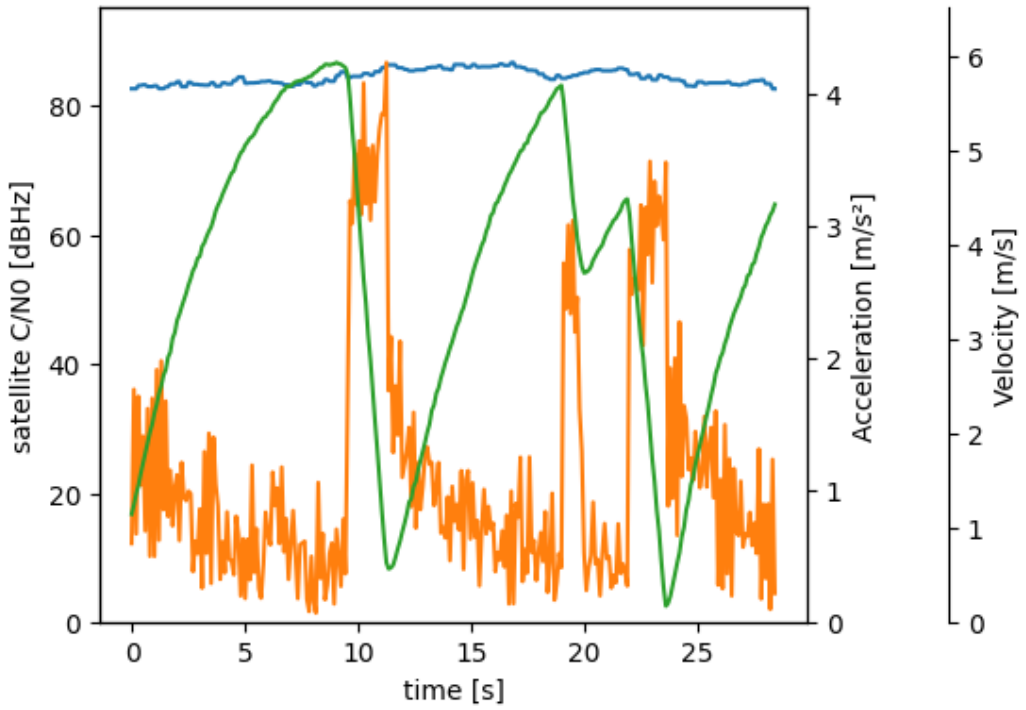

Figure 42. Acceleration (orange), velocity (green), satellite C/N_0 (blue) data when driving at 50% of maximum power.

The number of repetitions is small in this last test round, but some considerations can be made. During the last test runs the acceleration problem was already visible. The cable drone was not able to reach constant speed at all, as it can be seen in Figure 42. The acceleration peaks in the graph are wide, acceleration takes nearly 10 seconds. Acceleration should be increased. The maximum acceleration is again approximately 1,5 m/s^2 and the deceleration is around 3,5 m/s^2. Even though the constant velocity was not achieved at the time, the cable drone did keep its location within permissible limits. In the second run, when about 18 seconds have passed, there is a visible braking due to release of the dead man's switch. The O-ring was clearly worn out and it was decided to end testing there. Dead man's switch works well. The acceleration and the velocity graphs peak at that time because the cable drone brakes suddenly. The satellite C/N_0 is around 80 dBHz meaning that the measurements are quite accurate, but they are not as accurate as in the initial test runs.

6.4 Further analysis of the cable drone

The test results show that the cable drone is capable of carrying the required payload of multiple sensors although it is modified with all the equipment that make the automated

drive possible. The added weight reduces the speed achieved by the cable drone. Faster acceleration with larger payload can be achieved but it might require closed loop control. There are some challenges, but the system is worth developing.

The socket server between Jetson TX2 and another computer works well. More settings which must be easily changeable, for example the PID values for the motor controller, can be added later. The configuration of the PID values required the script to be changed considerably and therefore setting them up was left for later. Also, the Closed Loop Speed -mode was not fully working yet while tests were conducted. Reason for unexpected behaviour in the Closed Loop Speed -mode was that the encoder's Cycles per Revolution -value was set too low.

The test results of automated drive suggest that the acceleration profile needs to be reshaped. The form of the motion profile could be changed from a trapezoidal to an S-curve shaped profile, where the acceleration rate is limited. This prevents the wheel from slipping at the beginning of acceleration and at the stop. Changing the controlling mode from Open Loop Speed -mode to Closed Loop Speed -mode would increase the repeatability. Velocities are not constant due to Open Loop Speed -mode which controls the power.

The changes to the motion profile are needed in the future to spare the O-rings from wearing out too quickly due to excessive wheel spinning. The O-ring wear was detected in repeated tests. The cable drone was able to produce similar results in several tests despite this wear. After multiple runs with high accelerations the O-ring must be replaced with a new one. Another benefit of manipulating the motion profile is that the constant velocity could be reached more quickly, and the maximum velocity could be increased.

Noise-like, high frequency variation in acceleration graphs is similar both in manual runs in chapter 6.1 and in automated test runs in chapter 6.3. This variation is probably caused by vibrations and shaking of the cable drone while it is moving. Even if this would not cause problems for the cable drone, it would be wise to dampen the vibration from the portable sensor system so it would not interfere with measurements in the future. Logitech's BRIO 4K pro webcams have produced some challenges occasionally. Sometimes they do not stay on or capture images when other devices are also connected. It turns out they're not fully compatible with Linux. This is a somewhat

larger problem; thus, the cameras will be replaced with other cameras so that they do not become a problem in the future.

The cable drone performed well in a windy environment when the system was briefly tested at the OuluZone. The tests at the OuluZone are still in progress and the portable sensor system has not been used there yet so no actual data is yet gathered. At the time the cable drone was equipped with two large plastic balls which are used as configuration points for drones, shown in Figure 43. The purpose of this test was to try out the cables at a longer span. The distance between the truss towers was 150 meters.

Figure 43. The cable drone at the OuluZone.

The test at the OuluZone was successful, and the cables were raised with the truss towers and tightened securely. The elongation of the cables was not closely studied. However, the cables showed no visible changes like stretching or damage during the tests. Then the cable drone was tried out briefly with manual drive and the wind did not seem to affect it significantly. There was a little bit of ice or frost on the surface of the cables, but it did not cause problems. Moisture reduces friction between wheel and cable, so it can influence acceleration and increase braking distance.

The location of the cable drone is known within the limits of GNSS/INS location information. The MTI-G-710 promises a horizontal accuracy of 1,0 meters, which can

be considered currently sufficient accuracy. Improving accuracy would require for example an RTK GPS but using it on the cable drone or the portable sensor system was excluded from this work.

6.5 Further studies

Applying the RTK GPS method with the u-blox C94-M8P or another similar device should be more thoroughly tested to get centimeter-level accuracy of the cable drone's location. More time for the setup is required to get this method to work. This method needs to be tested in a wider space, somewhere without buildings or other structures which interfere with the signal and thus cause problems to the location estimation. Attaching the rover to the portable sensor system or the cable drone's body will not cause any significant problems and the stationary base can be placed on the truss tower.

To be able to leave the cable drone on the cables for a longer period of time, a docking station with a wireless charging must be designed. The docking station should offer protection from weather. Automated drive will have to be expanded with a scheduled driving sequence which includes a safe method for docking to the station. The docking station can include other devices also, for example a wireless router for Wi-Fi signal strength data logging.

The tests mentioned in chapter 5.1 (Use of the cable drone) can begin. The tests have already offered data from the LiDAR which have been reconstructed to the point cloud shown in Figure 44. The data is from the Botanical Garden. In addition to the aforementioned tests, to improve the current version of the cable drone, wearing and abrasion of different O-rings should be studied. This provides information on how they affect the wheelspin.

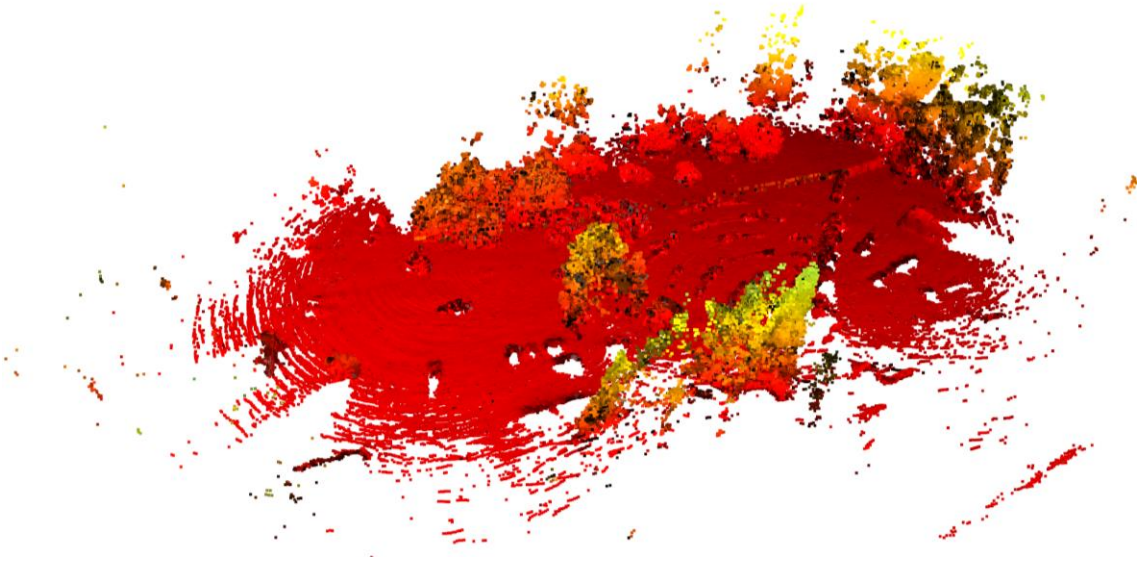

Figure 44. Point cloud map of the Botanical Garden from the LiDAR data.

A VR Simulation of the collected data has already been started. In the simulation the cable drone's track is shown with blocks that change color depending on the acceleration of the cable drone, red depicts high acceleration, and yellow for constant speed. The simulation was first done from saved data, but it has already been implemented to offer the same information almost in real-time.

A new version of the cable drone could also be built to better meet the requirements, now as the truss towers are tested and they are proven to work properly. The new cable drone should have more grip on the cable. The basic operating principle could stay the same, but also some larger changes could be made to the new model. In the current model, there is only one drive wheel. If it was replaced with multiple drive wheels and the cable drone's frame would be altered so that the wheels can be supported on both sides, a higher pressure can be applied to the wheels. Better traction is required if the new cable drone will be used automatedly without constant surveillance. Both the current and the upcoming model could be used in Closed Loop Speed -mode, thus that must be more thoroughly tested.

7 CONCLUSIONS

This master's thesis has an overview of phenomena and known errors which occur when a picture is taken in motion. The importance of testing sensors was highlighted later, and some validation criteria were listed. In testing of such subjects, the cable drone could be utilized to generate a controlled motion. A sensor testing system, which uses an automated cable drone as a method of movement, was tested and evaluated in this project.

The cable drone proved to be a system worth developing. Automated drive was achieved, and data could now be gathered in various weather conditions and different locations. The cable drone was modified to fit the requirements and new ideas for a new model of the cable drone came up while the tests went on. Modifications like for example a new case with two larger batteries, made the cable drone heavier but it is still capable of carrying the required payload of multiple sensors. These modifications were required to make the automated drive possible.

Automated driving sequence of the cable drone was tested in Open Loop Speed -mode. In order to achieve a steady velocity, many contributing factors must be considered. The Closed Loop Speed -mode would work better in this application. The test results of automated drive suggest also that the acceleration profile needs to be reshaped. The form of the motion profile could be changed from a trapezoidal to an S-curve shaped profile, where the acceleration rate is limited. Automated driving was achieved but reaching the goal set for steady velocity requires still some work.

The portable sensor system works well. With multiple possible attachment points for the sensors and various ways for quick modification of the frame, the aluminium profile is a very good choice for this application. The same portable sensor system can be used in many different applications besides the cable drone. It can be equipped with the kind of sensors which is needed at that time. The goal to make a portable, easily attachable, and customizable sensor system frame is achieved. The position of the cable drone is known in the level of accuracy which the Xsens MTi-G-710 can provide. The position estimate's accuracy can be improved considerably with an RTK GPS.

A hinged truss tower structure that holds the cables in place while the tower is lifted was developed for this project. The truss tower is secured in its place with three guy-wires and a ground anchor. The cables can be left in place while they are not used. The cables could then be lowered with ratchet cable pullers or a pulling hoist when the cable drone is to be set on the cables. One goal was to find a way to lift the cables in the air securely without the need for humans to climb on ladders and place them afterwards. This goal is reached. The idea of such an anchoring method came after the master's thesis plans were made, but it was decided to be included it in this project

When an additional goal for the development of the cables' lifting system was set, ideas had to be assessed. The use of towers in the fastening and lifting of cables seemed like a straightforward task at first, but it eventually took quite a lot of time to plan and put into practice. This meant that the focus of the thesis would be changed to the construction of a new testing environment that had to meet the requirements set by the original tests. The experimental testing of sensors was omitted from the master's thesis, so the theoretical part was also changed to focus on the forces the cables exert and on the cables' behaviour in addition to general sensor testing and sensors' performance. The knowledge and equations of the forces were later used in structural analysis of the truss tower.

A completely new version of the cable drone could also be built in the future. By replacing one drive wheel with multiple drive wheels and altering the cable drone's frame so that the wheels can be supported on both sides, a higher pressure can be applied to the wheels. Better traction is required if the new cable drone model will be used automatedly. This would make the cable drone meet the requirements better. Both the current and the upcoming model could benefit from Closed Loop Speed -mode and therefore it is important to make it work.

8 REFERENCES

Air Drone Craze, 2021. The Future of Drone Technology. [online document]. Available: https://airdronecraze.com/drone-tech/ [Accessed 29 March 2021]

Anaheim Automation, 2021a. ENC-A5S Series Assembly Instructions Guide. [online document]. Available: https://www.anaheimautomation.com/manuals/encoder/L010745%20-%20ENC-A5S%20Series%20Assembly%20Instructions.pdf [Accessed 10 March 2021]

Anaheim Automation, 2021b. ENC-A5SN Single-Ended Encoder without Index Channel. [online document]. Available: https://www.anaheimautomation.com/manuals/encoder/L010732%20-%20ENC-A5SN%20Single-Ended%20Encoder%20without%20Index.pdf [Accessed 10 March 2021]

Aqel, M. O. A., Ismail N. B., Marhaban, M. H., Saripan, M. I. 2016. Review of visual odometry: types, approaches, challenges, and applications. [online document]. Berlin: SpringerPlus, 5. Available: https://springerplus.springeropen.com/articles/10.1186/s40064-016-3573-7#article-info [Accessed 23 July 2021].

Artlist, 2020. Everything you need to know about the gimbal. Available: https://artlist.io/blog/everything-you-need-to-know-about-the-gimbal/ [Accessed 8 March 2020]

Basri R., Singer A., Voroninski, V. and Özyeşil, O., 2017. A survey of structure from motion. Acta Numerica, 26, pp. 305–364. doi:10.1017/s096249291700006x

Ben-Ezra M. and Nayar S. K., 2004. Motion-based motion deblurring. In: Chellappa, R. and Kriegman D. J. et al. (eds) IEEE Transactions on pattern Analysis and Machine Intelligence. 26 (6). New York: IEEE Computer Society pp. 689-698

Bovik, A. C., 2005. Handbook of Image and Video Processing. Vol 2nd ed. Amsterdam: Elsevier Inc., p. 1372. ISBN 978-012119792-6.

Brook S., Fulkerson B., Gunnert-Jepsen A., Harville M., Piro D., and Radford J., 2020. Introduction to Intel® RealSense™ Visual SLAM and the T265 Tracking Camera. [online document]. Available: https://dev.intelrealsense.com/docs/intel-realsensetm-visual-slam-and-the-t265-tracking-camera?_ga=2.157333564.783877164.1626433620-353838607.1625655728. [Accessed 16 July 2021]

Burgess A., Holland R., and Molloy J., 2020a Performance Testing for Sensors in Connected and Autonomous Vehicles: Feasibility Study. United Kingdom: Catapult Network.

Burgess A., Holland R., and Molloy J., 2020b Performance Testing for Sensors in Connected and Autonomous Vehicles: Feasibility Study. Appendices. United Kingdom: Catapult Network.

Cadena C, Carlone, L, Carrillo H, Latif Y, Leonard J. J., Neira J, Reid I. and Scaramuzza D., 2016. Past, Present, and Future of Simultaneous Localization and Mapping: Toward the Robust-Perception Age. IEE TRANSACTIONS ON ROBOTICS, 32 (6), pp. 1309-1332

Chellappa R. and Rajagopalan A. N., 2014. Motion Deblurring: Algorithms and Systems. Cambridge: Cambridge University Press. p. 294. ISBN 978-1-107-04436-4.

Cook G., 2011 Mobile robots: navigation, control and remote sensing. New York: Wiley. p. 324. ISBN: 978-0-470-63021-1

Cultofdrone, 2021. Drone IMU Calibration. Available: https://cultofdrone.com/drone-imu-calibration/ [Accessed 18 October 2021]

DJI, 2021. DJI – Official Website. Available: https://www.dji.com/ [Accessed 10 March 2021]

Droneinfo, 2021. EU drone regulation. Available: https://droneinfo.fi/en/eu-drone-regulation [Accessed 11 February 2021]

Freefly Systems, 2021. Camera Movement Systems for Filmmakers. Available: https://freeflysystems.com/ [Accessed 10 March 2021]

Gaudiot J-L, Liu S., Li L., Tang J., and Wu S., 2020. Creating Autonomous Vehicle Systems. 2nd edition. California: Morgan & Claypool Publishers. p.216.

Geman D. & Geman S., 1984. Stochastic Relaxation, Gibbs Distributions, and the Bayesian Restoration of Images. IEEE Transactions on Pattern Analysis and Machine Intelligence. 6(6) pp.721-741.

Georgiev, M., Bregovic, R., & Gotchev, A., 2015. Fixed-Pattern Noise Modeling and Removal in Time-of-Flight Sensing. IEEE Transactions on Instrumentation and Measurement, 65(4), pp. 808-820.

Georgy J., Karmat T. and Noureldin A., 2013 Fundamentals of inertial navigation, satellite-based positioning and their integration. Berlin: Springer. p. 332. ISBN 978-3-642-30466-8

Gröll L and Kapp A., 2007. Effect of Fast Motion on Range Images Acquired by Lidar Scanners for Automotive Applications. IEEE TRANSACTIONS ON SIGNAL PROCESSING, 55. pp. 2945–2953.

Haataja K., Imani V., Toivanen P., 2018. Three main paradigms of simultaneous localization and mapping (SLAM) problem. Proc. SPIE 10696, Tenth International Conference on Machine Vision (ICMV 2017), Vienna, Austria.

Ibanez-Guzman J, and Li Y, 2020. Lidar for Autonomous Driving: The Principles, Challenges, and Trends for Automotive Lidar and Perception Systems. IEEE Signal Processing Magazine, 37 (4) 50-61

Intel, 2019. Intel RealSense Tracking camera – Datasheet. Available: https://www.intel.com/content/dam/support/us/en/documents/emerging-technologies/intel-realsense-technology/IntelRealSenseTrackingT265Datasheet.pdf [Accessed 21 July 2021]

Kiang Y-W and Li H-J, 2004. Radar and Inverse Scattering. In: Chen W.-K. (ed.) The Electrical Engineering Handbook. Boston: Elsevier Academic Press, pp. 671-691. ISBN 0-12-170960-4

Lagendijk R. L., and Biemond J., 2009. Basic Methods for Image Restoration and Identification In: Bovik, A. C. The Essential Guide to Image Processing. Amsterdam: Elsevier Inc., pp. 349-383. ISBN 978-0-12-374457-9.

Logitech, 2017. Logitech BRIO – Datasheet. available: https://www.logitech.com/content/dam/logitech/fi_fi/video-collaboration/pdf/brio-datasheet.pdf [Accessed 23 July 2021]

Mansurov N., 2020. Photography Life, Dead vs Stuck vs Hot Pixels. Available: https://photographylife.com/dead-vs-stuck-vs-hot-pixels#dead-pixels [Accessed 15 March 2021]

Mardirosian R., 2020. Lidar vs. camera: driving in the rain. Available: https://ouster.com/blog/lidar-vs-camera-comparison-in-the-rain/ [Accessed 9 September 2021]

McHugh S.T., 2019. Understanding Photography: Master Your Digital Camera and Capture That Perfect Photo. San Francisco: No Starch Press, Inc. p. 240. ISBN-13: 978-1-59327-894-6.

Morales Y, Tsubouchi T, 2007. DGPS, RTK-GPS and StarFire DGPS performance under tree shading environments. 2007 IEEE International Conference on Integration Technology, pp. 519-524.

Motion Compound Engineering, 2018. MCE Cable Camera Manual. 28 p.

Motion Compound Engineering, 2021a. Available: https://motioncompound-cablecam.de/mce-cable-cam-kit/ [Accessed 24 February 2021]

Motion Compound Engineering, 2021b. Socialmedia. Available: https://motioncompound-cablecam.de/socialmedia/ [Accessed 10 February 2021]

Newton Nordic, 2021. References. Available: https://newtonnordic.com/stories-about-newton-stabilized-remote-camera-system/ [Accessed 10 February 2021]

NovAtel, 2015. An Introduction to GNSS, 2nd edition. [online document]. Canada: NovAtel Inc. Available: https://novatel.com/an-introduction-to-gnss [Accessed 13 July 2021]. 91 p.

NVIDIA, 2021. JETSON XAVIER NX. [online document]. Available: https://www.nvidia.com/en-us/autonomous-machines/embedded-systems/jetson-xavier-nx/ [Accessed 26 July 2021]

Ouster, 2021. OS0 – Datasheet. Available: https://data.ouster.io/downloads/datasheets/datasheet-revd-v2p1-os0.pdf [Accessed 23 July 2021]. 5 p.

Rastogi P., 2015. Digital Optical Measurement Techniques and Applications. Norwood, MA: Artech House. 488 p. ISBN-13:978-1-60807-806-6.

Reinelt T., 2015. Seilkräfte fahrbare Kamera, Statische Berechnung, Motion Compound GbR. 5 p.

RoboteQ, 2018. Version 1.4, MDC1230/MDC1460 Motor Controller Datasheet. Available: https://www.roboteq.com/docman-list/motor-controllers-documents-and-files/documentation/datasheets/213-mdc14xx-datasheet/file [Accessed 10 March 2021]. 11 p.

SFS-EN 1991-1-4, 2010. Eurocode 1: Actions on structures. Part 1-4: General actions. Wind actions. 2nd edition. Finnish Standards Association SFS: 157+97 p.

SFS-EN 13814-1:2019, 2019. Safety of amusement rides and amusement devices. Part 1: Design and manufacture. Finnish Standards Association SFS: 163+13 p.

SkyCam, 2021. Official site of SkyCam. Available: www.skycam.tv [Accessed 25 October 2021]

The Tiffen Company, 2020. Steadicam. https://tiffen.com/pages/steadicam [Accessed 10 March 2021].

Unmanned Systems Technology, 2021. What is a Gimbal? Available: https://www.unmannedsystemstechnology.com/category/supplier-directory/cameras-imaging-systems/gimballed-sensors/ [Accessed 8 March 2021].

Vectornav, 2021a. Inertial sensors. Available: https://www.vectornav.com/resources/inertial-navigation-primer/theory-of-operation/theory-inertial [Accessed 20 July 2021].

Vectornav 2021b. What is an inertial measurement unit? Available: https://www.vectornav.com/resources/inertial-navigation-articles/what-is-an-inertial-measurement-unit-imu [Accessed 20 July 2021].

Xsens, 2020. MTi User Manual. Available: https://www.xsens.com/hubfs/Downloads/usermanual/MTi_usermanual.pdf [Accessed 23 July 2021]. 61 p.

Xsens, 2021a. From IMU to GNSS/INS. Available: https://mtidocs.xsens.com/from-imu-to-gnss/ins [Accessed 20 July 2021]

Xsens, 2021b. Global Navigation Satellite/Inertial Navigation Systems. Available: https://www.xsens.com/gnss-ins [Accessed 22 July 2021].

Xsens, 2021c. Gyroscopes - Overview. Available: https://www.xsens.com/gyroscopes [Accessed 20 July 2021].

ZHIYUN-TECH, 2021. ZHIYUN-TECH official website. Available: https://www.zhiyun-tech.com/en [Accessed 10 March 2021].